Astronomy Reports, Vol. 44, No. 6, 2000, pp. 349–352. Translated from Astronomicheskiĭ Zhurnal, Vol. 77, No. 6, 2000, pp. 403–406.
Original Russian Text Copyright © 2000 by Artyukh.

A Search for Large-Scale Inhomogeneities in the Distribution of Compact Radio Sources

V. S. Artyukh

Pushchino Radio Astronomy Observatory, Pushchino, Serpukhovskiĭ region, Moscow oblast, 142292 Russia

Received December 29, 1998

Abstract—A correlation analysis for a survey of compact radio sources (~0.1″) is presented. The survey is based on interplanetary-scintillation observations carried out at 102 MHz on the Large Phased Array of the Lebedev Physical Institute. The survey area covers 0.1 ster centered on the direction $\alpha = 10^h28^m$ and $\delta = 41°$. The distribution of scintillating sources is uniform on scales $1° < \theta < 6.5°$. © *2000 MAIK "Nauka/Interperiodica".*

1. INTRODUCTION

Information about the large-scale structure of the Universe and, in particular, about large-scale clustering of matter is very important for modern cosmology. Theoretical studies usually consider uniform models, which assume that the Universe is statistically uniform beginning on some scale (see the review [1]). However, on small scales, matter is distributed substantially inhomogeneously. Stars are concentrated in galaxies, which, in turn, form groups, clusters, and superclusters. In addition, giant voids on scales to 100 Mpc are observed in the distribution of galaxies [2, 3]. There is currently no evidence that this represents a limiting scale for inhomogeneity in the distribution of matter in the Universe. The question naturally arises of to which scales the Universe remains inhomogenous, such that, after averaging over these scales, the distribution of matter can be considered uniform and isotropic.

The solution of this problem encounters considerable difficulties; in particular, it is difficult to find appropriate "test particles"—beacons that can be used to trace the large-scale distribution of matter in the Universe. Optical galaxies are ill-suited for this purpose, due to the presence of dust that absorbs the optical radiation. It is difficult to distinguish inhomogeneities in the dust distribution from inhomogeneities in the galaxy distribution. Statistically uniform samples can be constructed on the basis of radio surveys. Radio radiation is not absorbed by dust, making radio samples preferable to optical samples. Unfortunately, here, there are also difficulties. Observations have demonstrated that the weakest radio sources are not necessarily the most distant ones. At flux densities of $S > 1$ mJy, the main contribution to the radio-source population is made by active galactic nuclei, which are at cosmological distances and have substantial redshifts; at flux densities of $S < 1$ mJy, the main contribution to source counts is made by blue galaxies whose activity is associated with star formation, which are comparatively nearby objects (mean redshift $z \sim 0.7$ [4]).

The situation changes if we consider only compact (~0.1″) radio sources at meter wavelengths. As shown in [5], the vast majority of low-frequency compact radio sources are associated with active galactic nuclei. Even high-luminosity infrared galaxies with outbursts of star formation do not have appreciable compact radio structure at meter wavelengths [6].

A survey of compact (~0.1″) radio sources based on 102-MHz scintillation observations on the largest meter-wavelength radio telescope—the Large Phased Array (LPA) of the Lebedev Physical Institute in Pushchino—enabled the detection of compact (scintillating) sources that were an order of magnitude fainter than previously known sources [7, 8]. In two areas of the 7C survey with total area 0.144 ster, 395 scintillating sources were detected, of which 380 had not been detected previously. The detected sources are characterized by a high degree of compactness and the presence of steep radio spectra for both compact and extended components. Analyses of observations of various classes of active galaxies (quasars, BL Lac objects, radio galaxies, Seyfert galaxies, LINERs) and normal galaxies carried out on this same instrument indicate that the scintillating sources are primarily quasars [9].

Scintillating-source counts from our survey [7, 8] have shown a sharp fall-off in the counts at weak flux densities ($S < 0.6$ Jy), which could be due to the birth of radio sources in the nuclei of galaxies during the course of cosmological evolution [10]. If the appearance of compact radio sources in galactic nuclei occurs at an early stage in the evolution of a galaxy, we expect that most weak scintillating sources have large redshifts, making them suitable objects for studies of the large-scale structure of the Universe.

1063-7729/00/4406-0349$20.00 © 2000 MAIK "Nauka/Interperiodica"

2. CORRELATION ANALYSIS FOR THE SCINTILLATING-SOURCE SAMPLE

To search for clustering of the compact radio sources, we conducted a correlation analysis of the distribution of scintillating sources from the second 7C-survey area [11]. In this area, which covers 0.1 ster (~327 square degrees) centered on the direction ($\alpha = 10^h28^m$, $\delta = 41°$), 289 scintillating sources with 102-MHz flux densities $S > 0.1$ Jy were detected. We used these data to estimate the two-point correlation function for the distribution of scintillating sources over the celestial sphere using the method presented in [12].

We will present the main assumptions of this method. The probability that a source is located in an arbitrary area of the celestial sphere $\delta\Omega$ is equal to

$$P = n\delta\Omega, \quad (1)$$

where n is the mean surface density of sources. The probability of finding one source in an area $\delta\Omega_1$ and a second source in an area $\delta\Omega_2$ separated from the first by a distance θ is

$$P = n^2[1 + w(\theta)]\delta\Omega_1\delta\Omega_2, \quad (2)$$

where $w(\theta)$ is the two-point correlation function for the distribution of sources. If the source distribution is described by a continuous function $n(\omega)$, then $n = \langle n(\omega)\rangle$, and

$$w(\theta) = \langle [n(\omega + \theta) - n][n(\omega) - n]\rangle / n^2. \quad (3)$$

It follows from (2) that the expected number of pairs of sources separated by distances from θ to $\theta + \delta\theta$ within an area Ω is equal to

$$N_p(\theta) = 0.5n^2[1 + w(\theta)]\Omega\langle\delta\Omega\rangle. \quad (4)$$

Here, $\langle\Omega\rangle$ is the mean value of the solid angle for the intersection of the survey region Ω and the ring $(\theta, \theta + \delta\theta)$. The coefficient 0.5 accounts for the fact that each pair gives rise to two terms. The solid angle for the survey is

$$\Omega_0 = (\alpha_B - \alpha_E)(\sin\delta_B - \sin\delta_E), \quad (5)$$

where α_B and α_E are the right ascension of the beginning and end of the survey and, similarly, δ_B and δ_E are the maximum and minimum declinations for the survey. We obtain an estimate of N_p via a direct count of the number of neighbors for all the scintillating sources in our catalog, based on the fact that the distance between two sources with coordinates (α_1, δ_1) and (α_2, δ_2) is given by the expression

$$\cos\theta = \sin\delta_1\sin\delta_2 + \cos\delta_1\cos\delta_2\cos(\alpha_2 - \alpha_1). \quad (6)$$

We adopted $n = N/\Omega$ as an estimate of n, where N is the total number of sources in the catalog. The quantity $\langle\delta\Omega\rangle$ depends on the thickness of the ring $\delta\theta$, which we can chose somewhat arbitrarily; we adopted $\delta\theta = 0.2\theta$. However, this arbitrariness can be completely excluded by the method proposed in [1], based on model computations. Generating random coordinates for N sources by computer, we use them to fill an area Ω of the same shape as the observed area. We then conduct a count of pairs of the "artificial" sources using the same program as in the analysis of the real observations, with the same $\delta\theta$. Since the distribution of sources in the model computations is completely random (Poisson), by definition, $w(\theta) = 0$. In addition, it follows from (4) that the ratio of the number of pairs in the real catalog N_p to the number of pairs in the model computations N_m is equal to

$$N_p/N_m = 1 + w(\theta). \quad (7)$$

We can estimate $w(\theta)$ from this expression. In order to avoid taking into account edge effects in a complicated way, when counting pairs, we chose only sources at least θ from the survey boundary. In this case, neighbors that are separated from the boundary by less than θ appear in the counts one time, while neighbors separated from the boundary by more than θ are counted twice. The ratio of counts of pairs for the real and model surveys allows us to exclude this effect.

With what step in θ should we estimate $w(\theta)$? It was shown in [13] that the output signal of a radio telescope is correlated and that the correlation function is equal to

$$\gamma(\theta) = a\int K(r)K(r + \theta)dr. \quad (8)$$

Here, a is a normalized coefficient and $K(\theta)$ is the antenna beam pattern. Relation (8) is valid when the angular size of the radio source is substantially smaller than the antenna-beam size. Since, in our observations, the sizes of the scintillating sources are ~0.1″ and the size of the LPA antenna beam is $\sim 1° \times 0.5°$, this condition is satisfied. It follows from (8) that the characteristic scale for correlation of the output signal of a radio telescope is determined by the size of the antenna beam. In fact, if the functions in (8) have second moments, it follows from the properties of the convolution that $\sigma_\gamma = \sqrt{2}\,\sigma_E$ [14], where

$$\sigma_E^2 = \int\theta^2 K(\theta)d\theta / \int K(\theta)d\theta \quad (9)$$

σ_γ is determined in an analogous fashion. An estimate of any correlation function is itself correlated, and the covariance of these estimates is [15]

$$\mathrm{cov}[w(\theta_1), w(\theta_2)] \cong (1/T)\int[\gamma(r)\gamma(r + \theta_2 - \theta_1) + \gamma(r + \theta_2)\gamma(r - \theta_1)]dr. \quad (10)$$

It follows from (10) that the characteristic correlation scale for estimates of $w(\theta)$ is determined by $\gamma(\theta)$, which, in turn, is determined by the antenna beam. Therefore, in our analysis of our catalog, the estimates of $w(\theta)$ will be independent if we choose them with a step that is no smaller than the maximum half-width of

the LPA antenna beam ($\Delta\theta \geq 1°$). The size of the survey area obviously determines an upper limit to θ.

The figure presents the resulting estimates $1 + w(\theta)$, together with their statistical errors. The dashed line corresponds to a Poisson distribution. The angle θ lies in the range from 1° to 6.5°. Note that observations for the analyzed survey of scintillating sources were carried out on a single radio telescope with equal sensitivities and that absorption by dust is negligible at radio wavelengths. Therefore, the systematic errors that dominate in estimates of $w(\theta)$ for optical surveys are virtually absent from our analysis. The main contribution to the errors is statistical. As shown in [1], if the survey objects are uncorrelated, the statistical error in the mean number of pairs N_p in the ring $\delta\Omega$ is $N_p^{-1/2}$. It is this error that is presented in the figure. Of course, the estimates of the number of pairs for the model computations N_m also have statistical errors. However, after averaging over 100 realizations of the computations, these errors are an order of magnitude smaller, so that they become negligible.

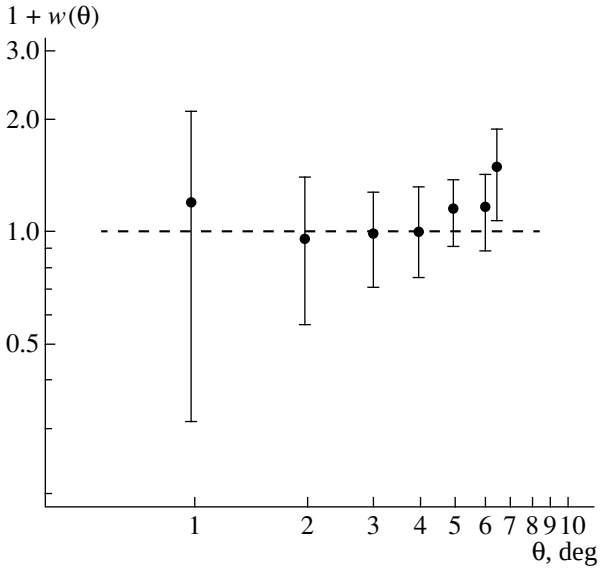

Two-point correlation function for the distribution of scintillating radio sources.

3. DISCUSSION

As we can see from the figure, the estimates of the two-point correlation function for the distribution of scintillating sources are consistent with zero to within the errors. Although the rise in the correlation function at $\theta = 6.5°$ suggests possible clustering on this scale, in our view, this result is preliminary and requires verification. Thus, we can take the scintillating sources to be distributed uniformly on scales from 1° to 7° in the given area.

In spite of the fact that the analyzed survey area is rather large (320 square degrees), it is clearly insufficient to extrapolate our results to the entire sky—our sample is not sufficiently representative for this, especially given that earlier observations on the LPA detected a clear deficit of scintillating sources (a radio void) in the direction of the radio galaxy DA 240 (in an area of 20 square degrees). The linear scale of this void is estimated to be 10^3 Mpc [16]. It is not yet clear whether this is a unique fluctuation or whether there exist other regions on the sky with clearly reduced or enhanced source densities. It is evident that new surveys of compact radio sources are needed, preferably of the entire sky.

The results of the present study indicate only that there are large areas of the sky in which the distribution of compact radio sources is uniform. Note that, if fluctuations in the density of sources are present only in a small area of the sky, and sources are uniformly distributed over the remaining surface of the celestial sphere, correlation analyses will not be sensitive to this sort of inhomogeneity, as pointed out in [1]. This may be why the correlation analysis of 4C radio sources carried out in [17] did not detect any deviations from a uniform distribution; other methods of cluster analysis are required to search for such nonuniformity.

ACKNOWLEDGMENTS

This work was supported by the Russian Foundation for Basic Research (project no. 96-02-17253).

REFERENCES

1. P. J. E. Peebles, *The Large-Scale Structure of the Universe* (Princeton University Press, Princeton, 1980; Mir, Moscow, 1983).
2. T. Kiang and W. C. Saslaw, Mon. Not. R. Astron. Soc. **143**, 129 (1969).
3. R. B. Tully, R. Scaramella, G. Vettolani, and G. Zamorani, Astrophys. J. **388**, 9 (1992).
4. P. A. Shaver, in *Seventeenth Texas Symposium on Relativistic Astrophysics and Cosmology*, Ed. by H. Bohringer, G. E. Morfill, and J. E. Trumper (New York Academy of Sciences, New York, 1995), p. 87.
5. V. S. Artyukh, Tr. Fiz. Inst. Akad. Nauk SSSR **189**, 223 (1988).
6. V. S. Artyukh, A. V. Zasov, and S. A. Tyul'bashev, Pis'ma Astron. Zh. **21**, 723 (1995) [Astron. Lett. **21**, 645 (1995)].
7. V. S. Artyukh and S. A. Tyul'bashev, Astron. Zh. **73**, 661 (1996) [Astron. Rep. **40**, 601 (1996)].
8. V. S. Artyukh, S. A. Tyul'bashev, and E. A. Isaev, Astron. Zh. **75**, 323 (1998) [Astron. Rep. **42**, 283 (1998)].

9. S. A. Tyul'bashev, Astron. Zh. **74**, 812 (1997) [Astron. Rep. **41**, 723 (1997)].

10. V. S. Artyukh and S. A. Tyul'bashev, Astron. Zh. **75**, 613 (1998) [Astron. Rep. **42**, 576 (1998)].

11. M. M. McGilchrist, J. E. Baldwin, J. M. Riley, *et al.*, Mon. Not. R. Astron. Soc. **246**, 110 (1990).

12. P. J. E. Peebles and M. G. Hauser, Astrophys. J., Suppl. Ser. **28**, 19 (1974).

13. V. S. Artyukh, V. V. Vitkevich, and I. M. Dagkesamanskaya, Astron. Zh. **50**, 924 (1973) [Sov. Astron. **17**, 588 (1973)].

14. L. Schwartz, *Mathematics for the Physical Sciences*. Transl. from the French (Addison-Wesley, Reading, 1966; Mir, Moscow, 1965).

15. G. M. Jenkins and D. G. Watts, in *Spectral Analysis and Its Applications* (Holden-Day, San Francisco, 1968; Mir, Moscow, 1971), Vol. 1, p. 218.

16. V. S. Artyukh and M. A. Ogannisyan, Pis'ma Astron. Zh. **14**, 888 (1988) [Sov. Astron. **14**, 377 (1988)].

17. M. Seldner and P. J. E. Peebles, Astrophys. J. **225**, 7 (1978).

Translated by D. Gabuzda

Astronomy Reports, Vol. 44, No. 6, 2000, pp. 353–364. Translated from Astronomicheskiĭ Zhurnal, Vol. 77, No. 6, 2000, pp. 407–419.
Original Russian Text Copyright © 2000 by Gorshkov, Konnikova, Mingaliev.

Analysis of Instantaneous Spectra of a Complete Sample of Flat-Spectrum Radio Sources

A. G. Gorshkov[1], V. K. Konnikova[1], and M. G. Mingaliev[2]

[1]*Sternberg Astronomical Institute, Universitetskiĭ pr. 13, Moscow, 119899 Russia*

[2]*Special Astrophysical Observatory, Russian Academy of Sciences, Nizhniĭ Arkhyz, Karachaevo-Cherkesskaya Republic, 357147 Russia*

Received May 5, 1999

Abstract—The results of observations of a complete sample of radio sources with spectral indices $\alpha > -0.5$ ($S \propto \nu^{\alpha}$) are presented. The sample was selected from the Zelenchuk Survey at 3.9 GHz and contains all sources with declinations 4°–6°, Galactic latitudes $|b| > 10°$, and 3.9-GHz fluxes > 200 mJy. Spectra at 0.97–21.7 GHz were obtained for all 69 sample sources. The spectra were classified, and a correlation between variability amplitude and spectrum shape was found. The spectra were separated into extended and compact components. The distribution of spectral indices α for the extended components coincides with the distribution for sources with power-law spectra. The correlation between the luminosity and frequency of the peak flux density is confirmed. This correlation is due to the fact that the distribution of source linear dimensions does not depend on luminosity. *© 2000 MAIK "Nauka/Interperiodica".*

1. INTRODUCTION

Many radio sources with spectral indices $\alpha > -0.5$ ($S \propto \nu^{\alpha}$) have complex morphologies. We also classify objects whose spectra cannot be described by a power law over a wide frequency range and whose two-frequency spectral index at centimeter wavelengths is > –0.5 as flat-spectrum sources. In such sources, along with the emission of extended structures, an appreciable, and often dominant, fraction of the emission comes from very compact structures with angular sizes less than one arcsec. In some objects, these compact components are not resolved by VLBI on the largest baselines available on the Earth's surface. These compact structures are identified with active galactic nuclei (AGN) and the "central machines" that are ultimately responsible for the radio emission.

Nonstationary processes that take place in AGN result in variations of the flux densities of radio sources on various timescales, from days to decades. After the detection of variability in discrete sources in 1966 [1, 2], this phenomenon has been actively studied at many observatories. Long-term series of observations of large samples of radio sources at decimeter [3], centimeter [4, 5], and millimeter [6] wavelengths have been obtained. Detailed studies of the most remarkable representatives of this class of objects are also carried out (see, for example, [7]).

During the last 1.5 years, we have been studying the variability of sources with flat spectra over a wide frequency range. For this purpose, we observed sources in a complete sample selected from the 3.9-GHz Zelenchuk Survey [8]. The sample includes all sources with 3.9-GHz flux densities $S_{3.9} \geq 200$ mJy with declinations 4°–6° and Galactic latitudes $|b| > 10°$. The sample contains 161 sources, of which 69 objects (43%) have flat spectra ($\alpha_{(3.9\text{–}7.7\ \mathrm{GHz})} > -0.5$). We presented an analysis of the spectra of the sample sources with spectral indices $\alpha_{(3.9\text{–}7.7\ \mathrm{GHz})} \leq -0.5$ (steep spectra) in [9]. Based on RATAN-600 monitoring in 1985–1992 at 3.9 and 7.5 GHz, we found that only 14 of the 69 flat-spectrum sample sources did not display significant variability during the observation period [10].

The purpose of the present work is to study the spectral parameters of compact components and their possible connection with the character of the variability. The spectra of the variable sources change with time; therefore, studies of instantaneous spectra require measurements that are simultaneous or separated by intervals much shorter than the variability timescales, as well as measurements of the spectra over a wide frequency range. We consider the source spectra averaged over a time interval of 15 to 50 days and derive variability parameters from five observational sessions carried out over a year and a half.

2. OBSERVATIONS

The observations of the sample sources were carried out on the meridian on the RATAN-600 radio telescope simultaneously at six frequencies: 0.97, 2.3, 3.9, 7.7, 11.1, and 21.7 GHz. The parameters of the receivers used on the Northern sector of RATAN-600 are given in [11, 12]. The antenna beam parameters are presented in [9]. Nearly all the spectra were obtained in August and November 1997 and January–February 1998. The

1063-7729/00/4406-0353$20.00 © 2000 MAIK "Nauka/Interperiodica"

spectra of seven sources were measured in May 1997 and of two, in August 1996. In each series, the sources were observed daily for 15–30 days, except for the January–February 1998 series, when the sources were observed over 50 days.

In addition to the flat-spectrum sources, we observed sources with steep spectra and constant flux densities (no less than 40% of all the sources observed). We used these objects as reference sources in our variability study, to eliminate instrumental effects, and to calibrate the flux densities of the target sources. The flux densities of all sources were statistically calibrated against the flux densities for the constant sources listed in [9]. The flux density of a source was determined as the weighted-mean value obtained using all the data in each observational series. The error of the weighted-mean flux density is defined to be

$$\Delta S = [\Sigma(S_i - \langle S\rangle)^2/(N-1)]^{0.5},$$

where S_i is the flux density for a given day, $\langle S\rangle$ is the weighted-mean flux density, and N is the number of observations of the source in the series. This error includes all sources of error: noise, calibration errors, calibration-signal reference errors, antenna pointing errors, etc.

3. INVESTIGATION OF THE SPECTRA

Table 1 lists the measured flux densities of the flat-spectrum sources studied at declinations 4°–6°. Column 1 gives the source name; columns 2, 4, 6, 8, 10, and 12, the source flux densities at 0.97, 2.3, 3.9, 7.7, 11.1, and 21.7 GHz; columns 3, 5, 7, 9, 11, and 13, the errors in the flux densities at these frequencies; and column 14, the epoch of the observation.

Classification of the spectra. The spectra of all 69 sources were fit with a parabola on a logarithmic scale using a least-squares method. Examination of the spectra and their least-squares fits showed that the spectra at 3–23 GHz can be divided into five types, as shown in Fig. 1:

(1) Spectra with flux densities that grow with frequency (growing spectra; Fig. 1a).

(2) Spectra with a flux-density minimum (Fig. 1b).

(3) Spectra with flux densities that decrease with frequency (Fig. 1c).

(4) Spectra that cannot be satisfactorily fit with a parabola (complex spectra; Fig. 1d).

(5) Spectra with a flux-density maximum (Fig. 1e).

All these types of spectra except for type 4 are well approximated by a parabola; in the overwhelming majority of cases, the differences between the measured and approximated flux densities are within two sigma. Spectra of types 1 and 3 have a small positive or negative curvature. In three cases, the best fit is a straight line.

The complex and type-5 spectra have a flux-density maximum in the frequency range considered, but in complex spectra, this maximum is usually located at higher frequencies. In these spectra, a local minimum is often observed in addition to a maximum.

Table 2 lists the parameters of the sources belonging to different types. Column 1 gives the spectrum type; column 2, the number of sources of the given type and the fraction (in percent) they constitute of the entire sample; column 3, the number of sources in which variability was detected over 1.5 years and the mean variability index; and column 4, the mean redshifts of the sources.

Relation between type of spectrum and variability. All of the sample sources were observed at six frequencies over 1.5 years (in three to five sessions). Statistically significant flux density variations were detected in 26 of the 69 sources. For each of these sources, we calculated the variability index $\bar{V} = \Delta S/\langle S\rangle$, representing the mean relative amplitude of the variability for our observation period. The definition of $\bar{V}$ and the procedure for our calculations are given in [13].

It follows from the data of Table 2 that the number of variable sources and their mean relative variability amplitude depend on the spectrum type. All six sources with type 1 (growing) spectra showed significant variability during the 1.5-year observation period, with mean amplitude $\bar{V} = 0.32$. Among the type-2 sources (with a minimum in their spectra), 40% were variable, with mean variability amplitude $\bar{V} = 0.31$. Variability with mean amplitude $\bar{V} = 0.24$ was found in one-third of the sources with type-3 spectra. Variable sources with $\bar{V} = 0.26$ made up 40% of type-4 sources (with complex spectra). Only two of the 16 sources with type-5 spectra had flux densities that were variable over the 1.5-year observation period, with mean variability amplitude $\bar{V} = 0.12$.

We believe that sources with spectra of types 1 and 2 are at an early stage of development of an outburst; the flux-density maximum is at millimeter wavelengths in the source frame, and type-2 sources have a considerable extended component. Sources of types 3 and 4 are at a later stage of development of a flare. The difference between these types of spectra could be related to the different contributions of their extended components (greater in type 3) or to sources with type-3 spectra being at a later phase of their activity compared to sources of type 4. It is likely that a considerable fraction of sources with spectra of types 1–4 represent a single class of object that are at different stages of development of their activity.

Sources with spectra of type 5 differ from the remaining sources in the nearly complete absence of variable objects among them and the very narrow range of frequencies ν_{max} where the maximum flux density is attained (see below, Fig. 4, the shaded area of the histogram); the extended component in these sources is faint

Table 1. Flux densities of the radio sources, mJy

Name	Frequency, GHz												Epoch*
	0.97		2.3		3.9		7.7		11.1		21.7		
	S	σ	S	σ	S	σ	S	σ	S	σ	S	σ	
1	2	3	4	5	6	7	8	9	10	11	12	13	14
0002 + 051	123	10	164	9	237	6	203	7	180	7	130	12	4
0019 + 058	262	15	268	9	279	8	306	5	310	6	274	27	3
0026 + 048	501	12	429	6	417	5	370	5	341	8	262	11	4
0027 + 056	275	19	367	10	422	9	498	7	524	6	541	31	3
0119 + 041	941	16	1138	7	1368	10	1613	15	1696	17	1499	28	5
0146 + 056	592	22	1034	20	1256	11	1417	10	1360	14	986	35	3
0152 + 043	360	19	368	13	356	9	285	6	261	7	150	15	3
0231 + 045	302	12	327	9	304	5	252	6	215	5	133	15	2
0237 + 040	954	14	825	6	748	7	625	6	600	10	492	23	5
0258 + 058	348	30	355	8	342	7	309	6	266	6	186	13	3
0303 + 051			202	9	283	6	228	7	191	8	60	29	2
0320 + 045	245	21	149	5	132	3	105	4	97	5	107	10	5
0348 + 049	751	19	510	8	387	12	297	5	250	5	187	15	4
0351 + 045	430	14	331	6	344	5	278	4	252	7	146	17	5
0355 + 055	80	16	182	11	256	9	276	7	234	6	139	20	3
0357 + 057	306	24	360	11	387	9	470	18	497	13	417	32	2
0409 + 044	127	8	203	5	229	4	226	4	200	5	140	12	5
0423 + 051	337	20	589	7	561	6	472	6	420	8	346	18	5
0425 + 048	902	18	576	12	534	15	504	8	498	14	577	23	4
0430 + 052	4160	30	3950	25	3870	19	4455	37	4380	54	2990	143	3
0502 + 049	1015	13	971	8	845	7	780	6	724	11	599	25	5
0506 + 056	376	23	435	13	485	9	595	10	604	16	463	33	3
0718 + 042	243	11	219	4	310	5	434	5	532	9	610	31	5
0731 + 050	271	10	268	5	270	4	291	3	322	6	345	14	5
0801 + 044	330	12	264	11	269	11	188	7	185	8	87	26	3
0805 + 046	579	13	465	5	478	4	449	7	426	9	304	13	5
0806 + 059	612	17	341	10	275	5	209	7	194	9	177	26	2
0829 + 046	1018	15	966	11	980	8	1248	11	1462	16	1703	47	5
0830 + 040	352	22	246	18	269	9	340	7	392	8	370	22	3
0858 + 050	119	14	192	5	250	4	309	4	343	7	388	15	5
1013 + 054	373	11	215	4	163	3	147	4	170	6	238	19	5
1015 + 057	427	23	530	13	608	9	778	19	893	20	883	40	2
1036 + 054	413	12	470	5	554	7	693	7	743	12	713	32	5
1117 + 044	314	15	276	9	252	4	232	10	228	6	161	12	3
1142 + 052	805	14	496	6	421	6	350	5	361	8	367	19	5
1204 + 057	559	18	396	13	351	10	340	14	339	9	294	20	2
1219 + 054	379	22	235	10	190	12	178	6	184	9	102	18	3
1219 + 044	684	25	529	9	578	8	822	10	1073	10	1946	53	4
1228 + 045	285	18	313	9	302	6	295	6	287	8	316	20	4
1237 + 049	396	18	444	6	430	5	443	5	462	9	483	23	5
1358 + 046	351	16	233	13	202	7	168	5	153	6	105	27	3

Table 1. (Contd.)

1	2	3	4	5	6	7	8	9	10	11	12	13	14
1402 + 044	866	18	1064	7	1024	9	1058	9	1081	16	959	21	5
1421 + 048	209	22	197	9	176	5	172	6	181	8	190	14	4
1456 + 044	1226	16	842	7	837	8	924	8	1006	20	1378	44	5
1509 + 054	40	13	177	4	407	5	783	7	906	13	799	31	5
1541 + 050	296	39	269	9	274	6	278	6	278	10	234	19	3
1542 + 042	937	25	577	16	438	7	352	7	392	12	442	28	4
1548 + 056	2200	50	2463	23	3193	24	3980	28	3948	54	2898	92	3
1557 + 043	289	13	189	5	159	3	163	4	172	6	182	14	5
1614 + 051	266	22	615	7	851	7	866	8	734	12	476	24	5
1614 + 042	375	18	226	15	203	5	141	6	119	8	76	20	2
1642 + 054	750	22	439	7	295	6	235	5	214	7	175	15	5
1646 + 042	595	66	290	13	250	4	199	6	175	8	169	16	4
1656 + 053	1844	22	1378	12	1225	9	1245	9	1172	14	927	34	5
1725 + 044	598	20	620	8	778	9	1180	18	1303	36	1342	46	4
1758 + 046	88	26	244	17	255	9	229	9	201	7	193	26	1
1926 + 050	453	14	334	6	314	7	298	6	284	5	224	16	4
1936 + 046	586	26	453	6	412	4	427	5	406	12	418	21	5
2019 + 050	168	14	416	6	464	5	400	5	342	7	218	18	5
2114 + 048	316	24	263	6	259	4	335	5	381	9	441	20	4
2121 + 053	540	35	545	14	700	20	1178	24	1641	38	2219	113	3
2144 + 042	85	44	98	11	123	5	160	14	214	5	236	23	1
2149 + 056	484	17	868	20	902	9	792	8	700	7	465	28	2
2201 + 044	896	25	554	12	470	16	385	6	378	10	372	22	4
2243 + 047	633	16	388	5	405	8	399	8	399	8	387	15	4
2259 + 058	177	14	295	8	322	10	336	7	324	6	235	18	3
2318 + 049	659	13	695	7	846	7	956	8	1073	28	1308	47	4
2346 + 052	697	17	451	14	366	11	416	7	400	10	297	28	3
2355 + 042	254	24	207	5	188	3	190	4	210	7	236	18	5

* (1) August 1996, (2) May 1997, (3) August 1997, (4) November 1997, (5) January–February 1998.

(or absent). The mean peak frequency in the observer's frame is 6.87 GHz. Nine objects of this group are identified with quasars; their mean redshift, $\bar{z} = 2.03$, is nearly twice that of the sources of other spectral types. For the quasars, the mean peak frequency in the observer's frame virtually coincides with $\bar{\nu}_{max}$ for all of group 5. Therefore, we believe that most sources with type 5 spectra are distant, luminous quasars with a small range of redshifts. The variability timescale in the source frame is 3–4 years; for a mean redshift $\bar{z} \approx 2$, this is 9–12 years in the observer's frame, and changes in flux density will be insignificant over 1.5 years. Furthermore, it was shown in [10] that the variability amplitude decreases with increasing luminosity.

There are probably also distant quasars among the sources with complex spectra, however, with extended components. Note that variability is absent in sources with type-4 spectra in objects with $\nu_{max} < 7$ GHz.

To study the spectra of the compact components, we must isolate their spectra; i.e., remove the emission of the extended component.

Separation of the components. We assume that all the spectra consist of two components: a power-law component,

$$\log S = S_0 + \alpha \log \nu \quad (1)$$

and a compact component, which can be represented by a quadratic function

$$\log S = C + (\log \nu - B)^2/2A, \quad (2)$$

where C is the logarithm of the flux density at the maximum of the spectrum, B is the logarithm of the frequency of this maximum, and A is the logarithmic inter-

val from the peak frequency to the frequency where $d(\log S)/d(\log \nu) = 1$ (the spectral curvature). It was shown in [14] that the spectra of compact components are well represented by formula (2) over a wide range of frequencies. We separated the components as follows. We chose the best-fit solution

$$\Sigma[S_{\nu i} - (S^s_{\nu i} + S^c_{\nu i})]^2,$$

where $S_{\nu i}$ is the flux density measured at a given frequency, $S^s_{\nu i}$ is the flux density for the power-law component, and $S^c_{\nu i}$ is the flux density for the compact component. For sources with data at frequencies below 0.97 GHz, we also found fits using these data.

Figure 2 shows an example of the separation into components for the source 0805 + 046; the diamonds show the initial spectrum, the solid curve shows the compact component, and the dashed curve shows the extended component.

We managed to separate into components all 39 sources with spectra of types 4 and 5 and two of the nine sources with spectra of type 3; the flux densities of the compact components peak at frequencies not exceeding 23 GHz. We found no extended components in three sources. For the remaining 28 sources, we could not separate the components. There could be several reasons for this: First, more than one compact component could be present; second, the compact component could be very faint or absent; third, the frequency of the spectral maximum for the compact component could be much higher than the maximum frequency of our measurements.

Figure 3 shows the spectral-index distribution for the extended components we have distinguished. The mean spectral index $\bar{\alpha}$ is –0.87, and the distribution standard deviation $\sigma_{\bar{\alpha}}$ is 0.15. The mean index and character of the distribution are similar to parameters obtained for samples of constant sources with power-law spectra [9, 10]. This supports the correctness of our component separation.

At our lowest observation frequency, 0.97 GHz, the variable component of the flux density of the compact component strongly depends on the shape of the total spectrum: For type-5 spectra with maxima in the frequency range considered, this variable component constitutes from 35 to 100% of the total (i.e., absence of an extended component). For this type of spectra, the mean contribution of the compact component to the integrated flux density at 0.97 GHz is 75%.

For type-4 (complex) spectra, the fraction of the 0.97-GHz total flux density contributed by the compact component seldom exceeds 35% (the mean fraction is 25%). At 0.365 GHz, for most sources, the variable component contributes less than 10%.

Spectra of the compact components. Table 3 lists characteristics of 41 sources in which the spectra of the compact components peak at 3–23 GHz. We approximated the spectra using formula (2). Table 3 presents the source (1) name; (2), (3) right ascension and declination at epoch 1950.0; (4) identification; (5) redshift; (6) flux density (mJy) at the maximum of the spectrum; (7) frequency (GHz) for this maximum; and (8) spectral curvature (*A*). We derived these quantities using only our data at frequencies from 0.97 to 21.7 GHz.

Table 2. Source parameters as a function of spectrum type

Spectrum type	Number of sources of given type (percent of total)	Number of sources displaying variability in 1.5 years (mean variability amplitude $\bar{V}$)	Mean redshift of quasars *z* (number of objects)
1	2	3	4
1	6 (9%)	6 (0.32)	
2	15 (22%)	6 (0.31)	1.3 (7)
3	9 (13%)	3 (0.24)	
4	22 (31%)	9 (0.26)	1.2 (9)
5	17 (25%)	2 (0.12)	2.03 (9)

For sources with flux densities measured at lower frequencies (in the Texas Survey at 365 MHz, the Molonglo Survey at 408 MHz, or the Arecibo Survey at 611 MHz), we also approximated the spectra using these data. For most of the sources, the results of this approximation were close to those in Table 3. For example, the differences in the peak frequencies did not exceed 5%. This rather good agreement of the approximation coefficients also testifies to the correctness of our separation of the emission into components.

Figure 4 presents the distribution of the peak frequencies for the 41 sources listed in Table 3. The sources that had type-5 spectra prior to the component separation are shaded. The mean peak frequency for the distribution $\bar{\nu}_{max}$ is 9 GHz, with a standard deviation σ of 5 GHz.

Of the 41 sources, 18 objects are quasars with known redshifts, three are galaxies, and three are BL Lac objects. The mean peak frequency for the quasars $\bar{\nu}_{max}$ (QSO) is 8.65 GHz, with σ = 5.7 GHz. For sources identified with star-like objects and empty fields (i.e., objects with magnitudes fainter than 21), $\bar{\nu}_{max}$ is 8.8 GHz. The coincidence of the $\bar{\nu}_{max}$ values for the quasars and objects with unknown *z* suggests that the latter are primarily quasars with a mean redshift close to that of the known quasars in our sample. Therefore, we take the spectral characteristics of the known quasars to be typical of the sample of radio sources. For the sources identified with BL Lac objects and galaxies, $\bar{\nu}_{max}$ (L + G) is 10.8 GHz, with σ = 1.8 GHz; therefore, we infer that,

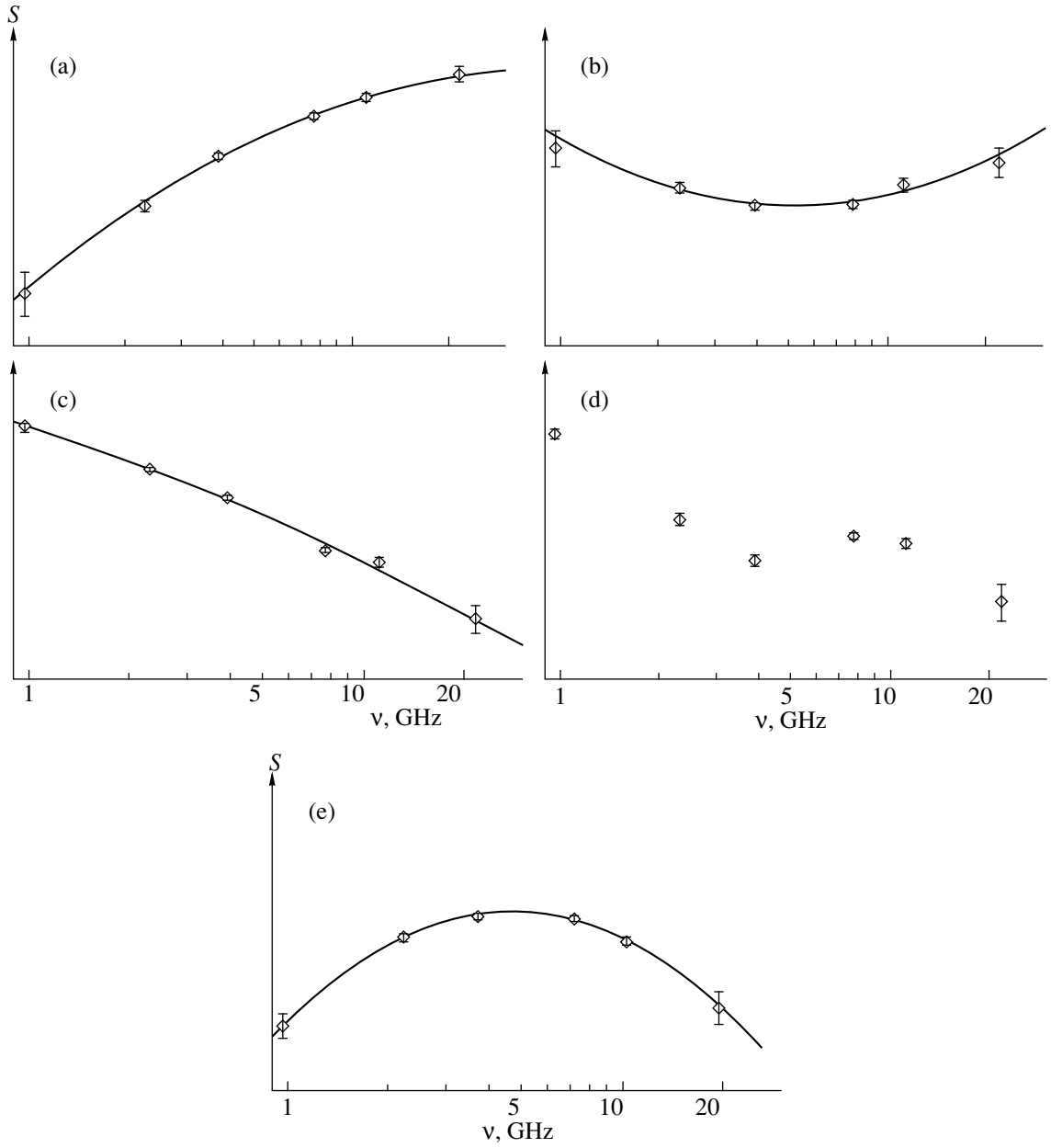

Fig. 1. Forms of spectra for the complete sample of radio sources with spectral indices $\alpha > -0.5$ (flat spectra). The vertical scale is in arbitrary units.

among the objects with unknown z, the (L + G) fraction is close to that among the identified sources.

Parameters of the spectra of compact components. Figure 5 shows the spectral characteristics of the compact components (diamonds: quasars, crosses: BL Lac objects and galaxies) as a function of redshift. For the BL Lac objects, we adopted $z = 0.5$. Figure 5a presents the absolute spectral radio luminosity at the peak frequency in a homogeneous, isotropic cosmological model with zero cosmological constant, deceleration parameter $q_0 = 0.5$, and $H = 50$ km s^{-1} Mpc^{-1}. The dashed line designates the minimum luminosity that can be detected for sources in our flux-density-limited sample; the straight-line segment shows the cutoff of the quasar luminosity function ($L_{\min} \sim 5 \times 10^{33}$ erg s^{-1} Hz^{-1}). We can see that, up to $z = \sim 1$, the quasars will be observable over the entire luminosity range.

Figure 5b shows the peak frequency in the source frame. The decrease of the variance of the peak-frequency distribution beginning at $z = \sim 1.4$ is readily visible. The mean peak frequency for quasars with $z < 1.4$, $\bar{\nu}_{\max}$ ($z < 1.4$), is 11.2 GHz, with $\sigma = 7.0$ GHz. For quasars with $z > 1.4$, we have $\bar{\nu}_{\max}$ ($z > 1.4$) = 6.1 GHz, with $\sigma = 2.0$ GHz; i.e., the standard deviation for this group

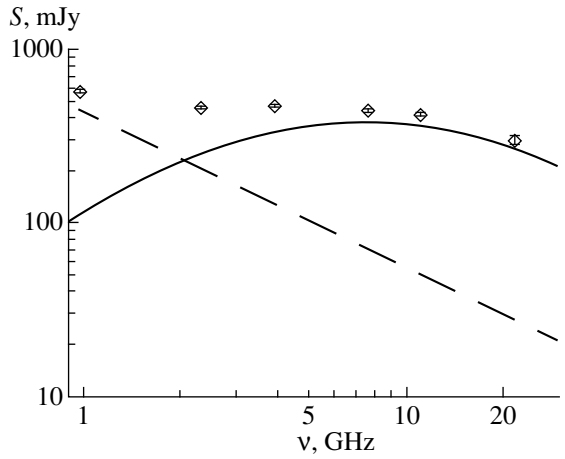

Fig. 2. Separation of the spectrum of 0805 + 046 into components. The diamonds show the initial spectrum, the dashed curve the spectrum of the extended component, and the solid curve the spectrum of the compact component.

of quasars is a factor of 3.5 smaller. The source-rest-frame peak frequencies for these groups of quasars nearly coincide: $\bar{\nu}_{max}$ ($z < 1.4$) = 21.0 GHz, σ = 14 GHz and ν_{max}($z > 1.4$) = 20.2 GHz, σ = 7.1 GHz. The rest-frame peak frequencies for the BL Lac objects are somewhat lower than for the quasars: $\bar{\nu}_{max}$ (L) = 17 GHz, σ = 1 GHz. All the data about the peak frequencies are listed in Table 4, which also gives the mean redshifts for each source group.

The variance decrease for distant quasars is due to the absence of sources with low peak frequencies. This could be due to the absence of low-luminosity quasars in this group. If low-luminosity quasars have, on average, lower peak frequencies, the peak frequencies will be bounded from below by a curve that is proportional to the spectral distance, i.e., by a dependence of the form $l_{bol}^2/(1 + z)$, which is shown by the dashed curve in Fig. 5b. This also supports the possible weak correlation between the peak frequency ν_{max} and redshift (the correlation coefficient is 0.356, with a significance level smaller than 10%). The peak frequency can depend on the luminosity if the distribution of linear dimensions of the compact components is independent of (or only weakly depends on) the luminosity.

Based on an analysis of the VLBI survey [16, 17], carried out at 2.32 and 8.55 GHz, Popov and Kovalev [15] determined the average size of the central component (core) of a compact radio source to be 2.6 pc. The resulting angular sizes [15, Fig. 3] yield a range of lin-

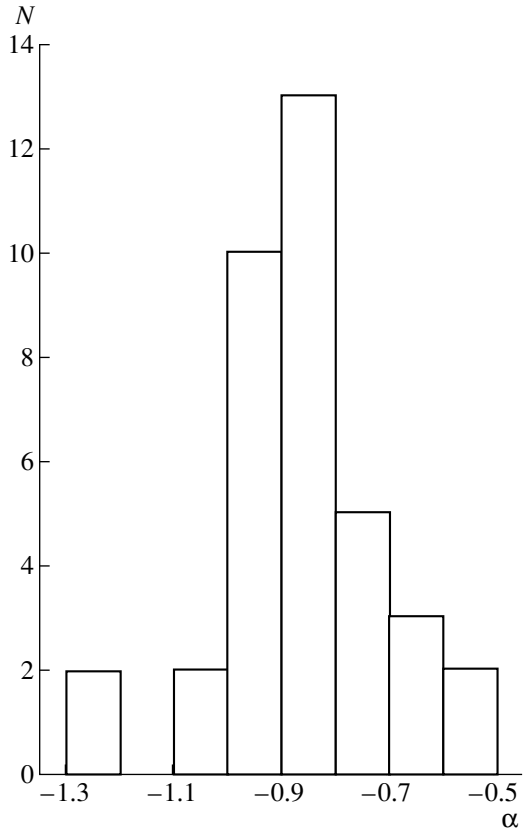

Fig. 3. Distribution of spectral indices α for the extended components.

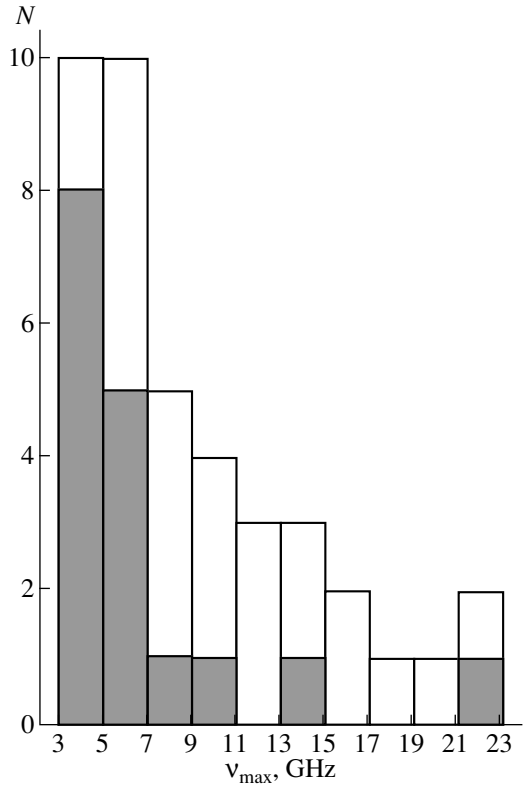

Fig. 4. Distribution of peak frequencies ν_{max} for the spectra of compact components. The sources that had type-5 spectra prior to the component separation (spectra with a flux maximum at 3–23-GHz) are shaded.

Table 3. Spectral parameters of sources with separated components

Name	R.A. (1950.0)	Dec. (1950.0)	Identification	z	S_{max}, mJy	ν_{max}, GHz	A
1	2	3	4	5	6	7	8
0002 + 051	00 02 46.42	05 07 28.00	Q	1.899	226	4.669	–0.801
0019 + 058	00 19 58.12	05 51 24.50	L		286	11.985	–1.280
0026 + 048	00 26 29.11	04 53 00.10	Q	1.633	327	5.611	–1.260
0027 + 056	00 27 11.25	05 38 01.59	Q	1.314	537	22.737	–2.299
0119 + 041	01 19 21.25	04 06 42.02	Q	0.637	1549	12.376	–0.898
0146 + 056	01 46 45.45	05 40 59.59	Q	2.345	1374	7.696	–0.740
0152 + 043	01 52 27.98	04 23 46.71	Q	1.132	256	4.470	–0.735
0231 + 045	02 31 30.47	04 33 39.00	Q	2.06	282	3.085	–1.065
0258 + 058	02 58 55.14	05 50 38.33	Q	2.313	294	4.300	–1.076
0303 + 051	03 03 09.95	05 11 59.35			282	4.657	–0.365
0351 + 045	03 51 46.10	04 32 38.00			239	5.596	–0.587
0355 + 055	03 55 06.68	05 33 55.41			275	6.206	–0.440
0357 + 057	03 57 32.15	05 42 17.70	Q	0.761	467	13.634	–1.192
0409 + 044	04 09 59.90	04 29 56.00			231	5.158	–0.882
0423 + 051	04 23 57.20	05 11 49.00	Q	1.333	574	3.050	–1.479
0430 + 052	04 30 31.51	05 14 59.43	G	0.03	4140	7.942	–0.707
0506 + 056	05 06 45.81	05 37 50.96	L		500	11.203	–0.632
0718 + 042	07 18 45.60	04 12 42.00			578	22.663	–0.753
0801 + 044	08 01 19.40	04 29 36.01			197	4.851	–0.533
0805 + 046	08 05 19.23	04 41 18.30	Q	2.876	383	7.454	–0.729
0830 + 040	08 30 41.56	04 00 49.40			375	17.506	–0.671
1036 + 054	10 36 10.95	05 28 06.52			716	15.904	–1.040
1117 + 044	11 17 08.00	04 26 45.00			211	6.895	–1.046
1204 + 057	12 04 24.42	05 46 33.39			281	13.684	–1.391
1219 + 054	12 19 19.29	05 26 54.39			135	8.369	–0.498
1358 + 046	13 58 17.33	04 39 59.58			126	6.696	–0.876
1402 + 044	14 02 29.91	04 29 54.38	Q	3.202	1071	6.278	–2.274
1509 + 054	15 09 12.17	05 29 28.98	G		916	13.198	–0.390
1541 + 050	15 41 05.00	05 01 44.40	G	0.0398	251	9.926	–1.318
1548 + 056	15 48 06.90	05 36 10.89	Q	1.422	3475	9.793	–0.453
1614 + 051	16 14 08.52	05 06 55.04	Q	3.209	889	5.903	–0.485
1646 + 042	16 46 57.92	04 17 09.58			228	7.922	–0.501
1656 + 053	16 56 05.63	05 19 46.70	Q	0.887	1062	6.396	–1.247
1725 + 044	17 25 56.37	04 29 27.70	Q	0.293	1330	19.079	–0.712
1758 + 046	17 58 36.30	04 38 46.00			249	4.090	–1.156
1926 + 050	19 26 51.69	05 01 41.85			239	9.092	–0.931
2019 + 050	20 19 06.56	05 05 37.66			461	4.227	–0.656
2149 + 056	21 49 07.94	05 38 07.33	Q	0.740	901	4.070	–0.822
2243 + 047	22 43 21.51	04 45 07.68	Q	1.091	366	15.072	–0.869
2259 + 058	2 59 21.58	05 53 05.06			340	6.160	–1.060
2346 + 052	23 46 47.73	05 17 58.93	L		345	10.739	–0.682

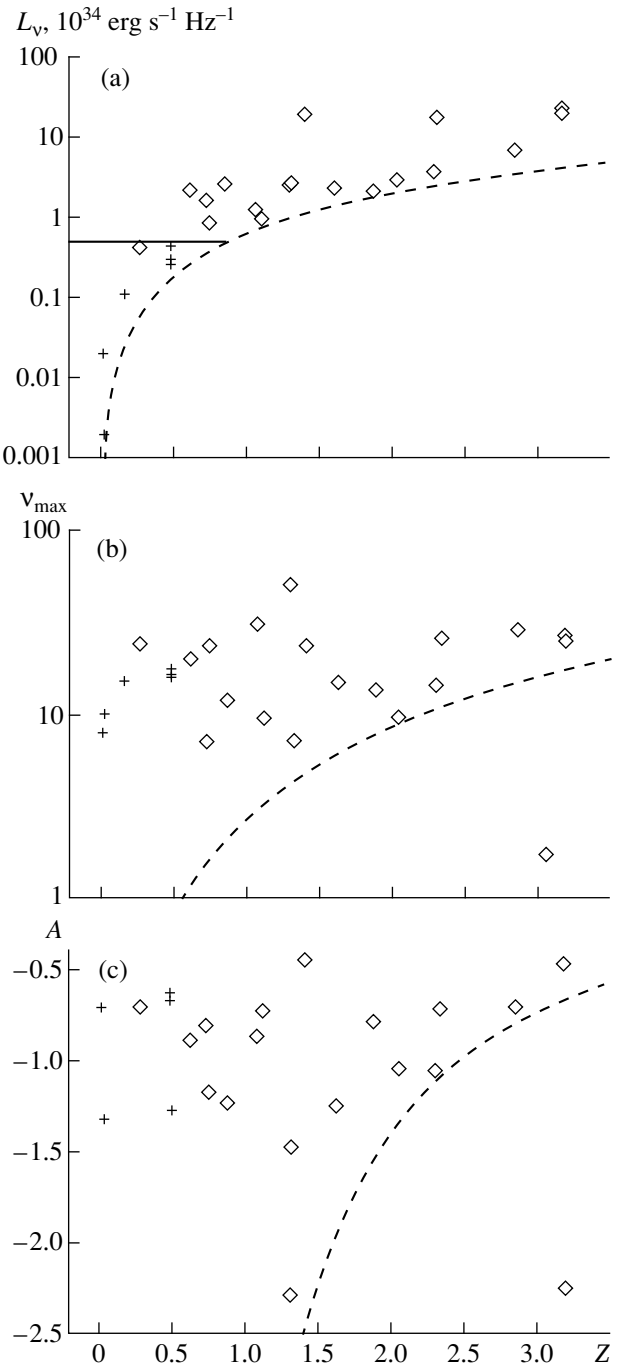

Fig. 5. Spectral characteristics of compact components (diamonds: quasars; crosses: BL Lac objects and galaxies) as functions of redshift z: (a) absolute spectral radio luminosity at the peak frequency L_{max} (dashed line: minimum luminosity that can be detected for sources in the given flux-limited sample; horizontal segment: cutoff of the quasar luminosity function at $L_{min} \sim 5 \times 10^{33}$ erg s^{-1} Hz^{-1}); (b) peak frequency in the source rest frame (dashed curve: dependence of the form $l_{bol}^2/(1+z)$, limiting ν_{max} from below); (c) spectrum curvature in the optically thin region (the parameter A) (dashed curve: dependence of the form $l_{bol}^2/(1+z)$, limiting A from below).

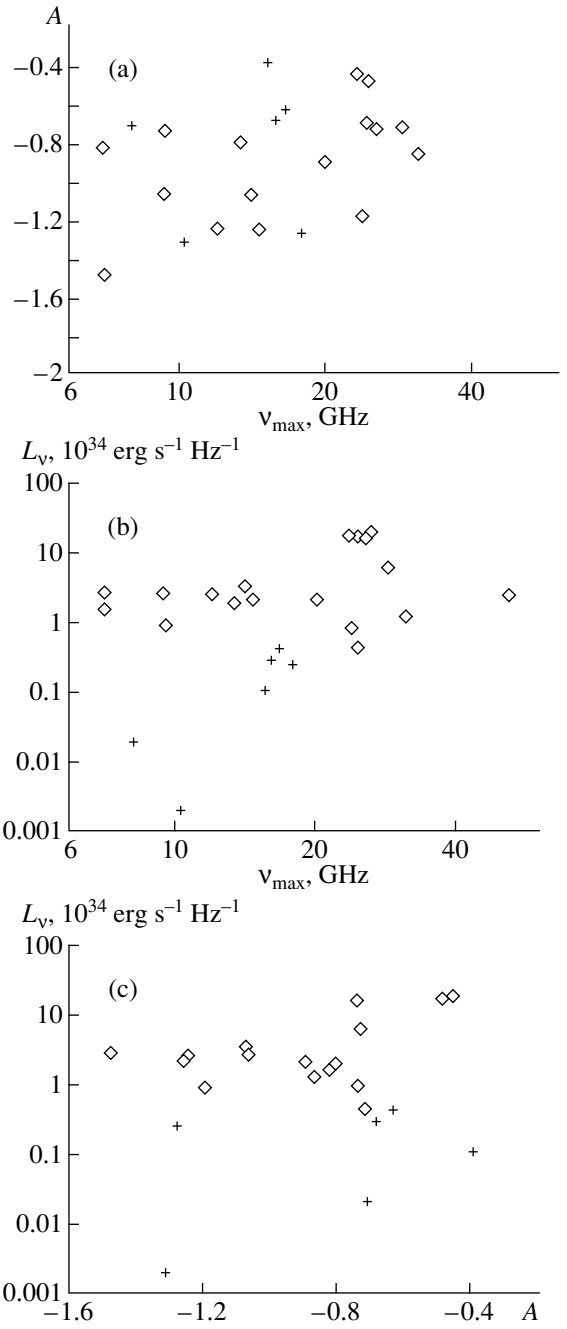

Fig. 6. Spectral characteristics of compact components (diamonds: quasars; crosses: BL Lac objects and galaxies): (a) spectrum curvature in the optically thin region (A) as a function of the peak frequency ν_{max}; (b) absolute radio luminosity at the peak frequency L_{max} as a function of peak frequency ν_{max}; (c) absolute radio luminosity L_{max} as a function of spectrum curvature A.

ear dimensions from 0.8 pc (boundary of the core) to 6.7 pc (components are well separated). Thus, there exist natural upper and lower boundaries for the size distribution for compact components, which likely depend on the type of radio source (QSO, RG, BL) but not on the luminosity of the object.

Table 4. Data on peak frequencies

Radio sources	N	$\bar{z}$	σ	Observer's frame		Source frame	
				$\bar{\nu}_{max}$, GHz	σ	$\bar{\nu}_{max}$, GHz	σ
All QSOs	18	1.62	0.89	8.65	5.7	20.0	11.0
QSO ($z > 1.4$)	9	2.33	0.65	6.1	2.0	20.2	7.1
QSO ($z < 1.4$)	9	0.91	0.34	11.2	7.0	21.0	14.0
L	3	(0.5)	–	11.3	0.6	17.0	1.0

Table 5. Parameters of the sources whose spectra could not be separated into components

Name	R.A. (1950.0)	Dec. (1950.0)	Identification	z	A_0	A_1	A_2
1	2	3	4	5	6	7	8
0237 + 040	02 37 14.51	04 03 29.84	Q	0.978	2.979	−0.158	−0.044
0320 + 045	03 20 37.00	04 35 45.00			2.368	−0.567	0.213
0348 + 049	03 48 15.32	04 57 19.67			2.868	−0.449	
0425 + 048	04 25 08.53	04 50 30.54			2.942	−0.577	0.336
0502 + 049	05 02 43.86	04 55 38.51	Q	0.954	3.012	−0.081	−0.066
0731 + 050	07 31 18.40	05 02 55.86			2.433	−0.071	0.122
0806 + 059	08 06 04.03	05 59 24.05			2.775	−0.721	0.243
0829 + 046	08 29 10.89	04 39 47.63	L	0.18			
0858 + 050	08 58 34.06	05 00 47.10			2.088	0.627	−0.192
1013 + 054	10 13 26.63	05 28 00.50			2.576	−0.930	0.559
1015 + 057	10 15 51.24	05 45 32.90					
1142 + 052	11 42 47.12	05 12 06.03	Q	1.342	2.897	−0.658	0.308
1219 + 044	12 19 49.15	04 29 54.03	Q	0.965	2.799	−0.393	0.585
1228 + 045	12 28 54.40	04 34 36.00			2.490	−0.020	
1237 + 049	12 36 59.94	04 59 33.30			2.624	0.030	
1421 + 048	14 21 38.52	04 48 29.06			2.360	−0.286	0.171
1456 + 044	14 56 29.57	04 28 13.65			3.070	−0.529	0.453
1542 + 042	15 42 29.73	04 17 07.55	Q	2.182	2.973	−0.803	0.398
1557 + 0.43	15 57 33.00	04 21 21.21			2.447	−0.643	0.401
1614 + 042	16 14 44.02	04 16 00.88			2.562	−0.410	−0.055
1642 + 054	16 42 28.53	05 24 06.05			2.878	−0.784	0.237
1936 + 046	19 36 01.87	04 41 19.48			2.742	−0.315	0.194
2114 + 048	21 14 50.80	04 50 27.71					
2121 + 053	21 21 14.82	05 22 27.10	Q	1.941			
2144 + 042	21 44 24.22	04 13 30.60			1.707	0.769	−0.173
2201 + 044	22 01 45.75	04 25 32.46	G	0.028	2.943	−0.643	0.275
2318 + 049	23 18 11.93	04 57 23.63	Q	0.623	2.802	0.144	0.070
2355 + 042	23 55 56.00	04 13 30.00			2.423	−0.423	0.299

Note: Notation in column 4: (Q) QSO, (L) BL Lac object.

Figure 5c demonstrates the lack of a correlation between the spectral curvature in the optically thin region (A) and the redshift. A dependence of the form $l_{bol}^2/(1+z)$ is also shown in Fig. 5c by the dashed curve. The lack of such a correlation is equivalent to the lack of a correlation between the luminosity and spectral index in the optically thin region of the spectrum.

Landau *et al.* [14] reported a significant correlation between the spectral parameters A, B, and C [see (2)] based on simultaneous observations over a wide frequency range (from radio to optical) for a sample of 15 sources. A correlation between the peak flux density S_{max}, peak frequency ν_{max}, and spectral index α in the optically thin region of the spectrum was found in [18].

The parameters C and B correspond to S_{max} and ν_{max}, while the parameter A characterizes the steepness of the spectrum, and can be related to the spectral index.

We have also done a correlation analysis between L_{max} (the absolute luminosity at the maximum of the spectrum), ν_{max}, and A. The input data are presented in Fig. 6. We find a possible correlation between the luminosity and peak frequency (correlation coefficient 0.365), with a confidence level of 10%. The same correlation coefficient for the flux density S_{max} and peak frequency ν_{max} was obtained in [18], though [18] deals with more powerful sources, which have a wider spread of peak frequencies.

We found no correlation between L_{max} and A or between A and ν_{max}, though in [14, 18] such correlations were found with significance levels smaller than 0.01%. What is the origin of this large difference in the properties of these spectral parameters? The strong correlation between S_{max} and α found in [18] is to a considerable extent the result of selection effects: According to the selection criteria imposed, low-luminosity sources with steep spectra were not included in the sample. In our sample, we have made no selection with respect to spectral index, since the sample was formed in accordance with a limiting flux density at a lower frequency than the peak frequencies for nearly all the sources.

We found no correlation between α and ν_{max}, since this correlation is due to objects with high peak frequencies, which are missing from our sample due to the restricted frequency range for the observations and the lower luminosities of the objects. This correlation vanishes after excluding objects with $\nu_{max} > 50$ GHz from the data of [18].

Thus, it is very probable that the distribution of source linear dimensions does not depend on luminosity.

Spectra of the remaining sources. Table 5 lists 28 sources in which we could not separate the spectra into power-law and compact components (objects with spectra of types 1–3). We approximated the spectra of these sources by a logarithmic parabola

$$\log S = A_0 + A_1 \log\nu + A_2 \log\nu^2.$$

For four sources (0829+046, 1015+057, 2114+048, and 2121+053), we were unable to obtain satisfactory approximations. These sources have the largest variability amplitudes among those listed in Table 5. Table 5 contains the source names, right ascensions, and declinations (columns 1–3); identifications and redshifts (columns 4, 5); and approximation coefficients A_0, A_1, and A_2 (columns 5–8). The sources in Table 5 are, on average, fainter in the optical: Almost half the sources are fainter than 20.5^m. Accordingly, redshifts have been measured for less than one-third of these sources (compared to 50% of the sources in Table 3). The mean redshift $\bar{z}$ is 1.0 (with standard deviation 0.7).

The fraction of active objects among these sources is the highest. During the 1.5 years of our observations, we found variability in 60% of these sources. Among the 41 sources with pronounced compact components and peak frequencies lower than 23 GHz, variability was found in only 12 objects. Among the compact components, variable sources have higher peak frequencies: The mean peak frequency $\bar{\nu}_{max}$ is 14 GHz, with $\sigma = 6$ GHz; this considerably exceeds the mean value for the distribution for all the sources ($\bar{\nu}_{max} = 9$ GHz, $\sigma = 5$ GHz).

The variable sources of Table 5 either have even higher peak frequencies or are in a stage of recurrent activity, when several compact components are present simultaneously.

4. CONCLUSIONS

(1) The spectra of the flat-spectrum sources of the complete sample at 0.97–21.7 GHz can be divided into 5 classes. This separation is related to two factors.

The first factor is the peak flux of the extended component at low frequencies compared to the peak flux of the compact component. In sources with spectra of types 2–4 (Fig. 1), the extended component makes the largest contribution to the total emission at frequencies below 4–5 GHz, whereas in sources with spectra of types 1 and 5 (Fig. 1), the emission of the compact component dominates at these frequencies. For 60% of the sources, we could separate the extended and compact components. The spectral-index distribution for the extended components (mean spectral index $\bar{\alpha} = -0.87$, $\sigma_{\bar{\alpha}} = 0.15$) coincides with that for sources with power-law spectra.

The second factor is the activity of a radio source at the epoch of observation. Sources that are at an initial stage of activity—i.e., at an initial phase of evolution of the ejection—have a higher peak frequency and a larger mean relative variability amplitude. These are sources with spectra of types 1 and 2, for which the peak frequency is outside the observed frequency band. Sources with spectra of types 3 and 4 are at a later stage of evolution, their peak frequencies are at centimeter wavelengths, and their variability amplitudes are lower. The mean redshifts of sources with type 1–4 spectra are approximately the same ($\bar{z} = 1.2$–1.3), enabling us to compare frequencies in the observer's frame. This behavior of the variable sources is consistent with all standard variability models.

(2) As a rule, sources with large redshifts ($\bar{z} = 2.03$) have no appreciable extended component, a very small scatter of peak frequencies, and little or no variability on timescales of 1.5 years.

(3) We have confirmed the weak correlation between the luminosity at the peak frequency L_{max} and the peak frequency ν_{max} in the spectra of compact components found in [14, 18]. We suggest that this correla-

tion is a consequence of the lack of dependence of the distribution of source linear dimensions on their luminosity.

(4) We have found no correlation between L_{max} and the curvature parameter A or between A and ν_{max}. We have demonstrated that the correlations between these parameters found in [18] are a consequence of selection effects.

ACKNOWLEDGMENTS

This work was supported by the Russian Foundation for Basic Research (project no. 98-02-16428), a grant of the "Universities of Russia" (no. 5561), and a grant of the Federal Program in Science and Technology "Astronomy" (no. 1.2.5.1).

REFERENCES

1. G. B. Sholomitskiĭ, IAU Bull. Variable Stars **83**, 1 (1965).
2. W. A. Dent, Science **148**, 1458 (1965).
3. M. Bondi, L. Padrielli, R. Fanti, *et al.*, Astron. Astrophys., Suppl. Ser. **120**, 89 (1996).
4. B. H. Andrew, J. M. MacLeod, G. A. Harvey, and W. J. Medd, Astron. J. **83**, 863 (1978).
5. H. D. Aller, M. E. Aller, G. E. Latimer, and P. E. Hodge, Astrophys. J., Suppl. Ser. **59**, 513 (1985).
6. H. Terasranta, M. Tornikoski, E. Valtaoja, *et al.*, Astron. Astrophys., Suppl. Ser. **94**, 121 (1992).
7. G. R. Romero, G. Surpi, and H. Vicetich, Astron. Astrophys. **301**, 64 (1995).
8. V. R. Amirkhanyan, A. G. Gorshkov, A. A. Kapustkin, *et al.*, *Catalog of Sources from Zelenchuk Sky Survey in the Declination Range 0°–14°* [in Russian] (Mosk. Gos. Univ., Moscow, 1989).
9. A. M. Botashev, A. G. Gorshkov, V. K. Konnikova, and M. J. Mingaliev, Preprint No. 132, SAO RAN (Spec. Astrophys. Obs., Russian Academy of Sciences) (1998).
10. A. G. Gorshkov and V. K. Konnikova, Astron. Zh. **72**, 291 (1995).
11. R. A. Nizhel'skiĭ, Otchet Spets. Astrofiz. Obs. (1996), p. 57.
12. A. B. Berlin, A. A. Maksyasheva, N. A. Nizhel'skiĭ, *et al.*, in *Proc. XXVII Radio Astronomy Conference*, St. Petersburg (1997), Vol. 3, p. 115.
13. G. A. Seielstad, T. J. Pearson, and A. C. S. Readhead, Publ. Astron. Soc. Pac. **95**, 842 (1983).
14. R. Landau, B. Golisch, T. J. Jones, *et al.*, Astrophys. J. **308**, 78 (1986).
15. M. V. Popov and Yu. Yu. Kovalev, Astron. Zh., 2000 (in press).
16. A. L. Fey, A. W. Clegg, and E. B. Fomalont, Astrophys. J., Suppl. Ser. **105**, 299 (1996).
17. A. L. Fey and P. Charlot, Astrophys. J., Suppl. Ser. **111**, 95 (1997).
18. E. Valtaoja, S. Haarala, H. Lehto, *et al.*, Astron. Astrophys. **203**, 1 (1988).

Translated by G. Rudnitskiĭ

Astronomy Reports, Vol. 44, No. 6, 2000, pp. 365–375. Translated from Astronomicheskiĭ Zhurnal, Vol. 77, No. 6, 2000, pp. 420–431.
Original Russian Text Copyright © 2000 by Rostopchina, Grinin, Shakhovskoĭ, Thé, Minikulov.

Photopolarimetric Activity of the Ae Herbig Star SV Cep

A. N. Rostopchina[1], V. P. Grinin[1, 2], D. N. Shakhovskoĭ[1], P. S. Thé[3], and N. Kh. Minikulov[4]

[1]*Crimean Astrophysical Observatory, Nauchnyĭ, Crimea, 334413 Ukraine*

[2]*St. Petersburg State University, Universitetskaya nab. 7/9, St. Petersburg, 199164 Russia*

[3]*Anton Pannekoek Astronomical Institute, University of Amsterdam, Amsterdam, The Netherlands*

[4]*Institute of Astrophysics, Dushanbe, Tajikistan*

Received June 2, 1999

Abstract—We present the results of simultaneous *UBVRI* photometric and polarimetric observations of the Ae Herbig star SV Cep made in 1987–1998. Over these 11 years, only a single deep ($\Delta V > 1^m$) brightness minimum was observed. Near this minimum, the brightness decrease was accompanied by an increase of the linear polarization, as is typical of young UX Ori stars. The photometric observations of SV Cep indicate reversals of the color tracks in brightness minima, as is common for stars of this type, as well as variations of the slopes of the color tracks during and after minima. This provides evidence that the circumstellar dust clouds screening the star differ in their sizes and masses, and also in the optical properties of their dust particles. A Fourier analysis of the brightness variations of SV Cep (including data from the literature) confirms the presence of previously suspected activity cycles with periods $P_1 = 4000^d$ and $P_2 = 670^d$. The polarimetric observations indicate that, along with the inverse correlation between the degree of linear polarization and brightness, the polarization parameters vary on characteristic time scales of 4000 and 1000 days. This suggests the existence of large-scale inhomogeneities in the circumstellar dust disk rotating about the star. © *2000 MAIK "Nauka/Interperiodica".*

1. INTRODUCTION

The present paper continues a series of studies of linear polarization in the most photometrically active young UX Ori stars. As shown in previous studies (see [1] and the reviews [2–4] and references therein), as a rule, the linear polarizations of these stars are inversely correlated with brightness, reaching 5–7% in deep minima. This polarization dependence made it possible to elucidate the origin of photometric activity in these stars: variable extinction in protoplanetary disks. These studies also provided evidence that the high level of photometric activity displayed by UX Ori stars is primarily due to an optimal orientation of their protoplanetary disks relative to the observer; i.e., they are edge-on or oriented at a small angle to the line of sight [2, 3, 5]. This is quite natural for the variability mechanism considered here. Due to this disk orientation, observations of UX Ori stars can be used to investigate the structure of protoplanetary disks and make it possible, in principle, to detect dust condensations associated with protoplanets.

The present study is focused on the Ae-Herbig star SV Cep. It is based on the results of photopolarimetric monitoring of the star carried out at the Crimean Astrophysical Observatory for 11 years from 1987 to 1998.

2. SV CEP: BASIC DATA

The spectral type of SV Cep has been determined to be A0III [6–10] and B9–B9.5V [11]. Due to its position in the sky, the variable can be observed essentially throughout the year. In spite of this, photometric observations published by the time of writing of this paper are quite fragmentary [12–18] (Fig. 1). The *V* brightness of the star ranges from $10^m.35$ to $12^m.15$ [19].

A normalized histogram of the photometric activity of SV Cep constructed from our data (see our electronic Table 1 accessible at ftp://cdsarc.u-strasbg.fr/pub/cats/J) and other sources [13–18, 20, 21] (Fig. 2) indicates that deep brightness minima are very rare. Wenzel [12, 13] and Kardopolov *et al.* [16–18] suggested the presence of several brightness-variability components with amplitudes from 0^m2 to 1^m0 on time scales from hours to years.

In his analysis of photographic observations of SV Cep made since 1896, Friedemann *et al.* [11] identified another component of the variability: a long-term brightness decrease. From 1896 to 1908, the brightness varied in the range 9^m5–10^m5; i.e. the star was, on average, more than 1^m(!) brighter. According to Minikulov *et al.* [22], who studied photographic observations of the star obtained over roughly 40 years, wavelike oscillations with amplitude $\Delta m \sim 0^m5$ were observed near the bright state. Cyclicity of the brightness variability of SV Cep with a period of about 700 days was suggested in [17].

The star has an IR excess [23, 24] due to thermal radiation by the circumstellar dust. Figure 3 presents the spectral energy distribution for SV Cep in its brightest state in the *UBVRI* bands, constructed from the data in our electronic table (filled triangles) and the data of [23, 24] (hollow triangles and circles). The ratio of the

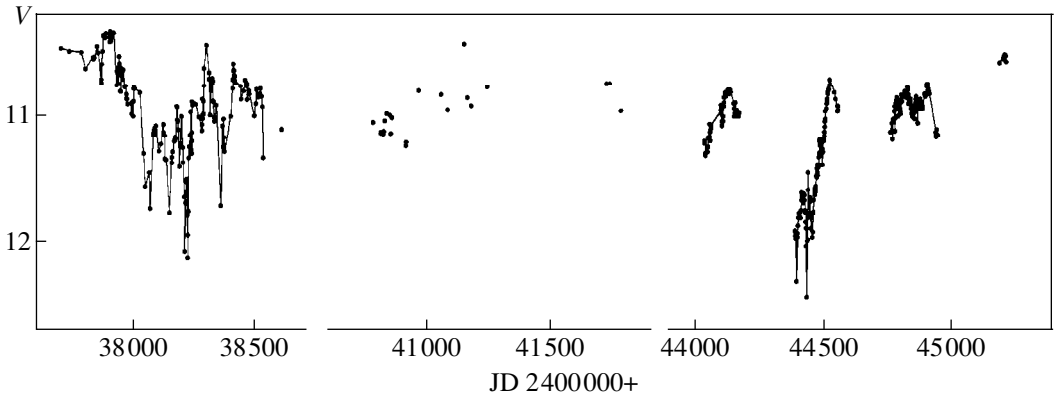

Fig. 1. Light curve of SV Cep obtained from published photoelectric data from various studies (see the text).

IR excess and the intrinsic luminosity of the star is roughly 25% for spectral type B9V and roughly 40% for spectral type A0III, similar to the values for other UX Ori stars [2]. We were not able to find any published data on the linear polarization of SV Cep.

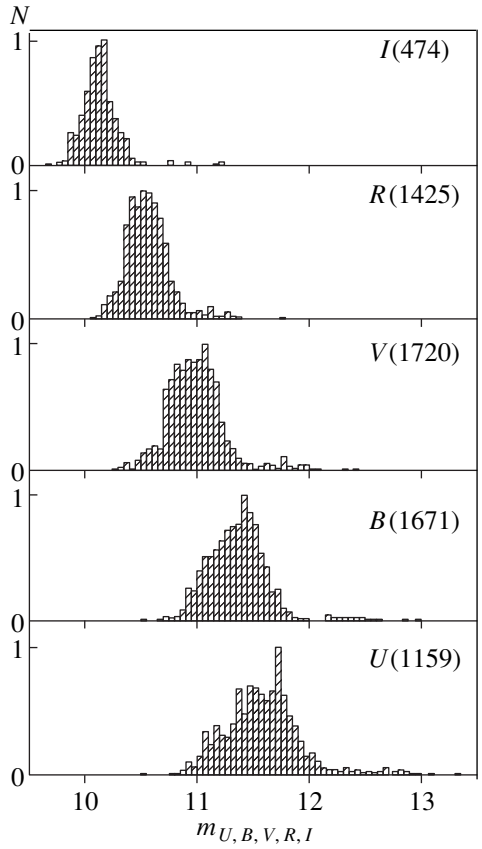

Fig. 2. Normalized histogram of the *UBVRI* photometric activity of SV Cep based on data taken from the literature [13–18, 20, 21] and from the present study. The number of points for each band used to construct the histogram is given in parentheses. Each point corresponds to a single observation in a night.

Published spectral observations of SV Cep are limited primarily to the region of H_α [10, 25–28]. As for other Ae/Be Herbig stars, this line is variable in the spectrum of SV Cep. According to [26], it possesses a two-component profile with $V/R \simeq 1.8$–1.9 and an equivalent width $W(H_\alpha)$ of about 20 Å; the observations of [28] indicate a two-component and nearly symmetric profile with $W(H_\alpha)$ about 13 Å; and the data of [27] show a single-component line profile with $W(H_\alpha)$ from 14.6 to 17.2 Å on different nights.

In [29], we determined the position of SV Cep in the HR diagram and estimated the star's basic properties: $\log(L_*/L_\odot) = 2.04$, $M_* = 3.1M_\odot$, $R_* = 3.6R_\odot$, and an age of 10^6 years. Therefore, although SV Cep is not associated with any bright nebula [30], its properties do not differ from those of classical Ae/Be Herbig stars.

3. OBSERVATIONS

Our observations of SV Cep at the Crimean Astrophysical Observatory began in 1987. We used the *UBVRI* photometer–polarimeter of the University of Helsinki [31] mounted on the 125-cm CAO telescope. This detector records the brightness and polarization of an object simultaneously in five bands. The effective wavelengths of the photometric system are close to those of the standard Johnson system; all photometric observations were reduced to the standard system. For nights with stable opacity, the comparison stars b and c [32] were tied to the photometric standard HD 218209. We present the *UBVRI* magnitudes for the comparison stars in Table 1.

As a rule, on nights with good images, we used a 10″-diameter diaphragm; on other nights, we used a 15″ diaphragm. Our mean photometric errors are $0\overset{m}{.}015$ in *U–B* and less than $0\overset{m}{.}01$ for the other color indices and the *V* band.

Polarimetric observations of SV Cep were made simultaneously with the photometric observations in all five bands (see our electronic table). Depending on the

observing conditions and the brightness of the star, from four to 30 measurements of the Stokes parameters were made in a night. We determined the instrumental polarization and zero point of the polarization position angle from observations of standard stars.

4. RESULTS OF THE OBSERVATIONS

Figure 4 presents the light curves and polarization parameters for our data. Over the 11 years of monitoring, we detected only one minimum with amplitude $\Delta m > 1^m$ and several cases of brightness decreases with $\Delta m < 1^m$.

We can see from Fig. 4 that the star does not have a stable bright state. Its brightness varies virtually continuously, with slow oscillations with amplitudes up to 1^m superimposed by rapid variations with amplitudes up to $\simeq 0^m3$. Comparison of our photometric observations with previously published SV Cep light curves [12–18] (Fig. 1) shows that, in spite of clear differences, all three deep minima observed over 36 years display a common feature—their duration. For the first and third minima [12–19], this was roughly 500 days. The second minimum was not observed in its entirety; however, the period of egress from minimum alone was roughly 100 days. As noted in [31], the interval between the first and second minima was roughly 6200 days, while that between the second and third minima was 5800 days. Given the long durations of the minima, this suggests some periodicity in their occurrence.

Figure 5 presents color–magnitude diagrams plotted using our data (see the electronic table). As noted in [12], *U–B* and *B–V* vary little during minima; i.e., they correspond to almost neutral absorption. This proved to be true only for some minima. Figure 5 also presents all four observed minima for SV Cep: one observed by Wenzel *et al.* [12–14] in the *UBV* bands (JD 38197–38235, hollow triangles), another observed by Kardopolov *et al.* [16–18] in the *BVR* bands (JD 44420–44520, hollow diamonds), and two more observed by us in the *UBVRI* bands (JD 49628–49774, filled circles and JD 49938–49970, filled squares). We can see that the slopes of the color tracks are different in different minima. In addition, a weakly pronounced reversal of the color tracks can be seen in both blue and red colors.

We can see clearly in Fig. 4 an inverse correlation between the brightness and the degree of linear polarization. In the deepest minimum, the degree of polarization increased to 3.5%, and the polarization position angle decreased by 20°. Similar variations of the degree and angle of the linear polarization were also observed in two subsequent minima with smaller amplitudes.

Figure 6 presents the dependence of the degree of polarization on the brightness of the star in all the *UBVRI* bands. Despite the appreciable scatter of the points, the nonlinearity of the polarization variations during periods of brightness decrease can clearly be seen; this is characteristic of models with variable circumstellar extinction [1, 2]. The small number of deep minima observed prevents us from tracing the polarization–brightness dependence over the entire range of brightness variations of the star.

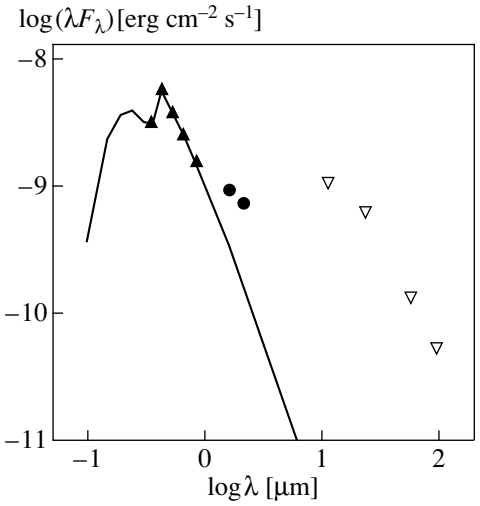

Fig. 3. Spectral energy distribution of SV Cep in the bright state. The thin curve displays the spectral energy distribution of an A0III star according to a Kuruzc model. See the text for details.

Figure 7 presents a diagram of the Stokes parameters P_x and P_y in the *V* band. We can see that the variations of the Stokes parameters occur primarily along one direction, though with a large scatter. Points at the lower end of the diagram correspond to the bright state of the variable, while those above and to the right correspond to brightness minima. The scatter of the points in Figs. 6 and 7 is the result of fluctuations in the scattered radiation due to inhomogeneities in the structure of the circumstellar disks [4].

The typical wavelength dependence of the linear polarization P_λ in various brightness states is presented in Fig. 8. We can see that the degree of polarization is almost independent of wavelength within the observational errors. In addition, the P_λ dependence varies only slightly as the brightness decreases. A similar pattern was observed for another UX Ori star, WW Vul [34]; as shown in [35], it is characteristic of circumstellar dust shells consisting of large grains. At the same time, unlike WW Vul, SV Cep's polarization position angle varies slightly (by up to 15–20°) from the *I* to the *B* band in brightness minima (see electronic table). This suggests that the observed polarization of the star is the

Table 1. Magnitudes of the comparison stars for SV Cep

Comparison star	*V*	*B–V*	*U–B*	*V–R*	*V–I*
b	10.767	0.397	0.267	0.378	0.597
c	11.275	0.733	0.384	1.160	1.194

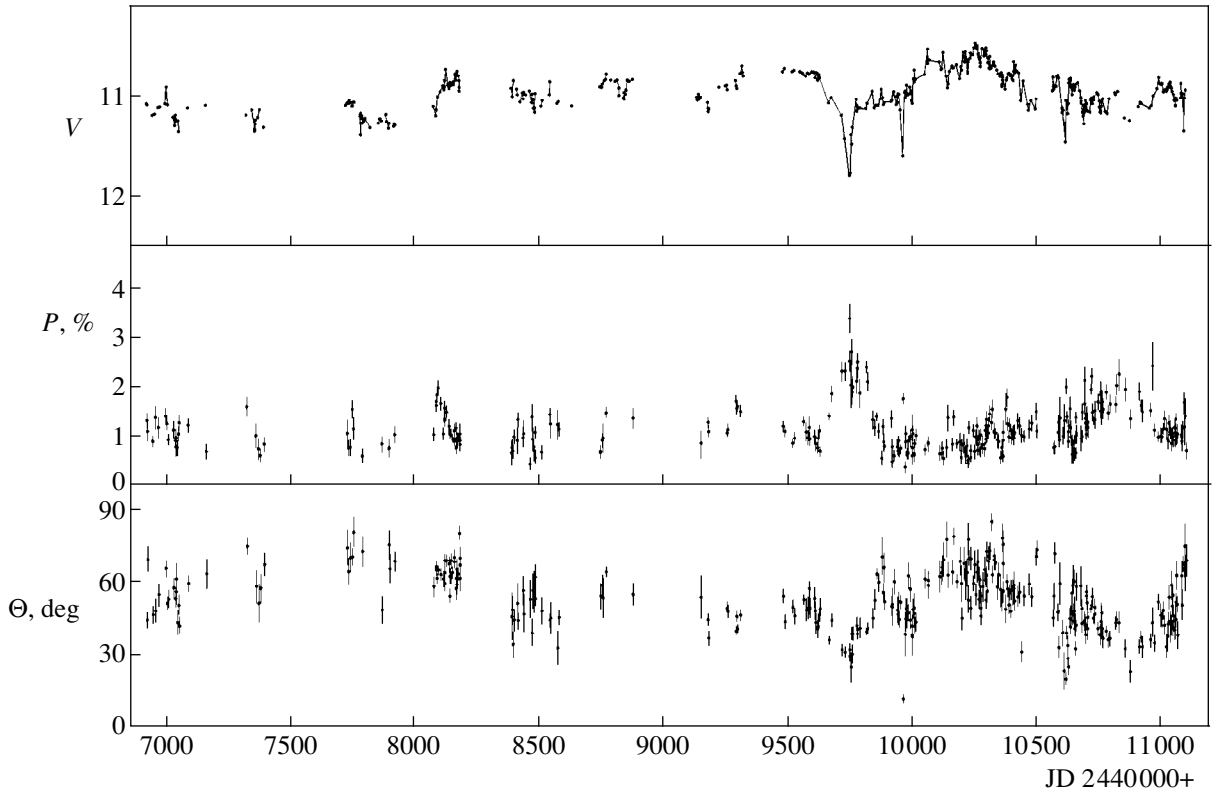

Fig. 4. The curves of *V*-band brightness, degree of polarization, and polarization position angle constructed from our data (see our electronic table).

sum of two components with different polarization position angles.

5. DISCUSSION

5.1. Photometry

We have compared our photometry for SV Cep with the results obtained by other authors. The color–magnitude diagrams constructed using our observations are in good agreement with the observations of [12–14, 20]. Some photometric observations [16–18] indicate a different slope for the color tracks, especially in the (*B–V*)–*V* diagram. It is hard to tell whether this difference is real or is due to errors in reducing the magnitudes to the standard system. The fact that we have not found any systematic differences between our data and the data of Kardopolov *et al.* [16–18] for other common stars in our programs argues that the observed differences are real. In addition, the variability of the color indices within our sample supports the reality of the color-track divergences in these minima. This variability has two components: differences of the color track slopes in different minima and parallel shifts of the color tracks as a function of time, primarily in the vertical direction (Fig. 5).

The variation of the color-track slopes in different is most pronounced at blue wavelengths. For example, the slope for *U–B*, $\alpha = \Delta(U - B)/\Delta V$, varies from 0.07 to 0.18, while the slope for *B–V* varies from 0.05 to 0.17. The color-track shift is most clearly visible at red wavelengths (*V–R* and *V–I*). This shift is also present at blue wavelengths but is less pronounced due to the general "smearing" of the color tracks, whereas the red color-track slopes are less variable. The times corresponding to parallel shifts of the color tracks do not seem to be related to any global variations in the light curve: the first color-index shift occurred as the brightness of the star was increasing slightly (JD ~ 2448100), while the second occurred after an egress from minimum brightness (JD ~ 2450150), as SV Cep was approaching its maximum brightness level.

One rather obvious origin for the color-track slope variation is differences in the optical properties of the dust grains in different dust clouds crossing the line of sight. Shifts of the color tracks (with their slopes remaining constant) are due to slow variations of the level of the bright state of the star (Fig. 4). Both of these mechanisms ultimately result in a large scatter of the points in the color–magnitude diagrams (Fig. 5).

5.2. Cyclicity of the SV Cep Brightness Variations

The collected photometric data enabled us to search for periodicity in the slow brightness variations of SV Cep. For this purpose, we removed the brightness

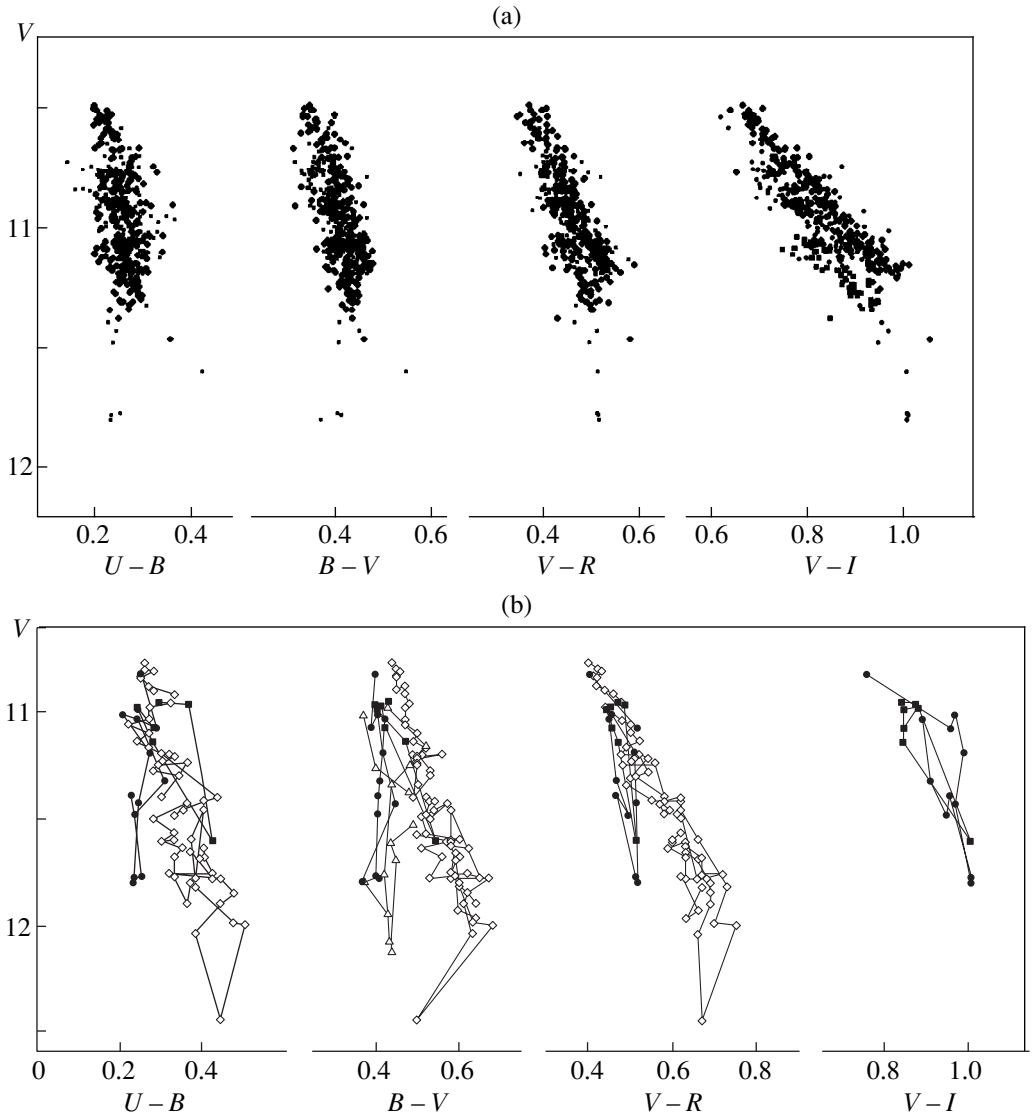

Fig. 5. Color–magnitude diagrams for SV Cep: (a) for our data, (b) for the deepest minima (see the text).

minima ($V \le 1\overset{m}{.}4$) from the photometric sequence to be analyzed. A periodogram analysis (Fig. 9) was performed using the ISDA package [35]. The period search technique is described in more detail in [33, 37].

A period of roughly 700 days in the brightness variations of SV Cep was suspected earlier in [17]. In [33], we suspected periods of 3920, 649, and 489 days in the brightness variability outside of minima. When we added our 1998 observations and the observations of Shevchenko *et al.* from the database of Herbst *et al.* [20] to the photometric data considered in [33], the 489-day peak disappeared from the periodogram (Fig. 9), while the two other peaks, P_1 and P_2, remained. The minor changes in the values for these periods (4000 and 670 days, respectively) are within the errors. Figure 9 presents the SV Cep light curve in the *V* band outside of minima folded with these periods. Note that one of the derived periods (670 days) is very close to that suspected in [17] and appears to be real.

This analysis demonstrated that the star's brightness variations with a characteristic time scale of 4000 days possess the same amplitude in all photometric bands. These variations give rise to the observed parallel shifts of the color tracks in color–magnitude diagrams.

5.3. Polarimetry

When we compare SV Cep's photopolarimetric variability with that observed for other UX Ori stars [24], it is apparent that they are very similar and can be understood in the framework of the model proposed in [1]. According to this model, the photopolarimetric activity of UX Ori stars is specified by two factors: occultations of the star by dust clouds moving in the

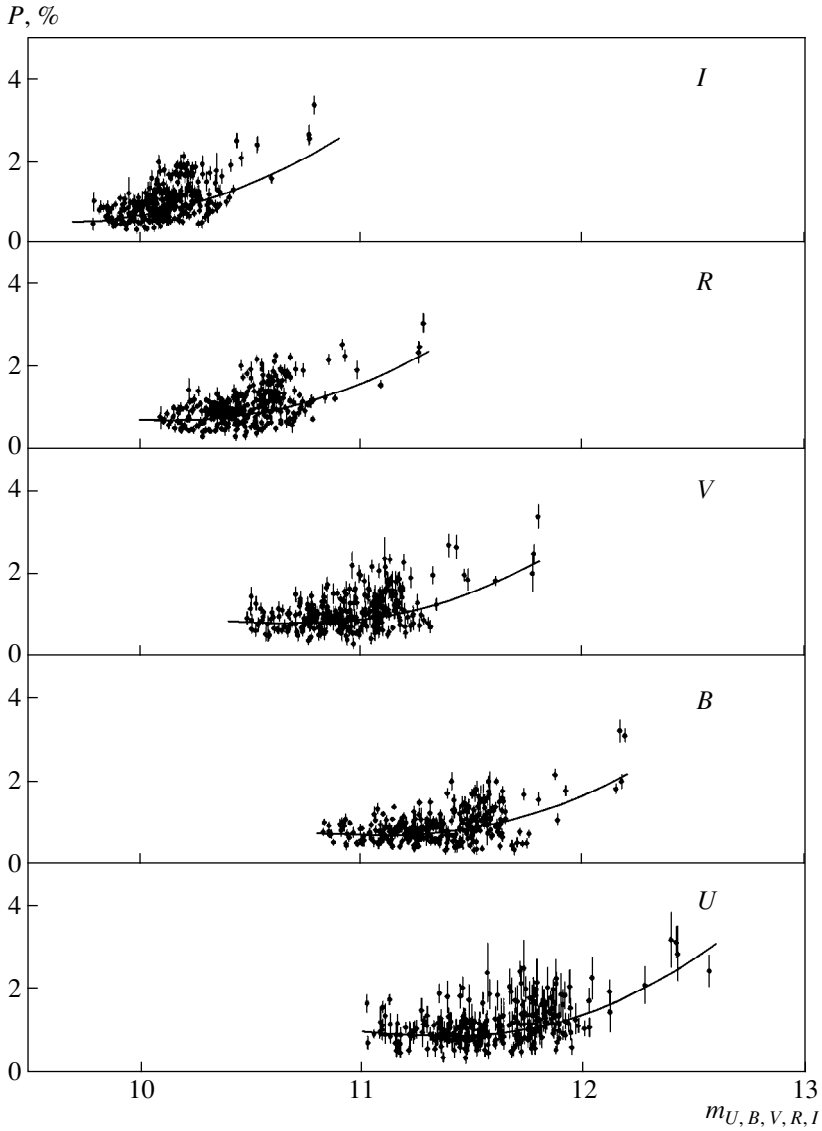

Fig. 6. The dependence of degree of linear polarization on brightness in the *UBVRI* bands. The solid curves show the theoretical dependences yielded by the solution of equation (1) taking into account weights that depend on the accuracy of the observations.

circumstellar disk and the scattered radiation of the circumstellar dust. When a dust cloud obscures the star from the observer, the fraction of direct unpolarized stellar radiation in the total observed radiation decreases, whereas the fraction of polarized radiation scattered on the circumstellar dust increases. This results in an increase of the polarization of the stellar light and a reversal of the color tracks in color–magnitude diagrams during brightness minima (the so-called "blueing effect").

The fact that the absorption is almost neutral at blue wavelengths (Fig. 5) provides evidence that the scattering dust particles are quite large compared to the wavelength of the scattered light, as is confirmed by the wavelength dependence of the polarization of SV Cep (see Section 4). Modeling based on Mee theory indicates that, for a mixture of dust particles with carbon and silicon in equal proportions, the particle size that should give rise to such variability is roughly 0.1 μm. This exceeds the average size of dust particles in the interstellar medium (0.005 μm [38]) by at least an order of magnitude but remains substantially smaller than the sizes determined for the "older" (compared to the UX Ori stars) disks around Vega-type stars (1 μm–1 mm [37]).

Provided the Stokes parameters for the scattered light do not vary with time (including during occultation of the star by dust clouds), variations of the degree of linear polarization should obey the law

$$\mathbf{P}_{obs}(\Delta m) = \mathbf{P}_{is} + \mathbf{P}_{in}(\Delta m), \quad (1)$$

where

$$P_{in}(\Delta m) = P_{in}(0) \times 10^{0.4\Delta m}. \quad (2)$$

Here, $P_{obs}(\Delta m)$ is the observed linear polarization of SV Cep, $P_{in}(0)$ is the intrinsic polarization of the star in the bright state, and P_{is} is the interstellar polarization in the direction toward the star. Writing this equation for all the observations in our electronic table, we obtain a redundant system of equations. We can obtain estimates of the interstellar polarization and intrinsic polarization in the bright state of the star by obtaining a least-squares solution for this system, taking into account the weights for each Stokes parameter separately.

Figure 6 presents the polarization–brightness dependence for SV Cep derived from this solution. We can see that, on the whole, the solution is consistent with the observed polarization–brightness dependence. However, the scatter of points in Fig. 6 is fairly large and exceeds the observational errors. In addition, the degree of interstellar polarization, $P_{IS} = 1.52\%$, and its position angle, $\theta_{IS} = 86.8°$, differ from the average values derived from adjacent stars (see below), and the wavelength dependence $P_{IS}(\lambda)$ is in poor agreement with the formula of Serkovskiĭ for interstellar polarization. As we will see below, this is due to the fact that the Stokes parameters of the scattered radiation vary with time. In this case, the accuracy of the solutions for (1) does not increase as observational data are accumulated.

Table 2 presents the results for the interstellar polarization of nearby stars located at roughly the same distance as SV Cep [11]. We can see that the polarization position angles for the adjacent stars are, to a good accuracy, aligned along the same direction (roughly 50°), providing evidence for the presence of a regular magnetic-field structure in the direction toward SV Cep. Note that the average of the polarization position angles for the nearby stars is close to that of SV Cep itself when it is in the bright state and differs from the position angle of SV Cep at its minimum brightness by roughly 20°.

Agreement of the intrinsic polarization position angle for the scattered radiation of the circumstellar disk and the direction of the local interstellar magnetic field to within 10°–20° has also been noted for other UX Ori stars [2, 3, 40, 41]. This indicates the important role played by the interstellar magnetic field, even as early as during the stage of gravitational contraction of the protostellar clouds. As a result, the rotation axis of the star, and also the symmetry axis of its circumstellar disk, become aligned along the direction of the local magnetic field. Thus, SV Cep can be added to the list of stars for which this interesting property has been revealed by polarimetric observations.

At times of occultation of the star by dust clouds, the polarization of the scattered radiation does not vary, whereas the observed polarization position angle (including the interstellar component) θ can vary only within the aforementioned range of 20°. Indeed, we can see in Fig. 4 a slight variation of θ, not exceeding this range, at minimum brightness (JD 2449750). However, about two months after this minimum, there was a rather abrupt variation of θ by roughly 30°. Further, another brief minimum was observed (JD = 2449950), during which the polarization position angle rotated roughly 35° in the opposite direction. Slower variations of the position angle by more than 20° were also observed at other

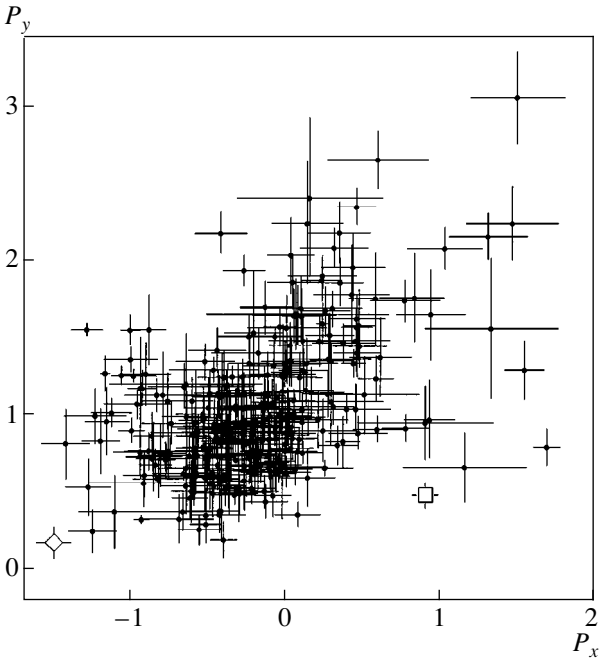

Fig. 7. The Stokes parameters P_x and P_y for the linear polarization of SV Cep. The hollow square and diamond mark the intrinsic polarization in the bright state and the interstellar polarization, respectively, both obtained from the solution of equation (1).

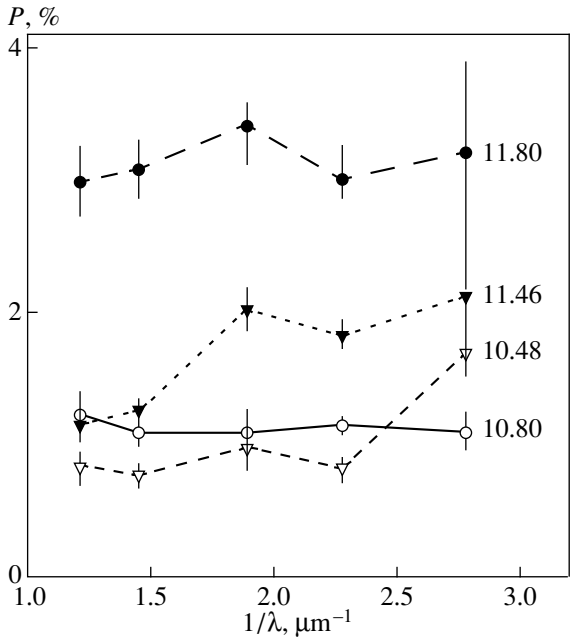

Fig. 8. Wavelength dependence of the linear polarization of SV Cep for various brightness states (indicated on the right).

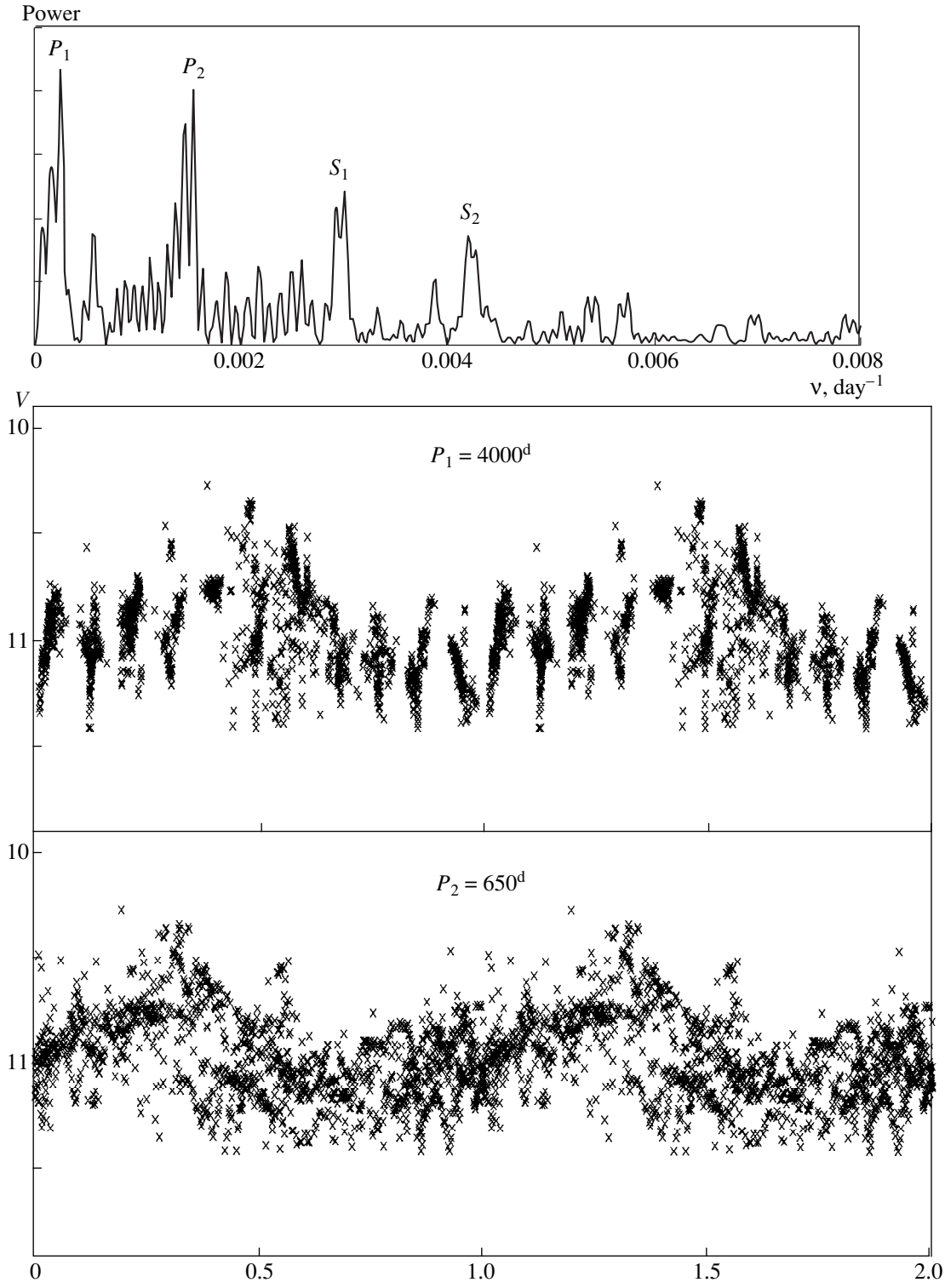

Fig. 9. Results of a period search in the brightness variations of SV Cep (see the text).

times. This behavior suggests that some low-amplitude variable component is present in the polarized radiation of the disk. The wavelike variations of the polarization plane suggest the existence of a period or quasi-period.

Analysis of the time variations of the Stokes parameters showed a trend in the variation of P_x over an interval of roughly 4000 days (Fig. 10). The amplitude of the trend is different in different bands: The largest

amplitude is seen in *I*, its magnitude decreases as we proceed towards bluer wavelengths, and it is not seen at all in *B* and *U*. Note that the characteristic time scale for this variability coincides with the longest of the photometric cycles.

In addition, a Fourier analysis revealed a period of roughly 1100^{d} in the variability of the Stokes parameters, which can be most clearly seen in the time dependence for P_y (Fig. 10). This period corresponds to the interval between polarization maxima observed over the last five years. Unfortunately, our polarimetric observations were less dense in the first few years of the monitoring, so that we can not be sure of the reality of this period. However, such a period is consistent with the observed polarization variations. Further polarimetric observations of SV Cep are clearly required to resolve this question.

Table 2. *V*-band linear polarization of stars in the vicinity of SV Cep

Star	$\alpha_{1950.0}$	$\delta_{1950.0}$	P, %	σP, %	θ, deg	$\sigma\theta$, deg
a	$22^{h}18^{m}57^{s}$	73°45′44″	0.58	0.15	58.9	4.2
b	21 30	51 32	0.64	0.08	35.5	3.5
f	23 18	58 08	0.73	0.13	49.9	6.5
g	24 32	55 12	0.61	0.14	61.1	6.9
j	26 19	48 56	0.32	0.10	52.3	7.0
k	19 06	23 12	1.02	0.12	34.3	3.6
l	20 52	28 04	0.79	0.13	45.0	4.8
s	24 25	21 48	2.50	0.23	44.1	2.8
t	25 45	30 32	1.38	0.22	74.2	4.1
γ	21 39	39 04	1.01	0.12	50.5	3.5
Average			0.96	0.18	50.6	3.2

5.4. Origin of the Photopolarimetric Cycles

What is the origin of the specific features of the photometric and polarimetric behavior of SV Cep? On the one hand, the behavior of the linear polarization of SV Cep during brightness minima is similar to that observed for some other UX Ori stars [2–4, 33, 34, 40, 41]. This suggests that the variations of SV Cep's brightness and intrinsic polarization are primarily due to occultations of the star by opaque dust clouds. On the other hand, together with the minima, we observe variations of the star's photometric and polarimetric properties that display periodic or quasi-periodic components.

In the framework of a variable circumstellar extinction model, such brightness and (possibly) polarization variations reflect the existence of global inhomogeneities rotating around the star in its dust disk. This is also indicated by the results of our recent analysis of cycli-

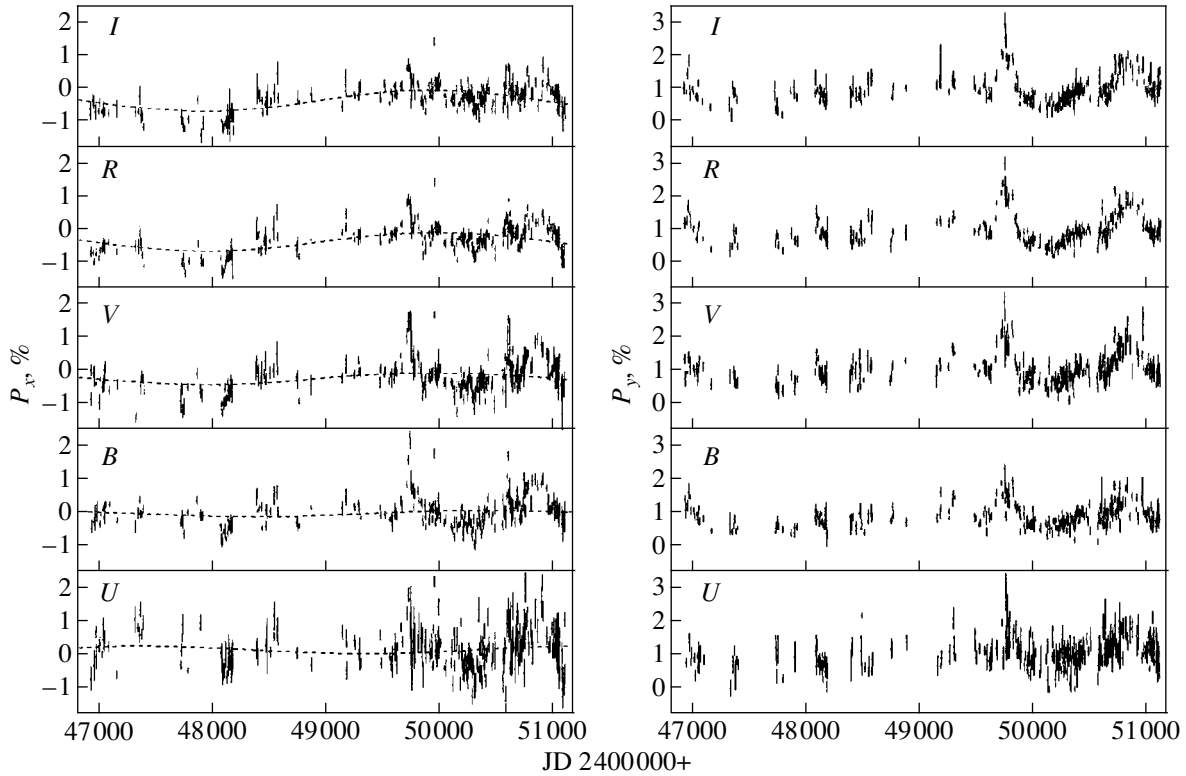

Fig. 10. Time variations of the Stokes parameters P_x and P_y of SV Cep for all five *UBVRI* bands.

cal variations in the brightnesses of other UX Ori stars [33, 37]. Such inhomogeneities could be formed by periodic gravitational perturbations due to the secondary component of a young binary system.

Recent observations (see, for example, [42]) indicate that the fraction of binary and multiple systems among Ae/Be Herbig stars is fairly high (up to 40%). Although all known UX Ori stars, including SV Cep, have been assumed to be single, it seems reasonable to suppose that the fraction of binaries among stars of this subtype is the same as among other Ae/Be Herbig stars. As shown by the calculations of [43], if such a star is binary, there should be density waves and matter flows into the inner parts of the gas–dust disk, which form variations in the radial concentration of dust, which, in turn, affect both the photometric properties of the system and variations of the Stokes parameter of the scattered radiation. This is apparently the reason for the rather large scatter of points in the color–magnitude diagrams of SV Cep (Fig. 5) and the dependence of the degree of polarization on the star's brightness (Fig. 6).

6. CONCLUSION

SV Cep displays all the features distinctive of UX Ori stars, which are due to the presence of inhomogeneous circumstellar gas–dust disks and associated variable circumstellar extinction. In addition, the photopolarimetric activity of SV Cep displays certain unusual features:

–infrequent, long-duration Algol-like minima;

–substantial-amplitude slow brightness variations in the bright state;

–the presence of at least two different characteristic time scales for these variations (4000 and 670 days);

–variability in the observed color–magnitude dependences;

–large-magnitude, possibly cyclical, variability of the linear polarization parameters that does not correlate with brightness.

All these properties suggest an extremely complex and inhomogeneous structure for the circumstellar medium (i.e., the disk), which complicates analyses of the properties of the medium using the simple models that have been successfully applied to other UX Ori stars [2, 35, 41, 44].

We believe investigations of these unusual properties to be interesting both in their own right and as a means to deepen our understanding of the UX Ori phenomenon. For this reason, we consider further studies of SV Cep via both photopolarimetric monitoring and other techniques to be valuable.

ACKNOWLEDGMENTS

This work has been partially supported by INTAS (grant no. 93-2478Ext) and the Russian Foundation for Basic Research (project no. 99-02-18520).

REFERENCES

1. V. P. Grinin, Pis'ma Astron. Zh. **14**, 65 (1988) [Sov. Astron. Lett. **14**, 27 (1988)].
2. V. P. Grinin, N. N. Kiselev, N. Kh. Minikhulov, *et al.*, Astrophys. Space Sci. **186**, 283 (1991).
3. V. P. Grinin, Astron. Astrophys. Trans. **3**, 17 (1992).
4. V. P. Grinin, in *The Nature and Evolutionary Status of Herbig Ae/Be Stars*, Ed. by P. S. Thé, M. Pérez, and E. van den Heuvel (PASP Conf. Ser. 62, 1994), p. 63.
5. A. Natta, V. Grinin, V. Mannings, and H. Ungerechts, Astrophys. J. **491**, 885 (1997).
6. E. A. Kolotilov, Astrofizika **13**, 33 (1977).
7. O. V. Kozlova, Personal communication (1998).
8. A. F. Pugach and G. U. Koval'chuk, Kinematika Fiz. Nebesnykh Tel **7**, 43 (1991).
9. G. U. Koval'chuk and A. F. Koval'chuk, Kinematika Fiz. Nebesnykh Tel **7**, 71 (1991).
10. L. V. Timoshenko, Astrofizika **22**, 51 (1985).
11. C. Friedemann, H.-G. Reimann, and J. Gúrtler, Astron. Astrophys. **255**, 246 (1992).
12. W. Wenzel, Mitt. Veränd. Sterne **5**, 75 (1969).
13. W. Wenzel, Mitt. Veränd. Sterne **6**, 22 (1972).
14. W. Wenzel, J. Dorschener, and C. Freidemann, Astron. Nachr. **292**, 221 (1971).
15. L. N. Mosidze, Byull. Akad. Nauk Gruz. SSR, Abastumanskaya Astrofiz. Obs., No. 37, 13 (1969).
16. V. I. Kardopolov and G. K. Filip'ev, Tsirk. Astron. Inst., Akad. Nauk UzSSR, No. 96, 34 (1981).
17. V. I. Kardopolov, L. V. Timoshenko, and G. K. Filip'ev, Perem. Zvezdy **22**, 137 (1985).
18. V. I. Kardopolov and G. K. Filip'ev, Perem. Zvezdy **22**, 153 (1985).
19. G. H. Herbig and K. R. Bell, Lick Obs. Bull., No. 1111 (1988).
20. W. Herbst, D. K. Herbst, and E. A. Grossman, Astron. J. **108**, 1906 (1994).
21. A. V. Berdyugin, Izv. Krym. Astrofiz. Obs. **87**, 107 (1993).
22. N. Kh. Minikulov, V. Yu. Rakhimov, N. A. Volchkova, and A. I. Pikhun, Astrofizika **36**, 55 (1993).
23. I. S. Glass and M. V. Penston, Mon. Not. R. Astron. Soc. **167**, 237 (1974).
24. C. A. Beichman, G. Neugebauer, H. J. Habing, *et al.*, in *Catalog of Infrared Observations* (NASA Ref. Publ., 1998), Part II, p. 1190.
25. G. V. Zaĭtseva and V. F. Esipov, Astron. Tsirk., No. 712 (1972).
26. G. V. Zaĭtseva and E. A. Kolotilov, Astrofizika **9**, 185 (1973).
27. A. F. Pugach, Astrofizika **29**, 448 (1988).
28. O. V. Kozlova, V. P. Grinin, and A. N. Rostopchina, Astron. Astrophys. **8**, 249 (1995).
29. A. N. Rostopchina, Astron. Zh. **76**, 136 (1999) [Astron. Rep. **43**, 113 (1999)].
30. P. S. Thé, D. de Winter, and M. Pérez, Astron. Astrophys., Suppl. Ser. **104**, 315 (1994).
31. V. Piirola, Ann. Acad. Sci. A **VI**, 61 (1975).

32. A. F. Pugach and G. U. Koval'chuk, Perem. Zvezdy **22**, 9 (1983).
33. A. N. Rostopchina, V. P. Grinin, and D. N. Shakhovskiĭ, Pis'ma Astron. Zh. **25**, 291 (1999) [Astron. Lett. **25**, 243 (1999)].
34. V. P. Grinin, N. N. Kiselev, N. Kh. Minikulov, and G. P. Chernova, Pis'ma Astron. Zh. **14**, 514 (1988) [Sov. Astron. Lett. **14**, 219 (1988)].
35. N. V. Voshchinnikov and V. P. Grinin, Astrofizika **34**, 181 (1991).
36. J. Pelt, *Irregularly Spaced Data Analysis, User's Manual* (1993).
37. V. P. Grinin, A. N. Rostopchina, and D. N. Shakhovskiĭ, Pis'ma Astron. Zh. **24**, 925 (1998) [Astron. Lett. **24**, 802 (1998)].
38. J. S. Mathis, W. Rumpl, and K. H. Nordsick, Astrophys. J. **217**, 425 (1977).
39. A. Li and J. M. Greenberg, Astron. Astrophys. **331**, 291 (1998).
40. V. P. Grinin, E. A. Kolotilov, and A. H. Rostopchina, Astron. Astrophys., Suppl. Ser. **112**, 457 (1995).
41. A. N. Rostopchina, V. P. Grinin, A. Okazaki, *et al.*, Astron. Astrophys. **327**, 145 (1997).
42. C. Leinert, A. Richichi, and M. Haas, Astron. Astrophys. **318**, 472 (1997).
43. P. Artymovicz and S. H. Lubow, Astrophys. J. Lett. **467**, L77 (1996).
44. A. V. Krivova, Pis'ma Astron. Zh. **23**, 371 (1997).

Translated by K. Maslennikov

Astronomy Reports, Vol. 44, No. 6, 2000, pp. 376–388. Translated from Astronomicheskiĭ Zhurnal, Vol. 77, No. 6, 2000, pp. 432–446.
Original Russian Text Copyright © 2000 by Ivanova, Shimanskiĭ.

Non-LTE Analysis of the Formation of KI Lines in the Spectra of A–K Stars

D. V. Ivanova and V. V. Shimanskiĭ

Kazan State University, Kazan, Russia

Received March 3, 1999

Abstract—The non-LTE formation of KI lines in the spectra of A–K stars is analyzed. The computations are based on a 36-level model of the neutral potassium atom for blanketed LTE Kurucz model atmospheres with T_{eff} = 4000–10000 K, $\log g$ = 0.0–4.5, and [*M*/*H*] = (0.0)–(–2.0). The KI atoms in the atmospheres of these stars are in states of moderate and strong "over-recombination." A number of atomic parameters are refined using the profiles and equivalent widths of five lines in the solar spectrum. The classical van der Waals damping constants must be increased by factors of 2–60 to fit the observed profiles. The non-LTE solar potassium abundance—$\log\epsilon$ (K) = 5.14—corresponds to the meteoritic abundance. Non-LTE corrections to the potassium abundance are important and equal to –0.4…–0.7 dex for the λ7699 Å line and –0.15…–0.3 dex for the λλ12522, 12432, and 11769 Å lines. © *2000 MAIK "Nauka/Interperiodica".*

1. INTRODUCTION

There have been few studies of potassium lines in stellar spectra in the framework of chemical composition analyses. The main hindrance to such studies has been the absence of measurable and unblended potassium lines in the blue and ultraviolet. The λ7699 Å component of the 4*s*–4*p* resonance doublet is virtually the only KI line available for such analyses. This spectral region provides little information about stellar chemical composition, since it contains few lines and is strongly blended by telluric lines. Therefore, this wavelength interval was almost completely neglected until the early 1990s. Only the introduction of modern digital techniques for spectral recording have made it possible to take into account and exclude telluric lines.

At present, there has been only one fairly extensive series of KI-line observations, carried out by Gratton and Sneden for 25 mainly solar-type stars [1]. Even for stars with parameters close to those of the Sun, the abundances inferred in [1] were 0.2–0.4 dex higher than predicted by the standard theory of Galactic chemical evolution [2]. The potassium overabundance increases steadily in the transition to low-metallicity stars with [Fe/H] = –2, becoming as high as 0.7 dex instead of decreasing to [K/Fe] = –0.4 dex, as predicted by the theory [2]. Gratton and Sneden [3] suggested two possible explanations for this behavior: strong blending of potassium lines by telluric lines and possible non-LTE effects. The second possibility seems quite logical given that analyses of the resonance lines of NaI [4], which has a similar atomic structure, revealed substantial departures from LTE.

Since the pioneering work of de la Reza and Muller [8], non-LTE effects for KI have been analyzed by a number of other authors, including Severino *et al.* [5], Shchukina [6], and McKenna [7]. However, most of these papers focused on the formation of the λ7699 Å line in the solar atmosphere and its possible use for determining the velocity field at the solar surface. In their comprehensive analysis of non-LTE effects for populated KI levels, Bruls *et al.* [9] showed that a state of "over-recombination"—overpopulation of the ground state—was typical of the various solar models considered. As a result, the λ7699 Å line is stronger compared to the LTE case, and its intensity depends weakly on the adopted model atmosphere. Takeda *et al.* [10] performed non-LTE calculations of the profiles of this line using one-dimensional Kurucz model atmospheres [11]. Their main conclusion was that the classical Unsöld C_6 constants for van der Waals broadening had to be increased by up to an order of magnitude. They [10] showed the non-LTE atmospheric potassium abundances of the Sun and Procyon to be $\log\epsilon$ (K) = 5.1—0.4–0.7 dex lower than the corresponding LTE abundances, approximately corresponding to the meteoritic abundance [12]. In a later study, Takeda *et al.* [13] found the potassium abundance of the Cepheid SU Cas to be 0.2 dex higher than the corresponding solar abundance.

Thus, earlier investigations of KI lines have demonstrated that (1) there are substantial discrepancies between the derived LTE potassium abundances and theoretical predictions based on the synthesis of potassium during stellar evolution, and (2) the structure of potassium energy levels is favorable for strong departures from LTE, which, if correctly included in the analysis, might resolve these discrepancies. It should be borne in mind, however, that potassium belongs to a group of five elements (Cl, Ar, K, Ca, and Sc), of which only calcium has been studied reasonably thoroughly from the point of view of abundance determinations in

1063-7729/00/4406-0376$20.00 © 2000 MAIK "Nauka/Interperiodica"

late-type stars. Meanwhile, it is of interest to determine the mechanisms of elemental synthesis within the group, because it separates the light elements that form during the stage of hydrostatic carbon and oxygen core burning from the iron-group elements, whose abundances are determined to some extent by both αcapture and explosive nucleosynthesis. Thus, the atmospheric abundances of potassium, and also of calcium, can serve as a second indicator of the type of nuclear reactions occurring during late stages of stellar evolution. Determining accurate non-LTE corrections would make it possible to derive elemental abundances taking possible non-LTE effects into account, thereby avoiding misinterpretation of the results. This paper is dedicated to an analysis of non-LTE effects in the spectra of stars of various spectral types, luminosities, and metallicities.

Section 2 describes the atomic model adopted for KI, the atomic data for the lines considered, and the computation technique. In Section 3, we analyze KI lines in the solar spectrum using the data from the spectral atlas [14]. The analysis refines some poorly determined data for the atom as whole and the observed lines and investigates various abundance uncertainties due to the use of different model atmospheres and to errors in the van der Waals broadening constant C_6, microturbulent velocity $V_{\rm turb}$, and equivalent widths W_λ. Section 4 presents our computed non-LTE corrections for the potassium abundances for various domains of model-atmosphere parameters.

2. COMPUTATION TECHNIQUE

We computed non-LTE level populations and line equivalent widths using the NONLTE3 code developed by Sakhibullin [15] implementing the complete linearization method of Auer and Heasley [16]. The absorption coefficients at all frequencies were computed taking into account all continuum opacity sources, about 170 000 of the strongest lines at wavelengths $\lambda > 912$ Å from the list of Kurucz [17], and the main molecular bands according to the data of Nersisyan *et al.* [18].

We obtained most of our results using blanketed Kurucz-1994 model atmospheres [17] (hereafter newKur). For a number of stars, we performed additional computations to compare the results with those obtained using Kurucz-1979 model atmospheres [11] (oldKur) and, in the case of the Sun, with results based on the model atmospheres of Holweger and Muller [19] (HolMu) and Bell *et al.* [20] (Bell). We also performed computations for a combined solar model comprised of the newKur and Val-C [21] model atmospheres joined at the region of the temperature minimum.

We used the 36-level atomic model for KI whose Grotrian diagram is shown in Fig. 1. This model includes 35 bound states of KI and the $1s^22s^22p^63s^23p^61S_0$ ground state of KII. The model includes all levels with $n \le 10$ and $l \le 3$, and also the 11*s*, 12*s*, 5*g*, 6*g*, and 6*h* levels. We included the fine-structure splitting of the 4*p* level, since a number of studies [4, 9, 22] have indicated this to be important for non-LTE computations.

We took the ground-state ionization energy from [23] and calculated the excitation energies for other levels from the laboratory wavelengths listed in [24]. The 10*f* level has the lowest ionization energy in the model considered (0.11 eV). It follows that our atomic model for KI can be used for stars with temperatures T_{eff} = 2000–15 000 K, i.e., throughout the temperature range for observable potassium lines.

We compiled data from several sources [17, 25–27] to obtain a set of oscillator strengths for the bound–bound transitions. For principal lines, the discrepancies between published oscillator strengths were within 5%. The oscillator strength discrepancies increase for other lines, reaching 10 and 25% for transitions between lower and higher levels, respectively. Such errors for individual lines can be neglected in non-LTE computations, since they change the resulting level populations by only hundredths of a percent. Therefore, we took into account the maximum number of transitions possible with the data available. As a result, our computations include a total of 202 bound–bound transitions, of which 45 were taken to be linearizable.

To compute the ionization cross sections for levels with $n \le 10$ and $l \le 3$, we used the data tabulated in [28] fitted by the formula

$$\sigma_\nu = \left(\alpha + \frac{E_{\rm ion}}{\Delta E_\nu}\right)^2 \sigma_0 \nu^S, \qquad (1)$$

where $E_{\rm ion} = h\nu_{\rm ion}$ is the threshold ionization energy for the given level; $\Delta E_\nu = h\nu$, the transition energy at a given frequency; and σ_0, α, and S are approximation parameters. We computed the ground-state ionization cross section using a six-parameter approximation [29] to the results obtained using the Hartree–Dirac–Slater method. Note that the ionization cross sections reported in [28] and [29] differ by less than 10%. For the 11*s*, 12*s*, 5*g*, 6*g*, and 6*h* levels, which lack theoretical data, we used the ionization cross sections for the closest *s* or *f* states.

We used several methods to compute the electron collision rates:

(1) Regermorter's [30] approximation formula, with a floating value for the factor γ for the allowed transitions;

(2) Park's [23] two-parameter relations for most allowed and forbidden transitions with $n \le 6$;

(3) the tables of [31] for a number of transitions between high levels;

(4) the approximation formula of Casor and Nussbaumer [32] with $\Omega = 1.0$ for several transitions with no other data available;

(5) the four-parameter approximation of [31] to compute shock ionization by electrons from the $4s^2S$ ground state and Lotz's [33] approximation to compute ionization from the excited levels.

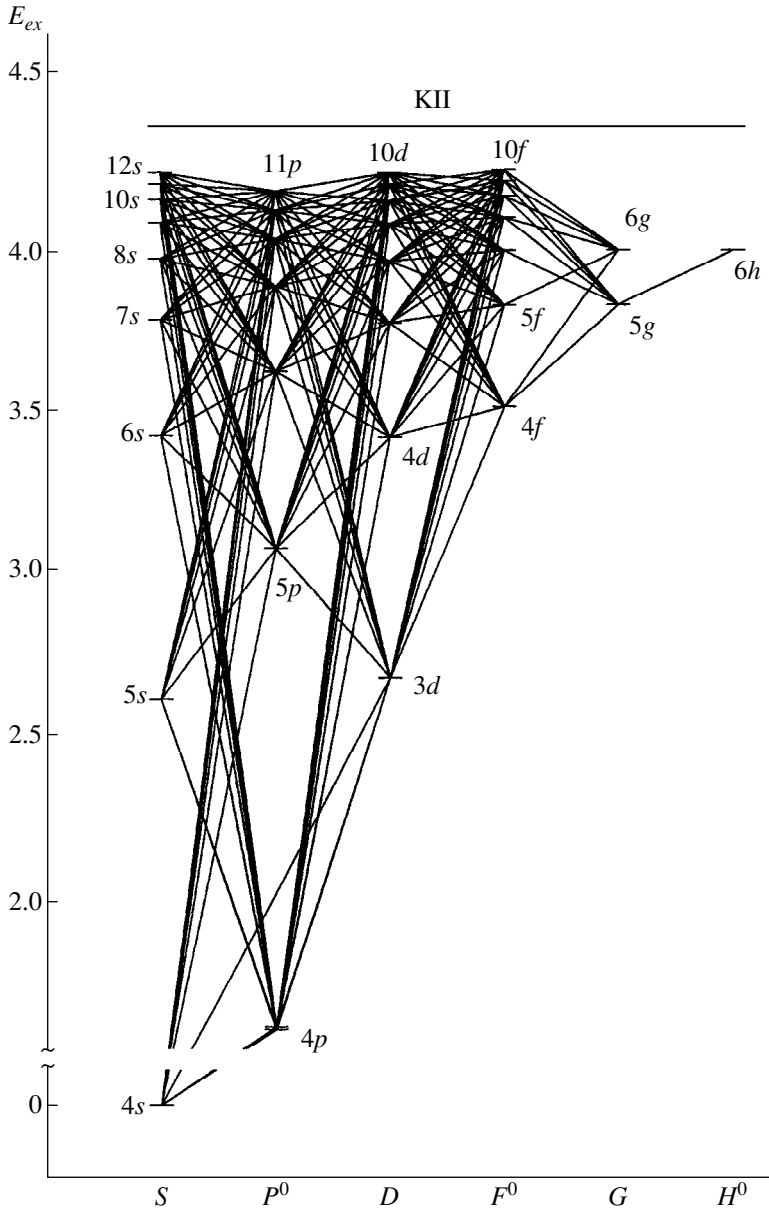

Fig. 1. Model KI atom.

For allowed transitions, we took into account collisional excitation and ionization by collisions with hydrogen atoms using the formula of Drawin [34]. A number of earlier studies [10, 34] have shown this to be only an order-of-magnitude formula, and we therefore used it with a scaling factor $k_H = 0$–1.

In the case of the newKur solar model atmosphere, we compared the results obtained using Regemorter's [30] and Park's [23] formulas for the collisional rates for the principal transitions. The two resonance-line abundances derived with $k_H = 0$ differed by 0.04 dex. The abundances derived from all other lines at $k_H = 0.0$ and from all lines at $k_H > 0.1$ differ by less than 0.02 dex. Since these discrepancies were so small, we used Park's [23] data to obtain all other results for transitions between levels with $n \le 6$.

We computed the profiles of five observable lines in the wavelength interval $4000 \le \lambda \le 13000$ Å. Table 1 lists the corresponding oscillator strengths and line broadening parameters. The theoretical profiles and equivalent widths include the effect of Doppler broadening due to thermal motions and microturbulence, radiation damping (with constants derived from the lifetimes given in [9]), and van der Waals broadening, computed using the formula of Gray with Unsöld's [36] C_6 constants. We will refer to these constants as C_6(Uns) to distinguish them from the empirical constants C_6(prof) we estimated using the observed solar spectrum. The technique we

Table 1. Unsöld transition configurations, f_{ij}, γ_R, and C_6

λ, Å	Transition	f_{ij}	γ_R, 10^{-7}	C_6, 10^{30}
6938.78	$4p^2P^0_{3/2}$–$6s$	0.019	4.802	0.536
7698.97	$4s$ –$4p^2P^0_{1/2}$	0.339	3.663	0.0964
11769.63	$4p^2P^0_{3/2}$–$3d$	0.090	6.067	0.192
12432.23	$4p^2P^0_{1/2}$–$5s$	0.183	5.818	0.445
12522.10	$4p^2P^0_{3/2}$–$5s$	0.183	5.818	0.444

used to determine C_6(prof) is described in Section 3. As shown in [9], Stark broadening is insignificant, and we neglected it in this study. Our analysis of the solar line profiles included additional broadening due to rotation $V\sin(i)$ = 1.9 km/s, microturbulence $V_{\rm macr}$ = 1.5 km/s, and a Gaussian instrumental profile with a half-width corresponding to the spectral resolution of [14].

We adopted the initial solar potassium abundance ($\log\epsilon$(K) = 5.14) from [12], which corresponds to the meteoritic abundance. When computing the line profiles for stars of nonsolar metallicity, we varied the potassium abundance in proportion to the overall metallicity.

3. ANALYSIS OF POTASSIUM LINES IN THE SOLAR SPECTRUM

We used Kurucz's atlas [14] (Δλ2960–13000 Å, signal-to-noise ratio 9000, and λ/Δλ = 522000) as the source of the solar spectrum. We used several methods to determine equivalent widths (direct integration of the profile and half-profile, fitting a Gaussian or Lorentz curve, convolving several Gaussians and Lorentz curves to compute the areas of individual components). Table 2 lists the final equivalent widths we obtained after analyzing the results given by the various methods (see below). A comparison of the observed and theoretical solar infrared spectra revealed additional continuum absorption due to extended (Δλ > 10 Å) molecular bands in the earth's atmosphere at the wavelengths for most of the KI lines studied. Since our technique does not take this absorption into account, we determined the continuum level by dividing all the intensities by the Δ values listed in Table 2. These values correspond to the maximum residual intensities near the lines studied. The refined continuum level had a nonzero slope at λλ12522, 12432 Å, and we give the mean values corresponding to the line centers in these cases. Note that the equivalent widths of the infrared subordinate lines derived for the refined continuum calculation agree with the results of Lambert and Luck [36] to within 5%.

Unfortunately, the set of lines studied here is by no means representative of the adopted model atom for KI. This set includes the λ7699 Å resonance line, three subordinate lines λλ12522, 12432, 11769 Å resulting from transitions from the 4*p* level to the nearest 5*s* and 3*d* levels, and the weak λ6938 Å line resulting from transitions from the 4*p* level to the highly excited 6*s* level. A non-LTE analysis of the potassium lines in the solar spectrum should bring the resonance-line abundance into agreement with the mean abundance derived from all the subordinate lines. This gives us a criterion for assessing the accuracy of the computed non-LTE 4*s*-to-4*p* level population ratios and non-LTE departures for the λ7699 Å line.

Figure 2 shows the distributions of the *b* factors ($b = n_{\rm NLTE}/n_{\rm LTE}$) for the principal KI levels for the newKur, oldKur, and HolMu solar model atmospheres with k_H = 1.0, and also for the newKur model atmosphere with k_H = 0.0. Our analysis of these profiles indicates that the KI atoms in the solar atmosphere are in a state of strong over-recombination; i.e., the lower 4*s* level is overpopulated relative to the main KII ionization stage in layers with $\tau_R < 0.4$. The KI over-recombination state is possible owing to the following two factors:

(1) The 4*s* ground level has a very small ionization cross section (σ_0 = 0.012 Mb), which very strongly restricts ionization of the atoms by ultraviolet radiation. For comparison, MgI atoms, which are in a state of weak "over-ionization" in the solar atmosphere, and NaI atoms, which are in a state of moderate over-recombination, have cross sections of σ_0 = 2.93 and 0.142 Mb, respectively. Ionization of the 4*p* level is also

Table 2. Empirical values for C_6 (prof); equivalent widths and abundances derived from various lines with and without continuum level correction (superscripts 2 and 1, respectively); continuum correction factor Δ; mean $\log\epsilon$(K) derived from all lines (superscript 3) except λ6938Å (superscript 4) and their rms errors σ

λ, Å	C_6^1, 10^{30}	W_λ^1, mÅ	$\log\epsilon(\mathrm{K})^1$	C_6^2, 10^{30}	W_λ^2, mÅ	$\log\epsilon(\mathrm{K})^2$	Δ
6938	55	6.0	5.13	10	4.1	4.98	0.995
7699	0.2	170	5.06	0.2	170	5.06	1.000
11769	49	58	5.23	13	48	5.18	0.993
12432	35	76	5.26	15	55	5.17	0.985
12522	20	99	5.21	11	83	5.14	0.980
$\log\epsilon(\mathrm{K})^3 \pm \sigma$	5.18 ± 0.07			5.11 ± 0.08			
$\log\epsilon(\mathrm{K})^4 \pm \sigma$	5.19 ± 0.08			5.14 ± 0.05			

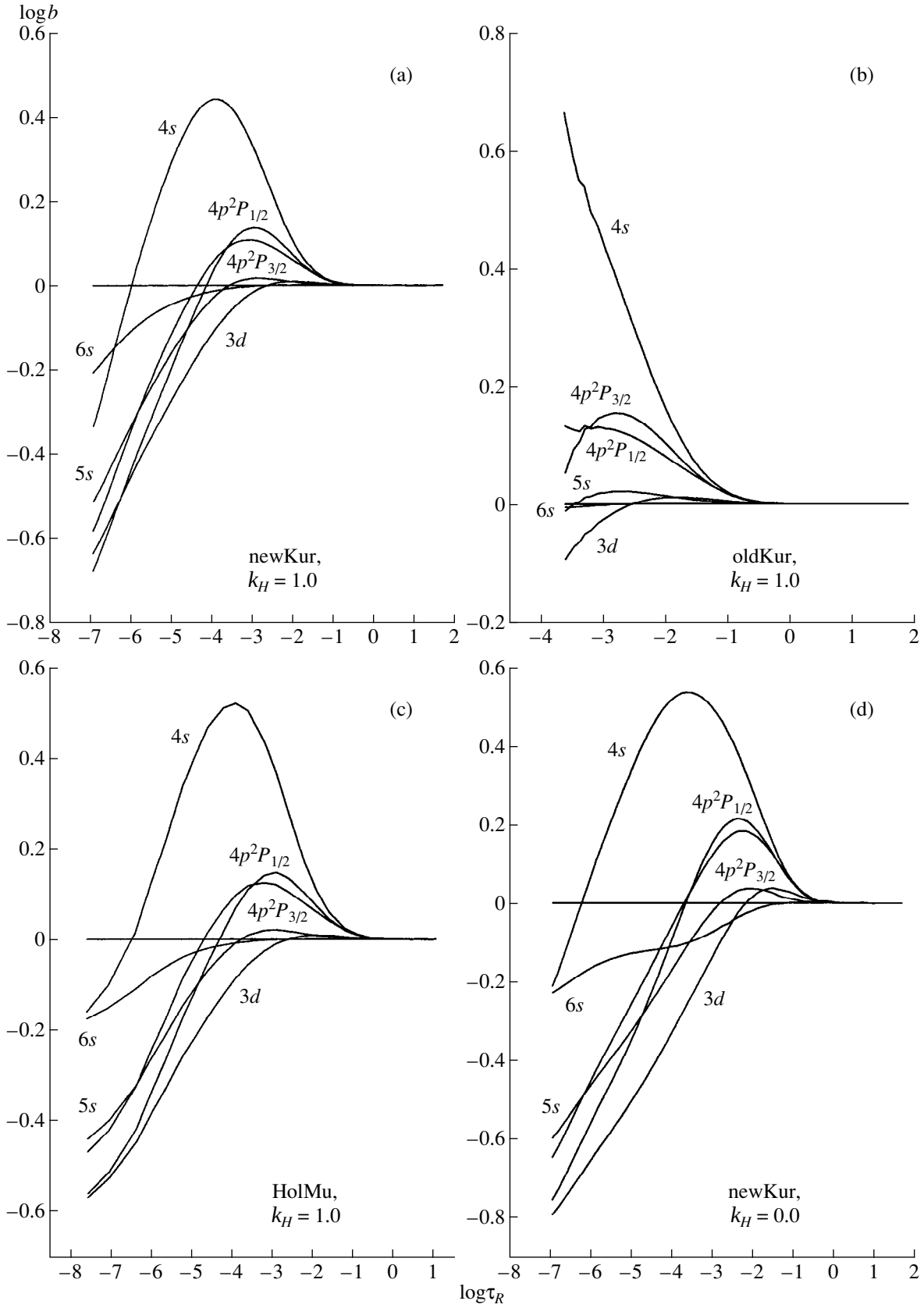

Fig. 2. *b* factors of the main KI levels plotted as functions of the Rosseland opacity τ_R for the (a) newKur, (b) oldKur, (c) HolMu model atmospheres with $k_H = 1.0$ and for the (d) newKur model atmosphere with $k_H = 0.0$.

inefficient, since the corresponding ionization threshold lies in the visible part of the spectrum (λ4530 Å). Thus, photoionization of KI atoms only very slightly affects the overall KI/KII ionization balance.

(2) All other KI lines lie in the infrared part of the spectrum, which is characterized by a strong excess of rates of spontaneous transitions over rates of photoexcitation. This is most pronounced in the lines corresponding to the 4*p*–5*s*, 4*p*–3*d*, and, especially, 4*s*–4*p* transitions. The dominance of spontaneous transitions in KI lines provides a mechanism for the sequential, multistep pumping of atoms from higher to lower states. As a result, highly excited KI levels become strongly depopulated, allowing their efficient collisional population from the KII ionization continuum, which is always in LTE. Together, these mechanisms ensure the efficient redistribution of atoms from the KII ground ionization stage to the 4*p* and 4*s* levels.

The magnitudes of departures from LTE for various model atmospheres are determined by their temperature gradients $dT_e/d\tau_R$ (where τ_R is the Rosseland opacity), which depend on the J_ν/S_ν ratios in layers with $\tau_\nu < 1.0$. The Bell and oldKur model atmospheres have the lowest temperature gradients, so that their atoms are least ionized by ultraviolet radiation. These model atmospheres exhibit the strongest departures from LTE in the form of over-recombination, which increase monotonically with height. The newKur and HolMu models have higher gradients $dT_e/d\tau_R$ and J_ν/S_ν ratios in layers with $\tau_\nu < 1.0$, higher ionization efficiencies, and lower efficiencies for spontaneous transitions. Therefore, the resulting *b* factors for the 4*s* level are lower ($\log b_{4s} = 0.5$) and decrease rapidly in higher layers.

Departures from LTE for the excited 4*p* level are similar to those for the 4*s* level, which is overpopulated only in layers where the 4*s*–4*p* resonance transition ($-3.2 < \log\tau_R < -0.6$). Lines are in detailed balance. The magnitude of non-LTE effects is then a factor of two to three smaller than for the 4*s* level, due to the lower efficiency of the 5*s*–4*p* and 3*d*–4*p* spontaneous transitions. Higher levels ($\log\tau_R < -3.2$) do not satisfy the detailed balance conditions for the resonance lines, and the 4*p* level is rapidly depopulated due to spontaneous transitions to the 4*s* ground state. As is evident from a comparison of Figs. 2a and 2b, changes in the neutral hydrogen collision rates do not affect the overall pattern of departures from LTE. Increasing k_H from 0.0 to 1.0 decreases the maximum *b* factors for the 4*s* and 4*p* levels decrease by a factor of 1.2–1.3 and shifts them toward higher levels ($\Delta\log\tau_R \approx -0.4$). The underpopulation of all highly excited levels decreases, reducing the gap between the *b* factors for the upper and lower levels for all transitions.

When determining the non-LTE abundances from the KI line profiles, we simultaneously refined the

(1) coefficient k_H in the formula for collisional interactions with hydrogen atoms;

(2) broadening constants C_6(prof);

(3) microturbulence ($V_{\rm turb}$) and macroturbulence ($V_{\rm macr}$) velocities.

This list includes neither the damping constants γ_R nor the rotational velocity, since the possible errors in these parameters (less than 10%) are insignificant and cannot affect the results. Neither did we refine the Stark-broadening constants, since the Stark effect is negligible under solar conditions [9]. We refined the parameters above using the *newKur* model atmosphere by finding the optimal agreement between the observed and theoretical profiles, taking into account the following factors:

(1) Changes in the KI abundance only slightly affect the residual core intensities of the λ7699 Å line, with the effect being stronger in the wings of this line and in the cores and wings of other lines.

(2) Increasing k_H decreases the core optical depth, most conspicuously in the case of the λ7699 Å resonance line.

(3) The microturbulence velocity $V_{\rm turb}$ broadens the cores of all lines and decreases the core depths of subordinate lines.

(4) The macroturbulence velocity broadens all lines in the core-to-wing transition zone, decreasing the $dH_\lambda/d\lambda$ gradient and increasing the residual core intensity.

(5) Increasing the constants C_6 increases the residual core intensities of subordinate lines and enhances the wings of all lines.

No single potassium abundance provides full agreement for all KI lines. This could be due to errors in the adopted model atmosphere and oscillator strengths. Therefore, we found the individual optimum abundances for each line, while also trying to minimize the abundance dispersion over the entire line set. Table 2 lists the resulting C_6(prof) constants for the spectral lines derived using the unrefined and refined continuum, and Fig. 3 shows the best-fit profiles for the latter case.

The λ7699 Å line yielded KI abundances that were systematically lower than those for all the subordinate lines at all $k_H \le 1.0$. As a result, the abundances can be brought into the best overall agreement if $k_H = 1.0$, since, in this case, the residual core intensities of the λ7699 Å line are at a maximum and the discrepancy between the results for the main line and the subordinate lines is at a minimum.

We were not able to unambiguously determine the microturbulence velocity, which varies in the interval $V_{\rm turb} = 1.0$–1.4 km/s, and we will fix it to be $V_{\rm turb} = 1.2$ km/s. A macroturbulence velocity of $V_{\rm macr} = 2.0$ km/s provides better agreement between the observed and theoretical λ7699 Å line profiles than $V_{\rm macr} = 0.0$ km/s, but the best agreement in the former case implies a KI abundance that is 0.25 dex lower than the mean value averaged over the other lines. Therefore, we give only an upper bound for the macroturbulence velocity, $V_{\rm macr} = 1.5$ km/s.

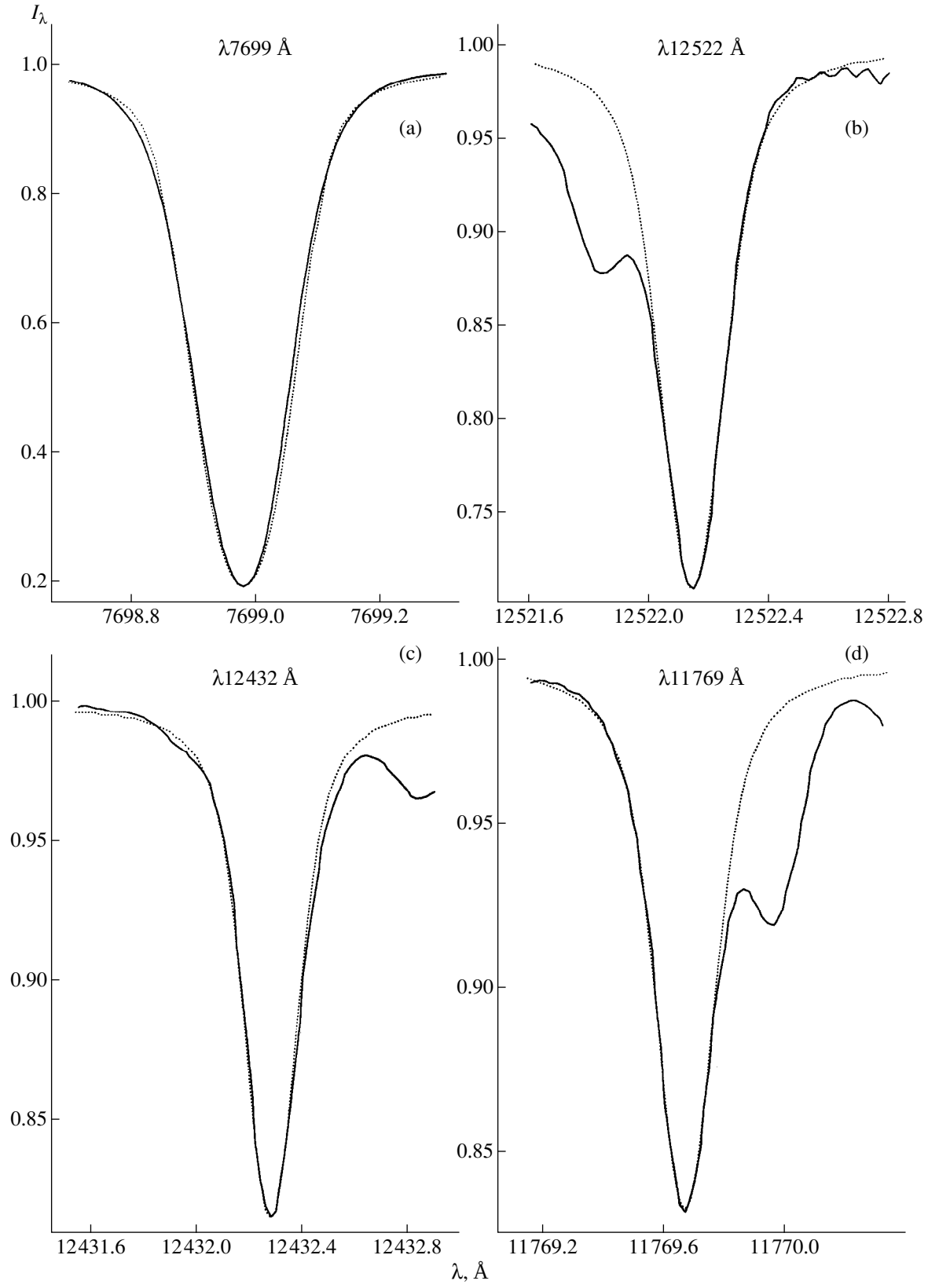

Fig. 3. Observed (solid) and theoretical (dashed) profiles of the (a) λλ7699 Å, (b) 12522 Å, (c) 12 432 Å, and (d) 11769 Å lines in the solar spectrum.

Our estimates of the C_6(prof) broadening constants substantially exceed the Unsöld values, by factors of two and 20–60 for the λ7699 Å line and the other lines, respectively. Note that our refinement of the continuum level made it possible to appreciably decrease the C_6(prof) values for the subordinate lines (by up to a factor of five). Thus, the reliability of the adopted continuum level is a crucial factor in the KI-line analysis.

The λ7699 Å line is obviously asymmetric. To investigate this, we computed the profile of this line taking into account the hyperfine splitting and isotopic shifts in accordance with [27]. However, this failed to improve the results significantly. The asymmetry could be due to motions in the solar atmosphere or to weak telluric lines.

The abundance derived using the λ6938 Å line and the refined continuum differs substantially from the mean abundance. We had to exclude this line when determining the final mean abundance, due to its low intensity in the solar spectrum (W_λ = 4.1 mÅ), which made the line profile very sensitive to the adopted continuum level. The resulting abundance, $\log\epsilon$ (K) = 5.14, coincides with the meteoritic abundance, and its dispersion (σ = 0.05 dex) is within current standards for the accuracy of abundance determinations.

At present, the potassium abundances in stellar atmospheres are derived using equivalent widths alone. Therefore, to determine the influence of various parameters on the results obtained by using equivalent widths W_λ, we computed LTE and non-LTE abundances for various model atmospheres, broadening constants C_6(prof), microturbulence velocities $V_{\rm turb}$, and k_H values. The results, some of which are listed in Table 3, lead us to the following general conclusions.

(1) Non-LTE corrections are small (ΔX = –0.03…–0.05) for the λ6938 Å line, important (ΔX = –0.05…–0.09) for the λλ12522, 12432, and 11769 Å lines, and very important (ΔX = –0.26…–0.39) for the λ7699 Å line.

(2) Increasing $V_{\rm turb}$ only slightly decreases the abundances derived from subordinate lines (ΔX = 0.000–0.004 for $\Delta V_{\rm turb}$ = 0.2 km s^{-1}) and has a stronger effect on the λ7699 Å line (ΔX = 0.020–0.045).

(3) Decreasing the coefficient k_H from 1.0 to 0.0 smoothly decreases the mean abundance by 0.13 dex. The dispersion of the abundances for different lines varies only slightly.

(4) Compared to the benchmark newKur model atmosphere, oldKur decreases the abundance by 0.05 dex and HolMu increases it by 0.05 dex. The dispersion of the abundance estimates is about 0.06 dex for all model atmospheres considered.

(5) Using the second set of equivalent widths decreases the mean abundance and its dispersion by 0.09 and 0.04 dex, respectively.

(6) The abundances derived from equivalent widths are somewhat lower than those yielded by profile fitting (by 0.12 and 0.05 dex for individual lines and the mean abundance, respectively).

Table 3. Mean LTE and non-LTE corrections to $\overline{\Delta X}$ and their rms errors σ for various model atmospheres, k_H, and the two sets of empirical broadening constants, C_6^1 and C_6^2

$\overline{\Delta X} \pm \sigma$		
k_H = 1.0, C_6^2, non-LTE		
newKur	oldKur	HolMu
−0.08 ± 0.06	−0.13 ± 0.06	−0.03 ± 0.06
newKur, C_6^2, non-LTE		
k_H = 0.0	k_H = 0.1	k_H = 1.0
−0.21 ± 0.06	−0.17 ± 0.07	−0.08 ± 0.06
newKur, k_H = 1.0		
C_6^1, non-LTE	C_6^2, LTE	C_6^2, non-LTE
0.01 ± 0.10	0.01 ± 0.08	−0.08 ± 0.06

Note: Note that, in all cases, C_6^1 and C_6^2 are used in combination with the sets of equivalent widths W_λ^1 and W_λ^2, respectively.

Thus, the potassium abundances derived for other stars based on measurements of λ7699Å-line equivalent widths alone can have the following errors:

—about 0.06 dex due to errors in the adopted model atmospheres and $V_{\rm turb}$;

—about 0.08 dex due to errors in C_6 and k_H;

—about 0.08 dex due to errors in the measured equivalent widths W_λ.

The total error including all these factors is 0.13 dex. Since the possible magnitude of non-LTE corrections for the λ7699 Å line exceed this estimate by more than a factor of two, allowing for departures from LTE is of prime importance in potassium abundance determinations.

4. DEPARTURES FROM LTE FOR KI IN THE ATMOSPHERES OF STARS OF VARIOUS SPECTRAL TYPES

We used Kurucz's [17] model-atmosphere grid to compute possible departures from LTE for KI lines in the spectra of stars of various spectral types. We varied the model parameters within the following intervals: T_{eff} = 4000–10000 K with step 250 K; $\log g$ = 0–4.5 with step 0.5, and [*M*/*H*] = 0 to –2 with step 0.5. Figure 4 shows the distribution of the *b* factors for the ground atomic levels for model atmospheres differing in one of the above parameters. Our analysis of these profiles leads us to the following conclusions:

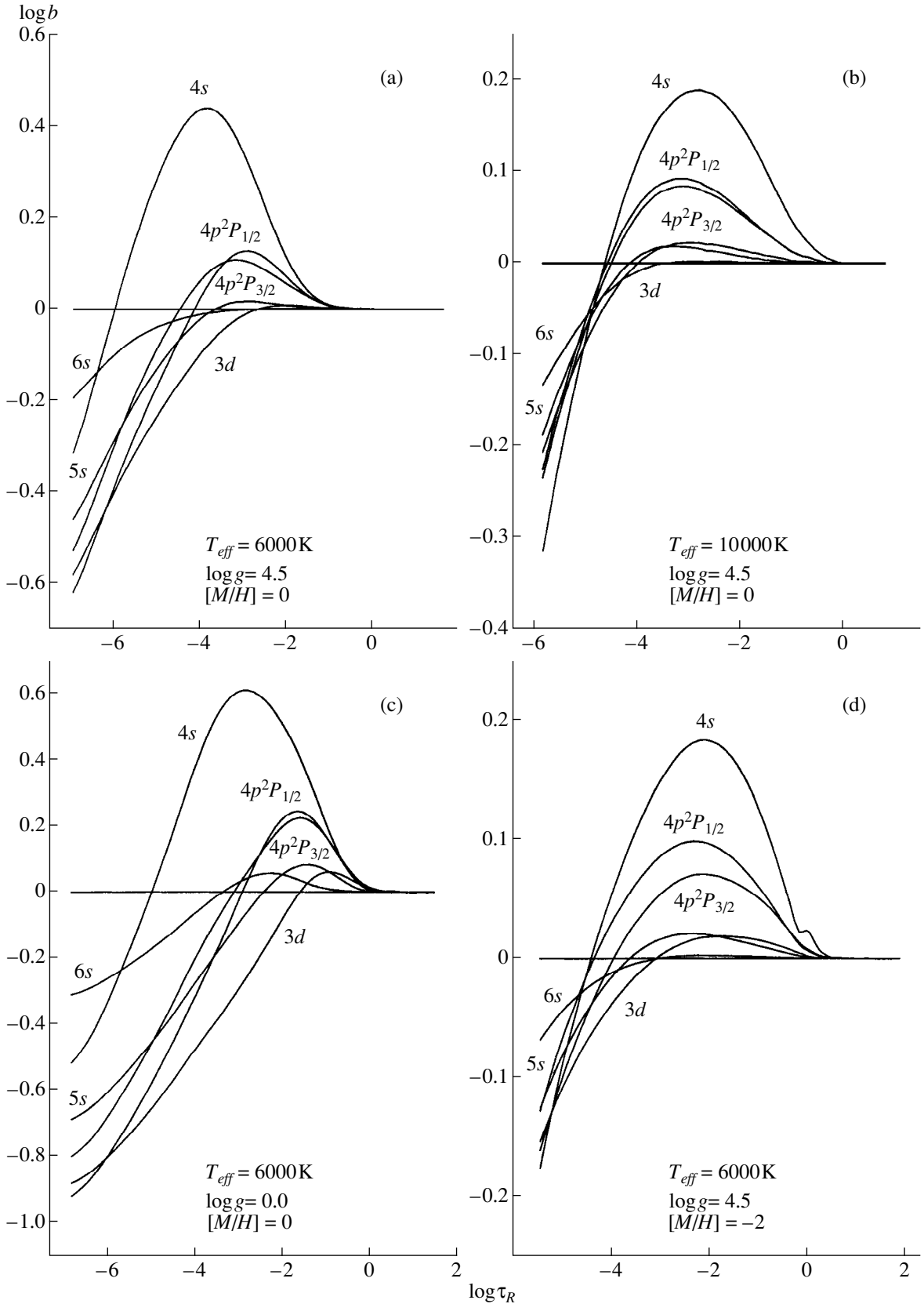

Fig. 4. *b* factors of the main KI levels plotted as functions of the Rosseland opacity τ_R for the newKur model atmospheres for $k_H = 1.0$.

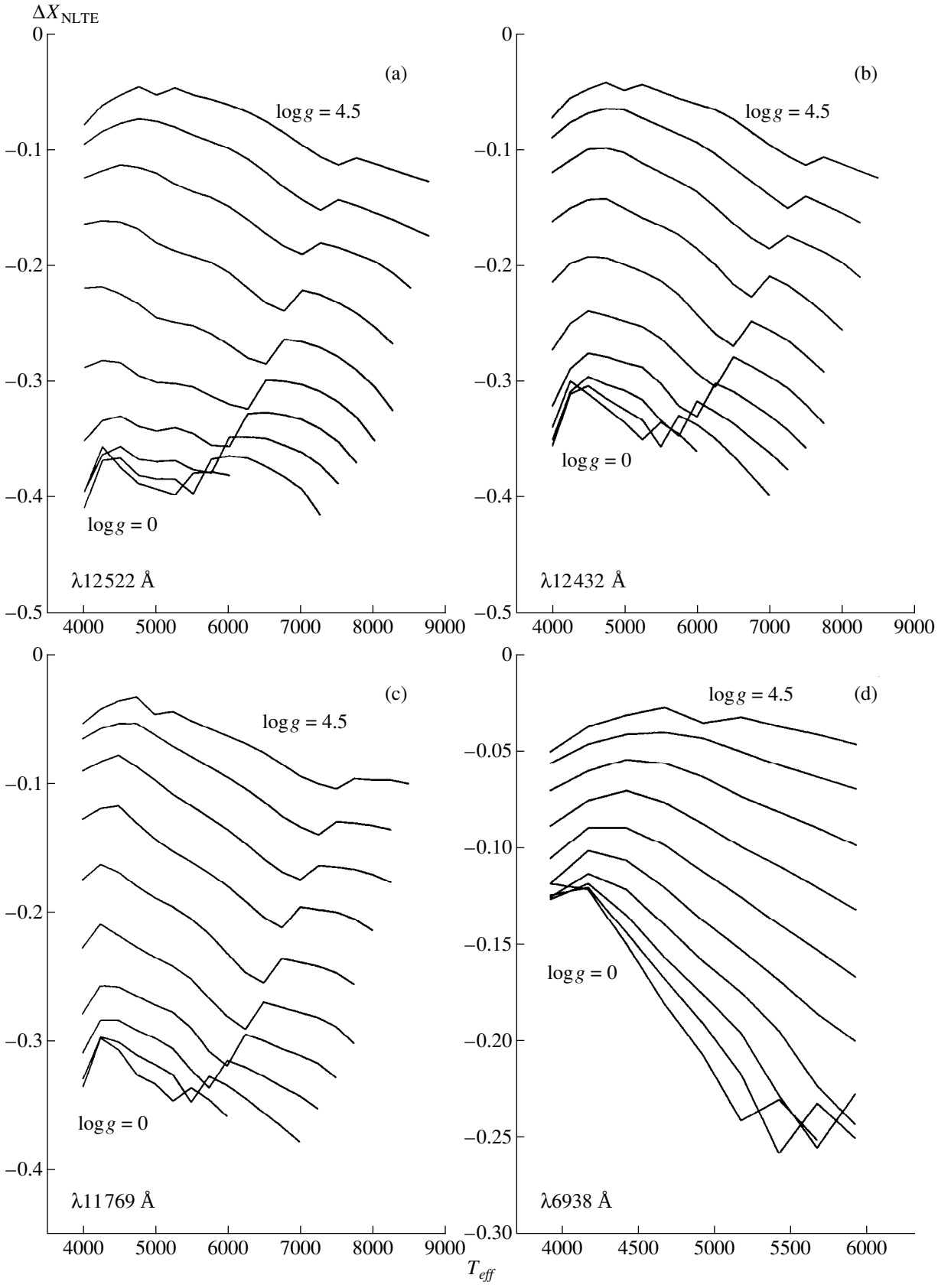

Fig. 5. Non-LTE corrections ΔX_{NLTE} to the abundances derived from the (a) λλ12522 Å, (b) 12432 Å, (c) 11769 Å, and (d) 6938 Å lines for solar-metallicity stars.

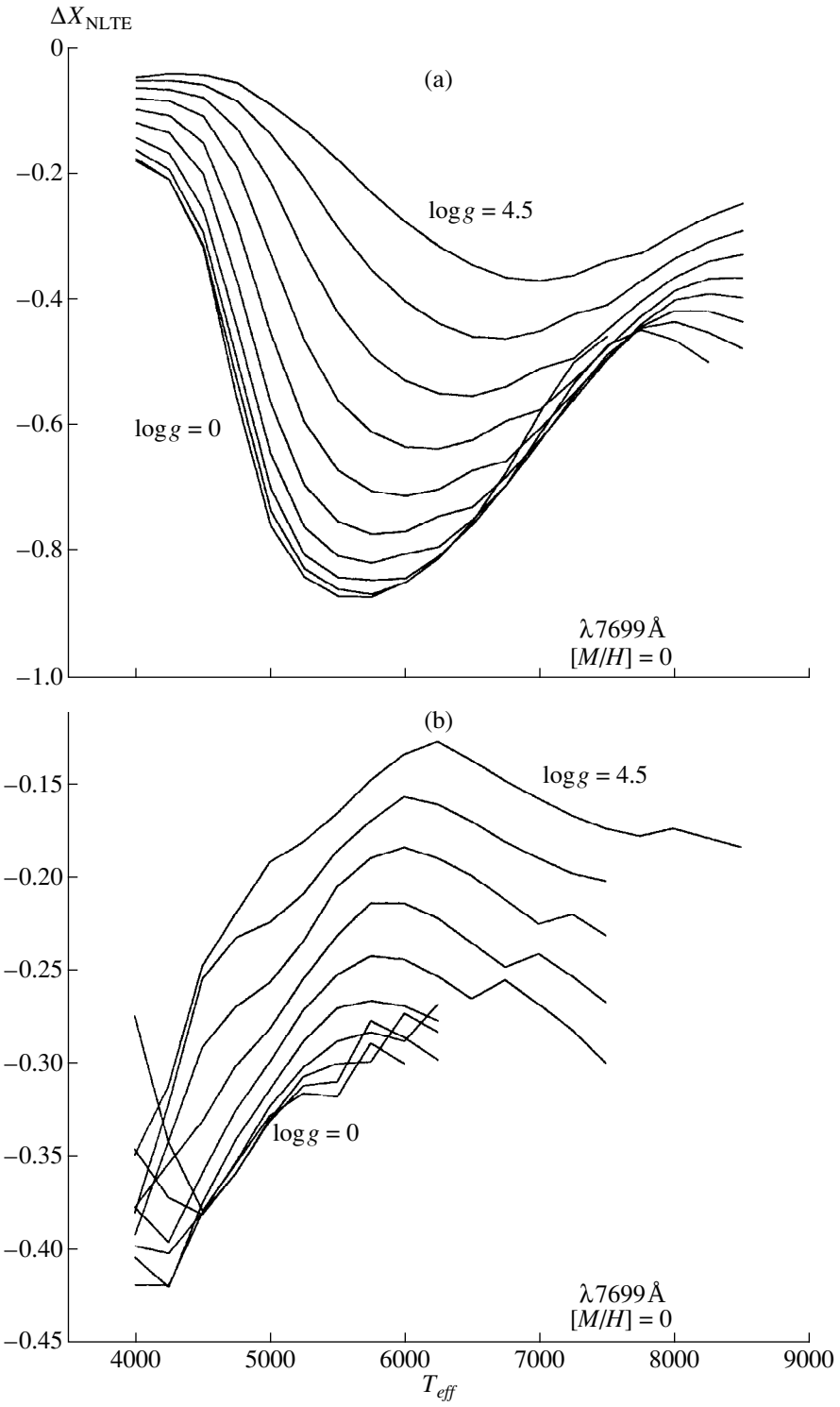

Fig. 6. Non-LTE corrections ΔX_{NLTE} to the abundances derived from the λ7699 Å lines for stars with metallicities (a) [M/H] = 0 and (b) [M/H] = –2.

(1) The over-recombination of the 4*s* ground state is stable throughout the range of effective temperatures, luminosities, and metallicities. The 4*p* level is also overpopulated but by a factor of 1.5–2 less than the ground level.

(2) The degree of over-recombination increases with effective temperature, up to $\log b_{4s} = 0.5$ at $T_{eff} = 6000$–7000 K, and then decreases to $\log b_{4s} = 0.2$. This over-recombination increase is a direct result of the increase in the cascade transition efficiency, since the source

function grows at the frequencies of most of the strong lines. The cascade transition efficiency decreases at temperatures above T_{eff} = 7000 K, since most of the KI lines become optically thin and have large residual core intensities. Note that the subordinate lines are the first to weaken, so that the overpopulation of the 4*p* level begins to decrease at lower temperatures (T_{eff} = 5500–6500 K).

(3) The departures from LTE level populations depend only slightly on $\log g$.

(4) Departures from LTE decrease with decreasing metallicity, due to the decrease of the intensities of all lines as described above.

Thus, the *b* factor of the 4*s* level always exceeds that of the 4*p* level, and the latter, in turn, exceeds those of all above-lying levels in stellar atmospheres for all spectral types. This pattern for the departures from LTE should always produce negative non-LTE corrections for all KI lines, as is evident from the expression for the non-LTE source function:

$$S_{ji} = \frac{2h\nu^3}{c^2}\frac{1}{\dfrac{n_i g_j}{n_j g_i} - 1} = \frac{2h\nu^3}{c^2}\frac{1}{\dfrac{b_i}{b_j}\exp\dfrac{h\nu}{kT} - 1} \approx \frac{b_j}{b_i}B_\nu(T), \quad (2)$$

where b_i and b_j are the *b* factors of the lower and upper levels, respectively. In our case, $b_i > b_j$, so that $S_{ji} < B_\nu(T)$, leading to line enhancement.

Figures 5 and 6 show the computed non-LTE corrections for various lines $\Delta X_{\rm NLTE} = X_{\rm NLTE} - X_{\rm LTE}$ (where $X_{\rm NLTE}$ and $X_{\rm LTE}$ are the non-LTE and LTE potassium abundances derived for the same line equivalent width) plotted as functions of T_{eff} for various $\log g$. Analysis of these relations for various lines reveals the following general patterns:

(1) The magnitude of the departure from LTE tends to increase with T_{eff}.

(2) The non-LTE corrections for a particular line depend on its position on the curve of growth (equivalent width):

(a) Departures from LTE are small on the damped portion of the curve of growth (Fig. 6a, T_{eff} = 4000–5000 K) but increase rapidly with decreasing line intensity.

(b) Non-LTE corrections reach their maximum on the saturated part of the curve of growth (Fig. 6b, T_{eff} = 5000–7000 K).

(c) Non-LTE corrections are minimum on the linear portion of the curve of growth, where they depend on the *b* factors of the lower levels for the corresponding transitions.

(3) The amplitude of $\Delta X_{\rm NLTE}(T_{eff})$ is 0.3–0.5 dex higher for high-luminosity stars than for dwarfs and is shifted toward lower T_{eff}.

As is evident from Fig. 6a, the non-LTE corrections for the λ7699 Å resonance line are important (up to –0.4 dex) for solar-luminosity dwarfs and become extremely large (up to –0.7 dex) for giants and supergiants. These corrections substantially exceed the possible errors noted in Section 3 and should be allowed for when determining potassium abundances. It is also desirable to take into account the $\Delta X_{\rm NLTE} \approx$ –0.15 to –0.30 dex corrections for the infrared λλ12522, 12432, and 11769 Å subordinate lines in the spectra of subgiant, giant, and supergiant stars. Finally, the λ6938 Å line usually requires no allowance for departures from LTE, buts its small equivalent width strongly restricts its use in abundance determinations.

The λ7699 Å line, which has rather large non-LTE corrections ($\Delta X_{\rm NLTE}$ = –0.15 to –0.25 dex), is the only one observable in the spectra of metal-deficient dwarfs. Departures from LTE for the λ7699 Å line proved to be important for stars of all spectral types considered. Furthermore, the non-LTE corrections can vary strongly as functions of the model atmosphere parameters, which can sometimes be a source of substantial errors, even when comparing the potassium abundances for stars of very similar types.

5. CONCLUSIONS

Our non-LTE analysis of the formation of KI lines in the atmospheres of stars of various types leads us to the following conclusions:

(1) The KI atoms in the atmospheres of stars of all spectral types are in a state of strong over-recombination; i.e., the 4*s* ground level and excited levels are overpopulated compared to LTE. This over-recombination is the result of strong cascade transitions in infrared KI lines.

(2) Taking into account departures from LTE increases the intensities of all KI lines; the increase is most pronounced for the λ7699 Å resonance line.

(3) Allowance for departures from LTE enables a more accurate description of the solar KI spectrum. Optimizing the agreement between the abundances derived from subordinate lines and from the resonance line suggests that k_H = 1.0 in the formula for the atomic hydrogen collision rates. The line profiles can be described best only if the classical Unsöld broadening constants C_6(Uns) are increased by factors from two to 60.

(4) The non-LTE corrections to the potassium abundances derived from the λ7699 Å line are important ($\Delta X_{\rm NLTE} \approx$ –0.4 to –0.7 dex) over a wide range of stellar temperatures (T_{eff} = 4000–10000 K), luminosities, and metallicities. Certain temperature intervals are characterized by a rapid increase of non-LTE corrections, which can lead to large errors in relative LTE abundances, even for stars with similar parameters. The non-LTE corrections for the λλ12522, 12432, and 11769 Å weak subordinate lines remain important ($\Delta X_{\rm NLTE} \approx$ –0.15 to –0.3 dex) and should be taken into account in chemical composition analyses based on infrared spectra.

ACKNOWLEDGMENTS

We are sincerely grateful to N.A. Sakhibullin and I.F. Bikmaev for their comprehensive assistance during this research, as well as their useful advice and numerous suggestions made during our analysis. This work was supported by the International Center for Fundamental Physics in Moscow, the "Soros Post-Graduate" and Student programs, and the Russian Foundation for Basic Research (project no. 96-02-16306a and 99-02-17488).

REFERENCES

1. R. G. Gratton and C. Sneden, Astron. Astrophys. **178**, 179 (1987).
2. F. X. Timmes, S. E. Woosley, and T. A. Weaver, Astrophys. J., Suppl. Ser. **98**, 617 (1995).
3. R. G. Gratton and C. Sneden, Astron. Astrophys., Suppl. Ser. **68**, 193 (1987).
4. L. I. Mashonkina, N. N. Shimanskaya, and V. V. Shimansky, Odessa Astron. Publ. **9**, 78 (1996).
5. G. Severino, G. Roberti, C. Marmolino, and M. T. Gómez, Solar Phys. **104**, 259 (1986).
6. N. G. Shchukina, Fiz. Kinematika Nebesnykh Tel **3**, 40 (1987).
7. S. J. McKenna, Astrophys. Space Sci. **106**, 283 (1984).
8. M. De la Reza and E. A. Muller, Solar Phys. **43**, 14 (1975).
9. J. H. Bruls, R. J. Rutten, and N. Shchukina, Astron. Astrophys. **265**, 237 (1992).
10. Y. Takeda, K. Kato, and Y. Watanabe, Publ. Astron. Soc. Jpn. **48**, 511 (1996).
11. R. L. Kurucz, Astrophys. J., Suppl. Ser. **40**, 1 (1979).
12. E. Anders and N. Grevesse, Geochim. Cosmochim. Acta **53**, 197 (1989).
13. Y. Takeda, S. Kawanomoto, and H. Ando, Publ. Astron. Soc. Jpn. **49**, 493 (1997).
14. R. L. Kurucz, I. Furenlid, J. Brault, and L. Testerman, in *Solar Flux Atlas from 296 to 1300 nm* (National Solar Observatory, Sunspot, New Mexico, 1984).
15. N. A. Sakhibullin, Tr. Kazan. Gor. Astron. Obs. **48**, 9 (1983).
16. L. H. Auer and J. Heasley, Astrophys. J. **205** (1971).
17. R. L. Kurucz, CD-ROMs (1994).
18. C. E. Nersisyan, A. V. Shavrina, and A. A. Yaremchuk, Astrofizika **30**, 247 (1989).
19. H. Holweger and E. Muller, Solar Phys. **39**, 19 (1974).
20. R. A. Bell, K. Eriksson, B. Gustafsson, and A. Nordlund, Astron. Astrophys., Suppl. Ser. **23**, 37 (1976).
21. P. Maltby, E. H. Avrett, M. Carlsson, *et al.*, Astrophys. J. **306**, 284 (1986).
22. D. V. Ivanova and V. V. Shimansky, Odessa Astron. Publ. **9**, 66 (1996).
23. S. Park, J. Quant. Spectrosc. Radiat. Transf. **11**, 7 (1971).
24. A. R Striganov and N. S. Sventitskiĭ, *Tables of Spectral Lines of Neutral and Ionized Atoms* (Atomizdat, Moscow, 1966; Plenum, New York, 1968).
25. E. Biemont and N. Grevesse, Atom. Data Nucl. Data Tables **12**, 217 (1973).
26. W. L. Wiese and M. W. Smith, in *Atomic Transition Probabilities. NSRDS–NBS Ref. Data Ser. 22* (Natl. Bur. Standarts, Washington, 1969), Vol. II.
27. A. A. Radtsig and B. M. Smirnov, in *Parameters of Atoms and Atomic Ions* (Énergoatomizdat, Moscow, 1986).
28. D. Hofsaess, Atom. Data Nucl. Data Tables **24**, 285 (1979).
29. D. G. Yakovlev, L. M. Band, M. B. Trzhaskovskaya, and D. A. Verner, Astron. Astrophys. **237**, 267 (1990).
30. H. van Regemorter, Astrophys. J. **132**, 906 (1962).
31. L. A. Vainshtein, I. I. Sobel'man, and E. A. Yukov, *Excitation of Atoms and Broadening of Spectral Lines* (Nauka, Moscow, 1979; Springer, Berlin, 1981).
32. J. I. Castor and H. Nussbaumer, Mon. Not. R. Astron. Soc. **155**, 293 (1972).
33. W. Lotz, Z. Phys. **232**, 101 (1970).
34. W. Steenbock and H. Holweger, Astron. Astrophys. **130**, 319 (1984).
35. A. Unsöld, in *Physik der Sternatmospheren* (Springer, Berlin, 1955).
36. D. L. Lambert and R. E. Luck, Mon. Not. R. Astron. Soc. **183**, 79 (1978).

Translated by A. Dambis

Astronomy Reports, Vol. 44, No. 6, 2000, pp. 389–400. Translated from Astronomicheskiĭ Zhurnal, Vol. 77, No. 6, 2000, pp. 447–459.
Original Russian Text Copyright © 2000 by Gal'per, Luchkov, Ozerov, Rinchinov, Khodarovich.

High-Energy Solar Gamma Rays in Solar Cycle 22: Data from the *Gamma-1* Experiment

A. M. Gal'per, B. I. Luchkov, Yu. V. Ozerov, S. B. Rinchinov, and A. M. Khodarovich

Moscow State Engineering Physics Institute, Kashirskoe sh. 31, Moscow, 115409 Russia

Received June 7, 1999

Abstract—We present an analysis of the temporal and spectral characteristics of high-energy ($E > 30$ MeV) gamma-ray emission from solar flares in the 22nd solar-activity cycle obtained in the *Gamma-1* experiment. The powerful flares of March 26, June 15, and October 27, 1991, are examined, as well as the weaker events of October 29 and December 8, 1991. Two emission phases are revealed in these flares: an active phase with individual, short bursts of radiation and a slow phase without such bursts. A qualitative scenario for the development of a solar gamma-ray flare is presented, based on the common temporal and spectral features of the observed flares and of simulation results. © *2000 MAIK "Nauka/Interperiodica".*

1. INTRODUCTION

The active phase of the Sun with its flares remains a very important target of observations for both ground-based and orbiting telescopes. Over the past 15 years, the Sun has also been investigated at gamma-ray energies, which carry the most direct information about the appearance and propagation in the solar atmosphere of beams of accelerated particles generated during solar flares.

Analyses of the hard X-ray and gamma-ray radiation of solar flares show that they are produced in processes that involve large releases of energy [1], substantially surpassing the thermal plasma energy. The thermal plasma energy is comparable only to the energy of the weakest flares [2]. On the other hand, the energy of the local magnetic fields in sites of sunspot clustering (in the active regions where flares occur) is quite sufficient to explain the energetics of the most powerful flares. In addition, magnetic energy-release processes occur impulsively; the field energy is rapidly converted to the kinetic energy of charged particles. This is consistent with the explosive character of the initial stage of a flare. The maximum kinetic energy of the particles in these processes is as high as several GeV. All this means that solar flares are high-energy phenomena, and the most direct information about them is supplied by hard gamma-ray radiation with energies of several tens of MeV.

The existing division of solar gamma-ray flares into impulsive and prolonged flares is based primarily on their duration. Nevertheless, analyses of the processes occurring during solar flares based on observations at radio, optical, and soft X-ray energies shows that, irrespective of their duration, we can distinguish in most flares an initial phase in which most of the acceleration of particles to relativistic energies is likely to occur. Moreover, a slow-decay component can be distinguished in the temporal profiles of many soft X-ray flares [3], during which there is additional energy pumping. Soft X-ray measurements carried out by the *Yohkoh* satellite since 1991 have also supplied a large amount of information that enables spatial imaging of solar-flare active regions with high time resolution [4]. However, this information is primarily related to secondary thermal processes, rather than the primary events directly associated with the acceleration of relativistic particles that produces the high-energy gamma-ray radiation.

Cosmic experiments devoted to the study of high-energy (more than tens of MeV) gamma-ray radiation are still very few in number: the American *SOLAR MAXIMUM MISSION* (1980–1989) and *COMPTON-GRO* (from 1991 to the present) satellites, the Soviet–French *Gamma* observatory (1990–1992), and the *Phobos* instruments on board the *Granat* spacecraft [5]. The number of solar flares detected at high gamma-ray energies (gamma-ray flares) is also few. Therefore, each new gamma-ray flare is of primary scientific interest.

This paper summarizes our analysis of *Gamma-1* data on solar gamma-ray flares. We present the temporal and spectral characteristics of the fluxes of gamma-ray photons generated during solar flares. We propose a scenario for the generation of high-energy solar gamma rays based on our analysis of these characteristics.

2. OBSERVATIONS AND REDUCTION TECHNIQUES

The *Gamma* observatory was designed chiefly for studying primary electromagnetic radiation at energies from a few tens of keV to tens of GeV. In July 11, 1990, the observatory was placed into a circular orbit with a height of about 400 km, an inclination of 51.6°, and a revolution period of 92 min, where it remained in operation until February 28, 1992. The main instrument on

1063-7729/00/4406-0389$20.00 © 2000 MAIK "Nauka/Interperiodica"

board the observatory was the large *Gamma-1* telescope, designed primarily for investigating discrete sources of Galactic gamma radiation at energies from 30 MeV to tens of GeV. The total exposure time for this experiment reached 2700 h. Measurements were conducted in two modes: observation of a single object in one orbit or observation of two different objects in one orbit, with appropriate reorientation of the telescope axes. The duration of measurements during one orbit was about 40 min in the first mode and ~70 min in the second mode, in total for both sources.

When detecting individual gamma-ray photons with the *Gamma-1* telescope, the information obtained by all the telescope detectors was recorded in output data sets, which then formed the input material for the experimental database. This database included a complete set of information on the recorded radiation fluxes, the location and conditions of the measurements, and other auxiliary information.

The *Gamma-1* telescope has the following general physical characteristics. The effective area for normal incidence of 100-MeV gamma-ray photons is about 180 cm^2; this area reaches a plateau of about 300 cm^2 at photon energies above 300 MeV. The times when the gamma-rays are recorded are established to better than 0.1 ms. The telescope has a sensitivity angle of about 12°. During observations of the active Sun, the telescope axis is aligned with the direction toward the Sun to an accuracy of ten arc minutes. The energy resolution of the four-section scintillation calorimeter incorporated into the *Gamma-1* telescope is about 70% at an energy of ~100 MeV and ~30% at an energy of ~1 GeV [6]. The total thickness of the calorimeter is 7.8 radiation lengths.

In most cases, we used original methods in our analyses of the experimental data. For example, in our temporal analyses, we used a sliding mean frequency (SMF) method based on the statistics of the time intervals, rather than the counting statistics, as is usually done. We also applied this method to identify weak flares, with additional allowance for the properties of the solar gamma-ray radiation detected in "strong" gamma-ray flares. A least directional divergence method was used to reconstruct the spectral characteristics of the radiation. This method allowed us to reconstruct the spectrum without applying any rigorous assumptions about its shape. The essence of the procedures we employed is as follows.

The SMF method. When examining time series, two different approaches can be used: determining the number of counts over a fixed time interval (counting statistics) and analysis of the time intervals between a given number of recorded events (interval statistics). In the case of powerful solar flares, we considered the reciprocal of the time interval between a given number of events, which corresponds to the mean intensity of the measured flux.

Assuming that the count rate is constant in the time interval T_n between the first and nth events and taking into account the dead time of the instrument, the SMF is determined by the formula [7]

$$\nu = (n-1)/(T_n - \Sigma\tau_i), \quad (1)$$

where the summation is performed over $(n-1)$ successive events and τ_i is the dead time, which is generally different for different events. This quantity is a "mean" frequency because it is determined for some number of events; the term "sliding" is used because the value of ν is assigned to each event in succession. As shown in [8], analyses of time series using the SMF method make it possible to determine the temporal structure of highly variable flows better than can be done using counting statistics.

Method for isolating weak flares. In the first papers on solar flares observed using the *Gamma-1* experiment [9], only large-scale structures of the temporal histories of powerful solar flares were analyzed. Later, in studies of the active phase of the powerful March 26, 1991, and June 15, 1991, gamma-ray flares [6, 8], isolated, very short bursts of gamma-ray emission were detected. Their intensity exceeded the background level by many orders of magnitude. This feature (the presence of sharp bursts of emission) was used to extract "weak" solar gamma-ray flares from the database. We compared the SMFs determined over five and 14 intervals (SMF5 and SMF14) and used an excess of SMF5 over SMF14 in terms of standard deviations as a criterion for identifying individual short bursts. A study of individual short bursts during the March 26, 1991, and June 15, 1991, flares showed that we should adopt a minimum excess of five σ. In this case, an individual short burst should consist of three or more gamma-ray photons separated in time by no more than 1.2 s. This criterion diminishes the chance that random pulses could be taken to be real bursts, and also preserves real bursts that are observed during powerful events. The final step in isolating weak gamma-ray flares was to distinguish groups of short bursts and determine if they were correlated in time with solar flares at other energies, primarily with optical and X-ray flares.

Least directional divergence (LDD) method [10]. The desired spectrum $I(E_0)$ can be determined from the equation

$$I(E_0)S(E_0) = \int N(E_u)F^{-1}(E_0/E_u)d(E_u),$$

where E_0 is the real (true) energy of a incident and recorded particle; E_u is the particle's measured energy; $N(E_u)$, the spectrum of measured gamma-ray photons with energy E_u; $I(E_0)$, the energy spectrum of the incident recorded radiation; $S(E_0)$, the instrumental function determining the dependence of the light collection efficiency of the instrument on the energy E_0 of the incident particle; and $F^{-1}(E_0/E_u)$, the *a posteriori* probability that the energy of the recorded particle lies in the range E_0–$E_0 + d(E_0)$, assuming that the measured (reconstructed) energy is E_u. The kernel $F^{-1}(E_0/E_u)$ is the reciprocal of the usual kernel $F(E_u/E_0)$ specifying

Characteristics of investigated solar flares

Characteristic	Flare					Note
	Mar. 26, 1991	June 15, 1991	Oct. 27, 1991	Oct. 29, 1991	Dec. 08, 1991	
Flare strength	3B/X4.7	3B/X12	3B/X6.1	SF	3N/M1.2	H_α line data
Heliocoordinates	S28W23	N33W69	S13E15	S09E62	N18E19	
				S13E35		
				S10E10		
				S18W09		
Onset	20^h26^m	6^h33^m	5^h38^m	10^h17^mE	5^h06^m	
				10^h17^mE		
				10^h18^mE		
				10^h32^m		
Maximum	20^h36^m	8^h31^m	5^h49^m	10^h19^m	5^h53^m	
				10^h31^m		
				10^h19^m		
				10^h32^m		
Duration	1^h11^m	4^h44^m	1^h20^m	24^m	1^h52^m	
				24^m		
				9^m		
				13^m		
Visible area (in millionths of solar disk area)	557	436	502	36	560	
				25		
				16		
				–		
Start of Measurement	20^h25^m	8^h38^m	5^h47^m	5^h47^m	5^h05^m	Gamma-ray emission data
Gamma-ray peak	20^h28^m	–	–	10^h27^m–10^h32^m	5^h22^m–5^h23^m	
Decay constant for the first phase	35–40 s	>500 s	130 s	–	–	
Transition time	20^h31^m	8^h48^m	5^h50^m	–	–	
Decay constant for the second phase	~17 min	~83 min	–	–	–	

the probability that the reconstructed energy lies in the range E_u–$E_u + d(E_u)$, provided that E_0 is the true energy of the recorded photon. The probability $F(E_u/E_0)$ is usually determined either via calibration of instruments mounted in accelerators or from numerical calculations. $F^{-1}(E_0/E_u)$ is the inverse function to $F(E_u/E_0)$; it is determined by Bayes' theorem and depends on the recorded spectrum $I(E_0)$. This last circumstance allows us to use a recurrence scheme with respect to $I(E_0)$, which was demonstrated to converge in [10], independent of the initial approximation used. On account of the limited statistics, we usually posed restrictions on the form of $I(E_0)$, which reduce to the requirement that this function be a decreasing function of E_0. The errors in the reconstructed spectrum were determined by the bootstrap method [11], in which $N(E_u)$ is assumed to be the parent population of the recorded particle distribution.

3. RESULTS OF THE OBSERVATIONS

Analyses of the characteristics of solar gamma-ray flares have been carried out in a number of studies [9, 12–14]. However, our modifications of the reduction techniques employed enabled us to reveal new temporal and spectral features of three powerful flares occurred in March 26, June 15, and October 27, 1991, and to detect and analyze the two weaker solar events of October 29 and December 8, 1991. Some characteristics of these five flares are presented in the table. The

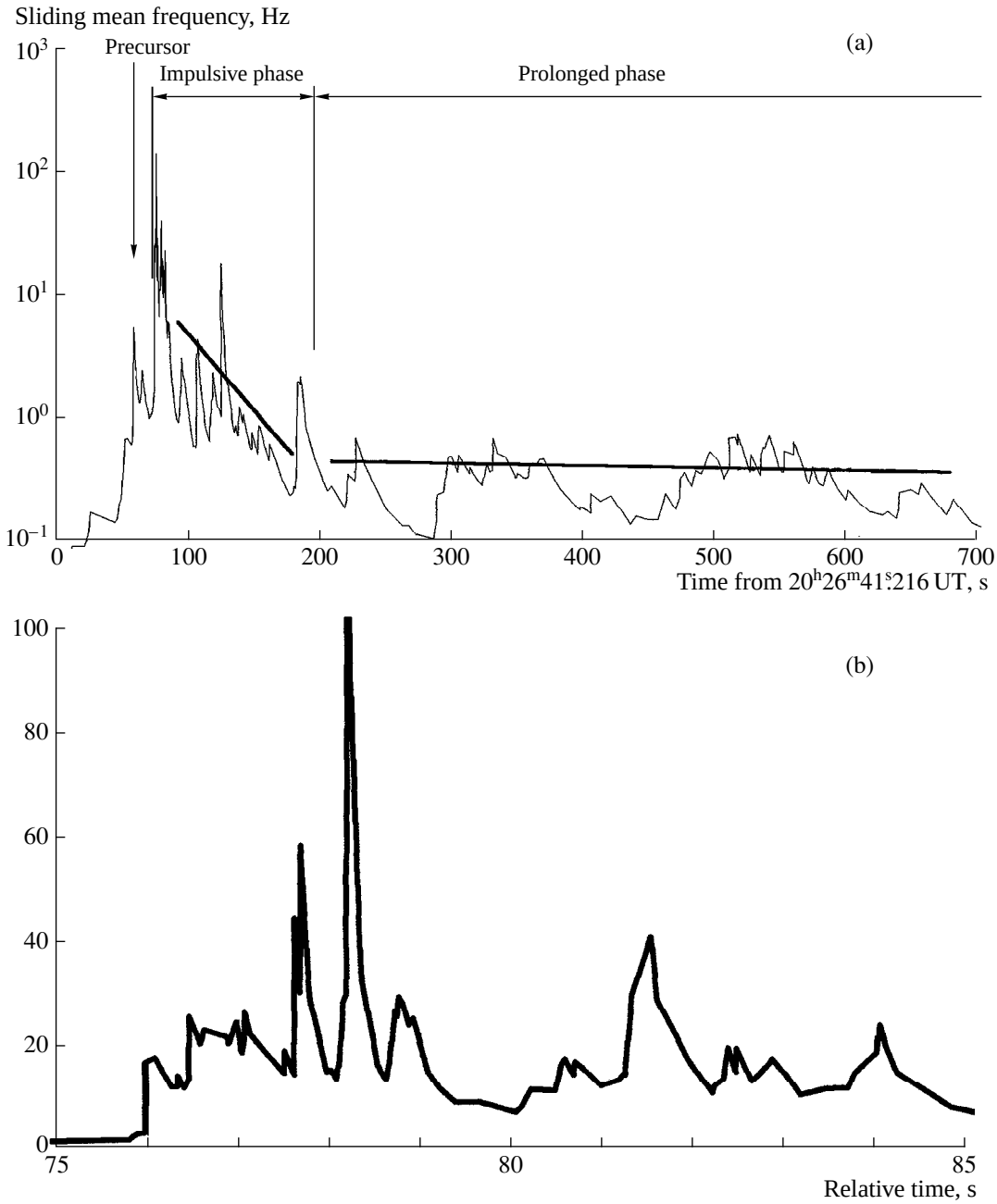

Fig. 1. Temporal characteristics of the March 26, 1991 solar gamma-ray flare.

optical and X-ray data are taken from the *Solar Data* catalog of solar flares. The visible area of active flare regions is expressed in millionths of the solar-disk area. We derived the characteristics of the gamma-ray emission in the present study.

March 26, 1991 flare. This flare was very strong (3V) in the optical. The soft X-ray flux (from 1 to 8 Å) also corresponds to a powerful (X4.7) flare. The flare occurred in the central part of the disk, at the point with heliocoordinates 28° S and 23° W.

The gamma-ray emission began at $20^h27^m57^s$, two minutes after the onset of the optical flare and eight minutes after the onset of the thermal X-ray emission, and lasted about 15 min [6]. Figure 1a presents the temporal history of the flare constructed using the SMF method and determined over five intervals (see, for example, [6]) on a semilog scale (the time scale zero is $20^h26^m41^s.216$ UT). The gamma-ray flare began as a weak "precursor," for which the telescope count rate increased from 0.1 Hz (background level) to 1 Hz.

Within 15 s, an active flare phase with a duration of three minutes began, characterized by sharp increases in the emission intensity against the background of a general exponential decay. The gamma-ray continuum of the March 26, 1991 flare included two temporal components: fast (with duration ~3 min and decay constant 35–40 s) and slow (with duration > 10 min and decay constant ~17 min). At longer times, at roughly 300–400 s and 450–550 s (Fig. 1a), two waves with some intensity increase can be seen.

The structure of the major burst in the flare, with duration ~10 s, is shown in Fig. 1b (see, e.g., [7]). It consists of two subbursts: the first at 76–79 s and the second at 80–85 s. These subbursts, in turn, were divided into separate emission peaks. The first subburst included three peaks (short pulses) with widths varying from 0.04 to 0.2 s and maximum rates of 60, 140, and 30 Hz. In the second short burst of the flare, a peak with width 0.3 s and a rate of 40 Hz is visible. The probabilities that these peaks are random estimated from counting statistics are rather low: 4.5×10^{-2}, 2.1×10^{-4}, and 3.3×10^{-1} for the first subburst, and 1.3×10^{-2} for the second subburst, thus demonstrating the presence of fine structure in the active phase of the gamma-ray flare. It would be very hard to distinguish these short bursts using counting statistics.

The energy spectrum of the flare, reconstructed based on the gamma-ray photons recorded during the first 145 s of the active phase assuming a decreasing spectrum for the recorded emission, is shown in Fig. 2a by the small squares. We compared the reconstructed spectrum to the spectrum predicted for gamma-ray photons generated during the interaction of beams of accelerated protons and electrons with matter (for details, see [8]). The calculated model spectrum for the gamma-ray photons is shown by the solid curve in Fig. 2a. It is obvious that the experimental points are in good agreement with the model spectrum. This agreement was obtained for the case of gamma-ray emission into the rear hemisphere relative to the proton beam, which is quite natural for a central-disk flare. The index for the particle spectrum is the same for electrons and protons ($\alpha = -3$), while the electron-to-proton ratio $K = 100$. The value of K is given for electrons at energies from 10 to 100 MeV and protons at energies from 0.5 to 100 GeV.

Changes in the gamma-ray emission spectrum during the March 26, 1991 event have been described in the literature (see, e.g., [15]). In the present paper, we also follow variations in the spectrum during the flare by introducing the so-called hardness parameter $K_1 = N(>120\ \text{MeV})/N(<120\ \text{MeV})$, where $N(>120\ \text{MeV})$ and $N(<120\ \text{MeV})$ are the numbers of recorded gamma-ray photons with the indicated energies. The boundary energy, 120 MeV, is chosen to separate low-energy gamma-rays associated with electrons from high-energy gamma-rays resulting from the decay of neutral pions produced by protons. Figure 2b plots the time dependence of K_1. The spectrum varies appreciably with time and becomes harder in the transition to the second phase of the flare.

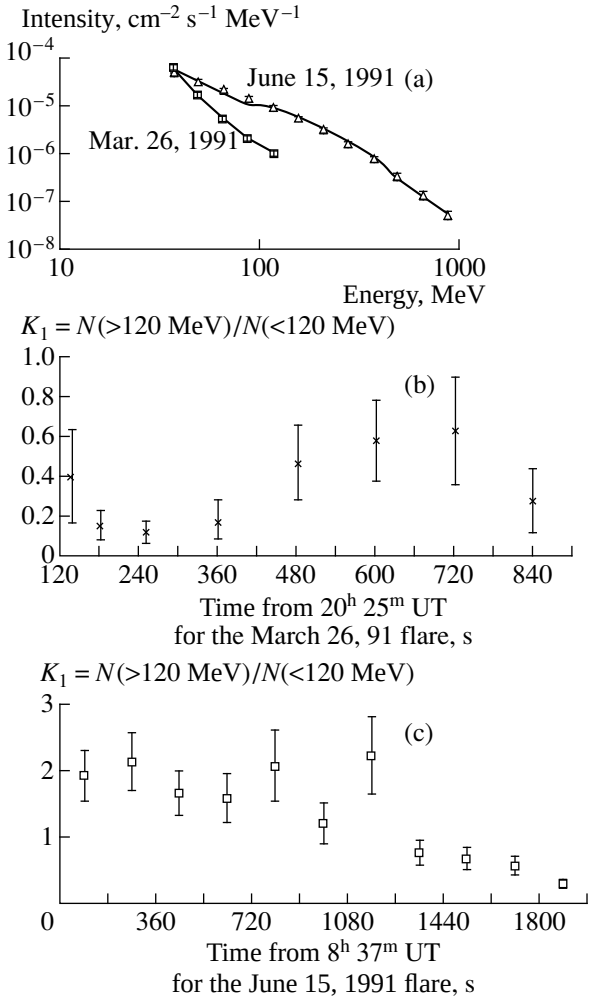

Fig. 2. Spectral characteristics of the March 26 and June 15, 1991 solar gamma-ray flares.

Thus, in the March 26, 1991 gamma-ray flare, which was observed in its entirety, we revealed (1) a short active phase with a duration of a few minutes, in which short (0.1–1 s) bursts of emission are detected against the background of an overall flux decrease with a decay constant of the order of a few dozen seconds and (2) a subsequent slow (prolonged) phase with a duration exceeding 10 minutes and a decay constant of about 17 min, which had no such bursts, only repeated weak pulses. The gamma-ray energy spectrum is the sum of contributions from electron bremsstrahlung and pion-decay gamma rays produced by the proton beam. In the transition to the second phase, the gamma-ray spectrum becomes harder, which probably reflects the increasing role of the proton beam.

June 15, 1991 flare. This is the most powerful of all the recorded flares. Its optical and X-ray strengths

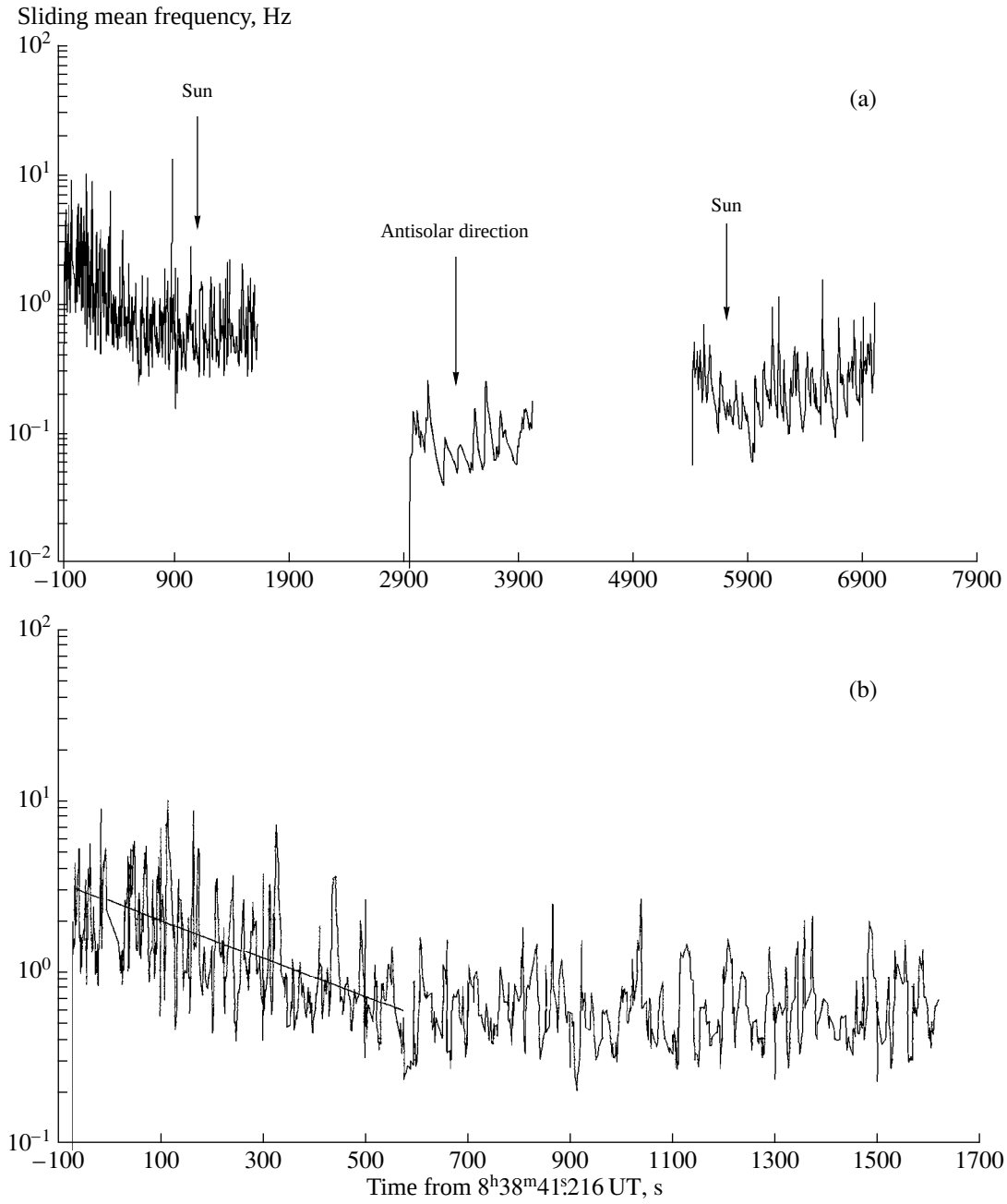

Fig. 3. Temporal characteristics of the June 15, 1991 solar gamma-ray flare.

were 3B and X12+, respectively. The flare occurred near the limb and had coordinates 33° N and 69° E.

The recording of the gamma-ray emission spectrum began at 08^h37^m UT, 20 minutes after the onset of the optical and X-ray flares. The initial part of the gamma-ray flare was obscured by the Earth. Figure 3 (see [8]) shows the temporal behavior of the flare measured using the SMF method. The time of the Brazilian magnetic anomaly is excluded; the time scale zero corresponds to $8^h38^m41^s.323$ UT. An exponential decrease in the emission with decay constant $\tau_1 = 410 \pm 80$ s is apparent during the first ~600 s, which then makes a transition to a quasi-constant count rate above the background level, which can be determined from measurements in the antisolar direction. A slightly decaying flux of gamma-ray photons was observed over two orbits, with an overall duration more than two hours and decay constant $\tau_2 = 83 \pm 7$ min.

Individual short bursts are present in the temporal profile of the gamma-ray flux (Fig. 3b). To ascertain

whether these bursts are statistical fluctuations, we compared the experimental and model SMF distributions [16] separately for the decaying (first 600 s) and quasi-constant (600–1700 s) fluxes. The probabilities that the calculated and observed distributions coincide are 5×10^{-5} and 0.3 for the decaying and quasi-constant fluxes, respectively. From this, we can draw a quite definite conclusion: The short bursts superposed on the decaying flux cannot be statistical fluctuations, and a significant fraction of them with SMF > 2 Hz are due to real intensity bursts. Thus, as on March 26, 1991, we observe two different phases of gamma-ray generation: the first (impulsive) phase, in which there are short bursts of gamma-ray emission, and the second (slow) phase, in which there are no such bursts, and there is a gradual decrease of the gamma-ray intensity. Note that the June 15, 1991, active phase of gamma-ray generation coincides in time with the second outburst of radio emission at 15.4 GHz [17, 18].

Figure 2a shows (i) the experimental spectrum reconstructed based on the first 1700 s of observations, assuming that the spectrum monotonically decreases with energy (triangles), and (ii) the calculated model spectra (solid curve). The best agreement between the calculated and experimental spectra in the case of isotropic gamma-ray emission is obtained for an accelerated-particle spectral index $\alpha = -3$ and an electron-to-proton ratio $K = 30$ (for the same electron and proton energy ranges as for the March 26, 1991 event). The model calculation without the electron component differs significantly from the low-energy observations and must therefore be rejected. This comparison has shown that electrons are present in the accelerated beam, even at such large times after the onset of the flare (20–50 min). Since electrons are rapidly lost from the beam as a result of synchrotron losses, their presence is an important argument in favor of repeated acts of acceleration.

The variation of the gamma-ray spectrum within the recorded part of the flare (expressed in terms of the hardness parameter K_1) is shown in Fig. 2c. The initially fairly hard spectrum softens with time.

The June 15 and March 26, 1991, gamma-ray flares differ considerably (despite the absence of the initial part of the June 15 flare). They have different durations, energy spectra, and spectral variabilities. Of course, these flares do differ in power (strength) but not very much. Instead, the observed differences are the result of the geometry of the gamma-ray observations: Because the March 26 flare is on the disk, the recorded gamma-ray photons are "forced" to fly into the rear hemisphere relative to the proton beam, whereas, in the June 15 limb flare, they escape isotropically. Qualitative model calculations show that the very different spectra of the March 26 and June 15 flares can be produced by particle beams with similar compositions and spectra.

October 27, 1991 flare. This powerful (3B/X6.1) flare occurred at the center of the disk, at heliocoordinates 13° S and 15° E. The October 27 *Gamma-1* observation began after the satellite entered the illuminated part of the orbit, nine minutes after the onset of the optical flare. The flux of gamma-ray emission was observed for roughly 200 s, when it ceased to be discernible owing to an increase in the background level due to the movement of the satellite into a high-latitude region.

The temporal history of the gamma-ray flare is shown in Fig. 9a [8]. Note that the event occurred near the Brazil Magnetic Anomaly and at a time when the Cherenkov counter of the telescope was inoperative, which considerably increased the background count rate. These shortcomings adversely affected the amount and quality of information obtained.

The spectrum for the first 145 s recorded, reconstructed assuming that the spectrum decreases with energy, is shown by the squares in Fig. 9b [8]. The spectrum can be approximated by a power law with index $\alpha = -3.15 \pm 0.16$. The continuous curve in Fig. 9b [8] represents the results of the model calculation. The best agreement between the experimental and calculated spectra is achieved for the following conditions: The gamma rays are emitted into the rear hemisphere relative to the proton beam and are isotropic for the electrons, the particle spectral index $\alpha = -3$, and the electron-to-proton ratio is $K = 100$. We present the spectrum's variability (time dependence of K_1) in Fig. 9c [8]. The spectrum initially hardens (this probably coincides with the end of the active gamma-ray flare phase), then remains constant.

By and large, the characteristics derived for the October 27, 1991 flare coincide with those for the March 26, 1991 flare, as is expected, since both flares originate in the central portion of the disk. Here, again, the geometry for the gamma-ray flux with respect to the particle beam proves to be the decisive factor.

December 8, 1991 event. The strength and coordinates of this solar flare are indicated in the table. Figure 4a shows the temporal history of the gamma-ray emission [19]. We observe a general flux enhancement and the presence of some sharp bursts and pulses, whose intensity and duration resemble the repeated pulses in the active phase of powerful flares. The poor counting statistics hinder analysis of individual short bursts, but peaks detected using our method for identifying weak bursts (indicated by the squares) may be real.

Because of the poor statistics, we could not reconstruct the gamma-ray spectrum, and it is replaced by the hardness parameter K_1. Figure 4b (see also [19]) shows the time dependence of K_1, which indicates that the spectrum hardens near short bursts and then rapidly softens. This is similar to the spectral behavior at the end of the active phase of the June 15, 1991, flare and may provide evidence for the reality of the distinguished gamma-ray flux. Note also that the geomagnetic index K_p did not exceed 2+ during the recording of this event (according to data reported in [20]), indicating quiet geomagnetic conditions.

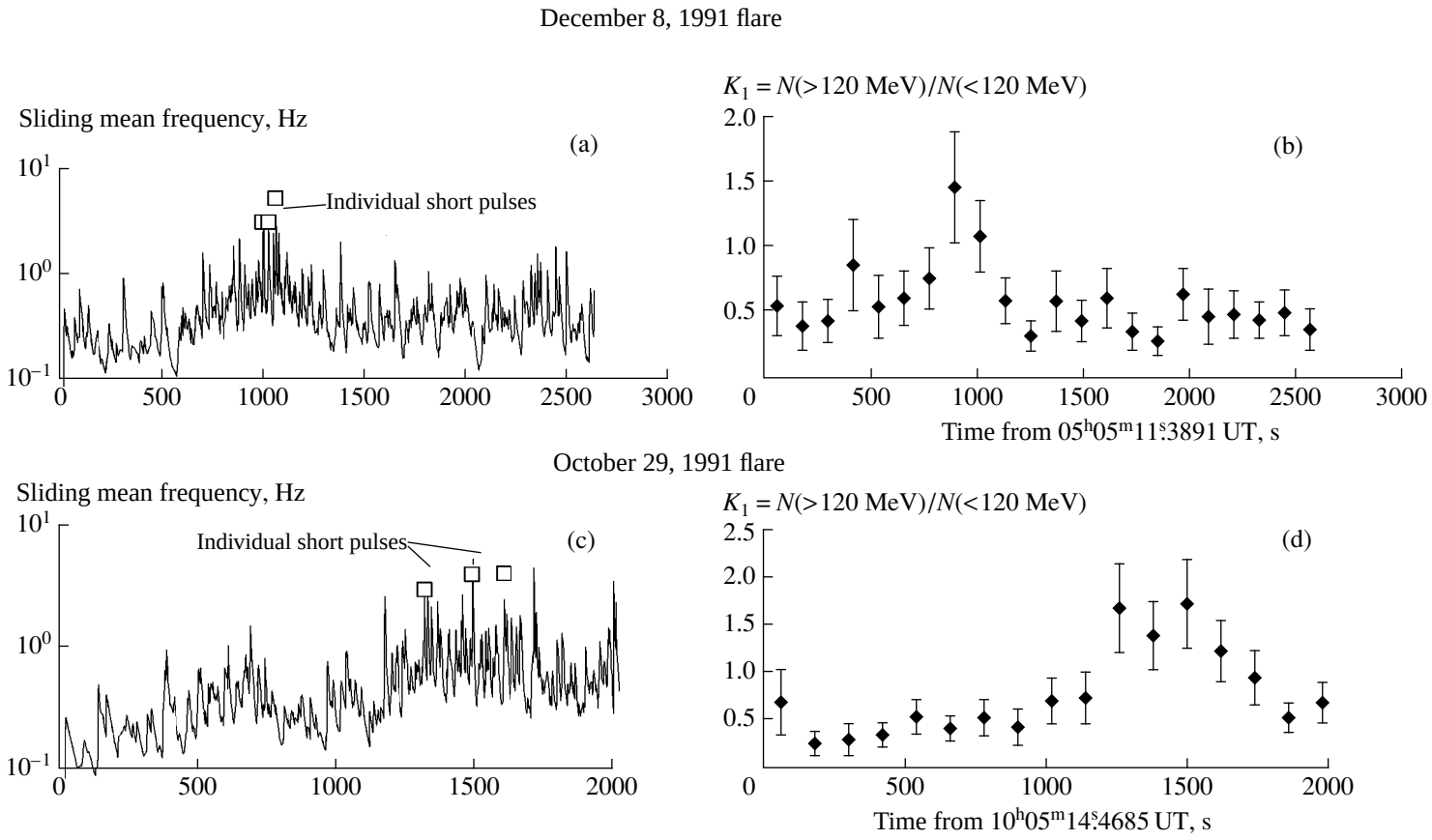

Fig. 4. Temporal and spectral characteristics of the December 8, 1991 (a, b) and October 29, 1991 (c, d) gamma-ray flares.

October 29, 1991 event. The strengths and coordinates of four possible identifications for the October 29, 1991 gamma-ray flare are given in the table. The temporal profile of the gamma-ray flux is shown in Fig. 4c (see also [19]). It displays all the characteristic features of gamma-ray flare emission in the active phase: a flux increase, individual short bursts, and repeated pulses. The bursts labeled by squares may be real. The time dependence of K_1 presented in Fig. 4d (see also [19]) shows a hardening of the gamma-ray spectrum near individual short bursts. This argues in favor of the reality of the gamma-ray flare. However, the K_p index was 6+ during the event, indicating magnetospheric disturbance and raising the possibility that the gamma-ray flux could be due to the background conditions.

Both weak gamma-ray flares are difficult to detect above the background level; their parameters are very uncertain, and they cannot provide new data on accelerated particle beams. However, it is important that these flares were identified only because of the presence of individual intensity bursts and would not have been detected using counting statistics alone. This can be considered a test of our method for distinguishing weak flares and, also, a reflection of the physical explosive processes occurring in weak solar flares.

4. SIMULATION OF EVENTS AND DISCUSSION

When observing the Sun with the *Gamma-1* telescope at the maximum of solar cycle 22, sharp bursts of high-energy gamma-ray emission were detected during three powerful and two moderate optical solar flares. For the first time, we observed solar gamma-ray flares with energies of several GeV and durations reaching several hours. Along with measurements carried out simultaneously by the *COMPTEL* and *EGRET* instruments on board the *COMPTON-GRO* orbiting station (see, e.g., [21]), these results initiated a new phase of investigations of solar gamma-ray flares and solar activity. Although no more than a dozen gamma-ray flares have been detected, common characteristic features can be distinguished.

Our results show that a gamma-ray flare goes through two evolutionary stages. The first, "active," phase with duration several minutes covers the impulsive phase of the corresponding powerful optical solar flare. It is characterized by a sharp rise of the gamma-ray emission, followed by an exponential decrease with a time constant from 10 to 100 s. Individual short bursts of emission with duration 0.1–1 s can be detected against the continuum.

The second, "prolonged," phase, with a duration from a few tens of minutes to hours, coincides in time with the major phase of the solar optical flare. It is characterized by a slow decrease in the gamma-ray flux with a decay time of the order of a few tens of minutes. No individual short bursts were detected during this phase. In the transition from the active to the prolonged phase, the gamma-ray spectrum hardens.

Note a further important feature of the detected gamma-ray flares. On the one hand, all the gamma-ray flares occurred in extremely large (in area) active regions of the solar disk. On the other hand, any optical flare associated with a large active region (if its active phase was observed) could become a source of high-energy gamma-ray bursts. This seems to be related to the complex magnetic-field structures of the solar corona in large active regions, which makes it easier for magnetic lines of force to reconnect and annihilate.

The assertion that individual short bursts of emission associated with repeated acceleration events are present in a flare is of fundamental importance for interpretations of the temporal profiles of solar flare gamma-ray emission. To verify this assertion, we developed a program based on the GEANT package [22] to simulate the generation of high-energy gamma-ray radiation in the solar corona. This program is briefly described in [23].

We simulated the March 26, 1991, gamma-ray flare's temporal profile as follows. We considered a magnetic loop in the solar corona, with its magnetic-field configuration and matter distribution taken from [24]. The initial parameters of the accelerated particles at the injection point at the apex of the magnetic loop were random. The angular distribution of the injected particles (protons and electrons) was assumed to be isotropic and the energy spectrum to be power-law. The direction of motion and the time of exit from the interaction region for each secondary gamma-ray photon were fixed relative to the time of injection of the charged particles. Initial, nonzero times were assigned to some fraction of the injected particles to imitate repeated acceleration events. The energy and temporal distributions of the gamma-ray photons for all the injected particles yield, respectively, the spectrum and temporal profile of the flare. When modeling the passage of the particles through the solar atmosphere, beginning at a certain time, it was possible to alter the plasma turbulence level, thereby changing the pitch-angle of the scattering and conditions for particle capture, and, accordingly, the rate of generation of gamma-ray photons.

The presence of short bursts of gamma-ray emission in the temporal profiles of individual sharp flares can be accounted for by changes in the density in the region in which the radiation is generated, variations in the level of magnetic turbulence in the solar corona, and additional particle acceleration events. The experimental data indicate short durations for individual gamma-ray bursts. This virtually eliminates the two first possible origins for the appearance of the sharp bursts, since they would require rapid changes of the magnetic turbulence level or density by several orders of magnitude. Agreement with the experimental data can be achieved only if we assume the existence of repeated charged-particle acceleration events. Figure 5 (see also [23]) shows the experimental and calculated temporal pro-

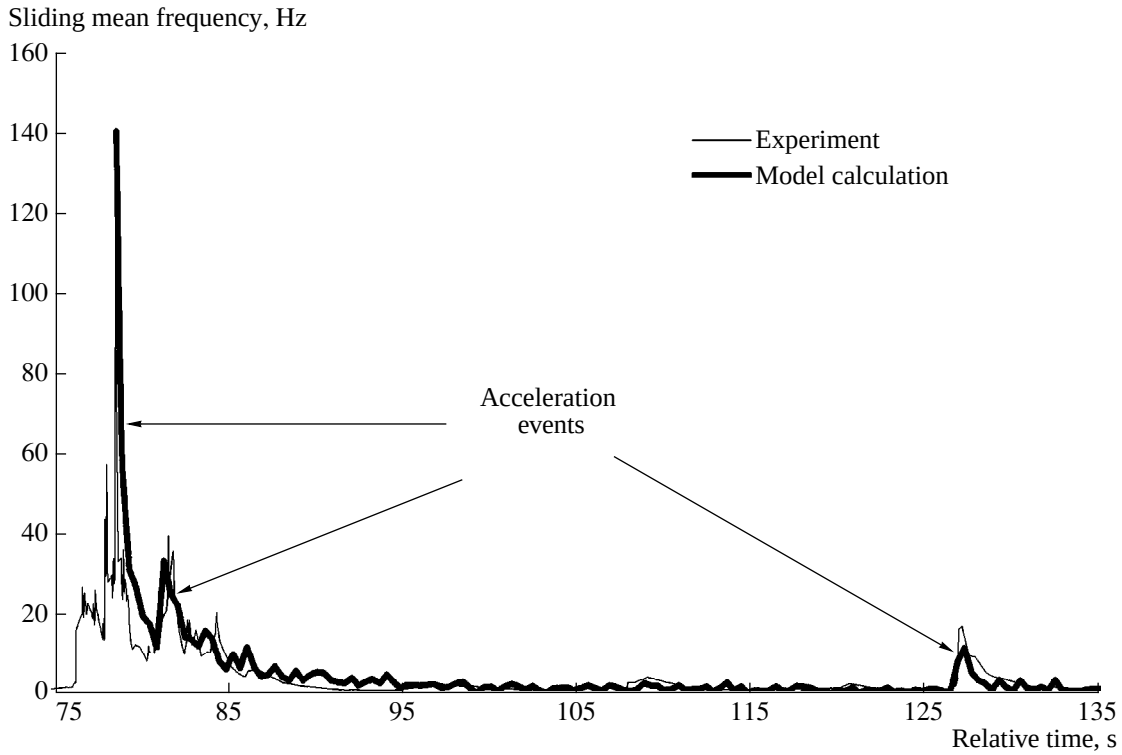

Fig. 5. Model and experimental temporal profiles of the March 26, 1991, gamma-ray flare.

files for the gamma-ray emission during the March 26, 1991, solar flare. Three additional charged-particle acceleration events (injection times) are assumed in the model profile, at the relative times ≈78 s (the main outburst), ≈81 s, and ≈127 s (Fig. 5). The amplitudes of the injected particle fluxes in these events are in the ratio 8 : 4 : 1. The turbulence level at the initial time is 3.2×10^{-7} erg/cm^3 and falls off exponentially with time, the stopper ratio is 30, and the magnetic field strength is 50 G. Figure 5 demonstrates a satisfactory agreement between the model and experimental temporal profiles of the flare. Note that the duration of the first, major burst of emission (about 40 ms) is also in reasonable agreement with the calculations.

Based on the measurements and simulations performed in this study, we can interpret the general pattern of solar gamma-ray flares as follows. The individual short bursts of gamma-ray emission observed in the active phase are associated with individual charged-particle acceleration events. The duration of these bursts is determined by the duration of the acceleration process and the rate of generation of the gamma-ray radiation. The widths of individual bursts in the March 26, 1991, flare were 40–200 ms. For such durations, the accelerated particles must be located in a rather dense medium, where it is difficult to accelerate them to tens or hundreds of MeV. This eliminates the possibility of gamma-ray generation by particles in magnetic loops and suggests that the radiation was generated during the passage of the particle beam from the corona to the chromosphere. In this case, the emission of a relatively soft gamma-ray spectrum can be explained by the position of the observer relative to the direction of propagation of the particle beams (corresponding to emission into the rear hemisphere with respect to the initial particle momentum). If the total-intensity decrease in the active phase is determined by the rate of loss of particles from the capture region, the size of the magnetic loop does not exceed 5×10^8 cm.

The decay constant of the gamma-ray emission in the June 15, 1991 flare is more than a factor of ten larger than in the March 26, 1991 flare, suggesting a much larger magnetic loop in this case. Moreover, the repeated short bursts of gamma-ray emission on June 15, 1991 clearly have longer durations, and the gamma-ray spectrum is much harder than in the March 26, 1991 flare. We can reconcile these facts if the repeated acceleration of particles in the active phase of the March 26 flare took place in the lower part of the magnetic loop as a result of reconnection of magnetic lines of force at a boundary between adjacent magnetic flux tubes. In this case, the beam of accelerated particles maintains its direction and gives rise to a soft spectrum and short intensity bursts. The particle acceleration in the active phase of the June 15 flare could occur at the apex of a large coronal magnetic loop, for example, as a result of a current-sheet instability. This difference in the generation site could explain both the hardening of the spec-

trum and the durations of individual sharp bursts of emission.

The transition to the second (prolonged) phase of the flare occurs after the cessation of acceleration events associated with the reconnection of magnetic lines of force, current instability, etc. In the low-turbulence case, particles are trapped in a magnetic loop in the solar corona, where the gamma-ray radiation is now generated. Because the momentum distribution of the trapped particles becomes more isotropic, the gamma-ray spectrum hardens and takes on a "pion" form. The spectrum's hardness is also determined by the progressive increase of the fraction of protons in the trapped particle beam, since the electrons disappear more rapidly as a result of synchrotron losses.

This qualitative scenario of a solar gamma-ray flare is in reasonable agreement with the analyses of soft X-ray flares in [3, 25]. Recently, these calculations have been confirmed by *Yohkoh* measurements that have detected solar flares that are intermediate between purely impulsive and prolonged. Flares with prolonged soft X-ray emission (long-decay flares) have also attracted attention. It is tempting to compare this emission to the high-energy gamma-ray emission lasting several hours observed by us.

The long-decay phase of solar-flare X-ray emission is preceded by an active phase, which could be associated with the reconnection of magnetic lines of force, either in complex magnetic-field configurations in the solar atmosphere (possibly the case for the March 26, 1991 flare) or in vertical current sheets forming at the apex of a giant magnetic flux tube as a result of a coronal ejection (possibly the case for the June 15, 1991, flare). Evidently, magnetic reconnection can occur repeatedly, each time producing beams of accelerated relativistic particles, which are manifest as abrupt rises of the gamma-ray intensity in the temporal profiles of gamma-ray flares (note that such rises are also characteristic of moderate gamma-ray flares). The final slow decrease of soft X-ray emission observed on March 26, 1991, and June 15, 1991, is likely associated with thermal plasma emission in large-scale coronal structures. This stage is not accompanied by individual sharp gamma-ray bursts, indicating that rapid acceleration no longer occurs at this time.

In a more general astrophysical context, the solar flares studied here are one type of nonstationary eruptive process occurring on stars of late spectral types: UV Ceti and T Tau flare stars (active red dwarfs of spectral types K and M), rapidly rotating stars, RS CVn binary systems, etc. Solar and stellar flares have much in common, but substantial differences also exist. To better understand the diversity of stellar flares, it is of considerable interest to study them at high-energy gamma-ray energies.

ACKNOWLEDGMENTS

This work was supported by the Russian Foundation for Basic Research (project no. 96-02-17127) and the Ministry of Science of the Russian Federation (the "*Gamma-1*" project, section "Extra-atmospheric Astronomy" of the State Science and Technology Program "Fundamental Cosmic Research").

REFERENCES

1. R. Ramaty and N. Mandzhavidze, AIP Conf. Proc. **374**, 533 (1996).
2. M. S. Longair, in *High Energy Astrophysics* (Cambridge University Press, Cambridge, 1992), Vol. 1, p. 361.
3. K. V. Getman and M. A. Lifshits, *Energy Balance in Sources of Prolonged Soft X-ray Radiation on the Sun* [in Russian], Preprint No. 1 (1117), IZMIRAN (Institute of Terrestrial Magnetism, the Ionosphere, and Radio-Wave Propagation, Russian Academy of Sciences, Troitsk, 1999).
4. S. Masuda and J. Cato, in *Workshop on Solar Flares and Related Disturbances* (Hitachi, Japan, 1996), p. 52.
5. C. Barat, in *Proceedings of the Conference on Nuclear Spectroscopy of Astrophysical Sources*, Ed. by G. H. Share and N. Gehrels (AIP, New York, 1998), Vol. 395.
6. V. Yu. Chesnokov, H. M. Djantemirov, A. M. Galper, *et al.*, *Research of Powerful Solar Gamma-Flares in "Gamma-1" Experiment*, Biannual report 93/94, MEPhI (Moscow Institute of Engineering Physics, Moscow, 1995).
7. A. M. Gal'per, V. M. Zemskov, B. I. Luchkov, *et al.*, Pis'ma Zh. Éksp. Teor. Fiz. **59**, 145 (1994) [JETP Lett. **59**, 153 (1994)].
8. A. M. Khodarovich, *Temporal and Spectral Characteristics of Solar High-Energy Gamma-ray Flares from "Gamma-1" Data*, Candidate's Dissertation in Mathematical Physics (Moscow, 1998).
9. V. V. Akimov, V. G. Afanas'ev, A. S. Belousov, *et al.*, Pis'ma Astron. Zh. **18**, 167 (1992) [Sov. Astron. Lett. **18**, 69 (1992)].
10. M. Z. Tarasenko, *Least Directional Divergence Method for the Solution of Certain Mathematical-Statistical Problems in Experimental Nuclear Physics*, Candidate's Dissertation in Mathematical Physics (Obninsk, 1973).
11. G. A. Simpson and H. G. Mayer-Hasselwander, Astron. Astrophys. **162**, 340 (1986).
12. N. G. Leikov, V. V. Akimov, V. A. Volsenskay, *et al.*, in *Proceedings of Symposium on Recent Advances of High Energy Astronomy* (Toulouse, 1992).
13. V. V. Akimov, A. V. Belov, V. G. Kurt, *et al.*, in *Proceedings of 23rd International Cosmic Ray Conference* (Calgary, 1993), Vol. 3, p. 111.
14. A. M. Gal'per, V. M. Zemskov, G. E. Kocharov, *et al.*, Izv. Ross. Akad. Nauk, Ser. Fiz. **57**, 132 (1993).
15. V. Kurt, V. V. Akimov, and N. G. Leikov, AIP Conf. Proc. **374** (1995).
16. Yu. V. Efremova, Yu. V. Ozerov, and A. M. Khodarovich, Prib. Tekh. Éksp., No. 4, 33 (1997).

17. A. M. Galper, B. I. Luchkov, Yu. V. Ozerov, *et al.*, in *Proceedings of 25th International Cosmic Ray Conference*, (1997), Vol. 1, p. 169.
18. V. G. Kurt, V. V. Akimov, and N. G. Leikov, AIP Conf. Proc. **374**, 237 (1996).
19. A. M. Gal'per, Yu. V. Ozerov, A. M. Khodarovich, and S. B. Rinchinov, J. Mosc. Phys. Soc. (1999) (in press).
20. *Selected Geomagnetic Solar Activity Indices* (National Geophysical Data Center, 325 Broadway Mail Code E/GC2 Boulder, Colorado 80303-3328 USA).
21. N. Mandzhavidze, R. Ramaty, and D. L. Bertsch, AIP Conf. Proc. **374**, 225 (1996).
22. R. Brun and F. Carminati, *GEANT Detector Description and Simulation Tool* (CERN Program Library Long Writeup, October, 1994).
23. Yu. V. Ozerov, A. M. Khodarovich, S. B. Rinchinov, and B. I. Luchkov, J. Mosc. Phys. Soc. (1999) (in press).
24. N. Mandzhavidze and R. Ramaty, Astrophys. J. **389**, 739 (1992).
25. M. A. Livshits, J. Mosc. Phys. Soc., No. 6, 393 (1996).

Translated by A. Kozlenkov

Astronomy Reports, Vol. 44, No. 6, 2000, pp. 401–406. Translated from Astronomicheskiĭ Zhurnal, Vol. 77, No. 6, 2000, pp. 460–466.
Original Russian Text Copyright © 2000 by Kozlova, Somov.

Studying Coronal Holes through Observations of an HeI Infrared Line and the H_α Line

L. M. Kozlova and B. V. Somov

Sternberg Astronomical Institute, Universitetskiĭ pr. 13, Moscow, 119899 Russia

Received May 31, 1999

Abstract—New results from electrophotometric scanning of the solar disk in the HeI λ 10830 Å and H_α lines are presented. The intensity at the center of the HeI λ 10830.30 Å line is 1–3% higher in the regions of coronal holes than in quiescent regions; this is accompanied by a decrease in the size and contrast of the chromospheric network compared to the network in quiescent regions. Our observations in the HeI line revealed chains of "dark points" surrounding coronal holes. The $H_\alpha \pm 0.5$ observations show increased velocities of ascent near the dark points compared to the velocities inside coronal holes and in quiescent regions. It is proposed that the intensification and acceleration of the flows of solar plasma from the dark points are due to reconnection of the magnetic fields of the bipolar chromospheric network and the predominantly unipolar magnetic field inside the coronal holes. Our observations suggest that the same reconnection process takes place near the temperature minimum, in the presence of certain conditions at the boundary between coronal holes and bipolar active regions. The reconnection process produces plasma flows from the chromosphere to the corona, which are sufficient to form prominences. © *2000 MAIK "Nauka/Interperiodica".*

1. INTRODUCTION

Emission at the center of the H_α line and the HeI 10830 Å infrared triplet forms in the middle and upper chromosphere, and partially in the transition region between the chromosphere and corona [1]. Analysis of spatial and temporal variations in the parameters of these lines can give extensive information about the configuration, fine structure, and dynamics of the chromosphere at the corresponding heights (see [2–5] and references therein).

The HeI 10830.3 Å line is of particular interest for the identification and study of large-scale, weak-contrast structures such as coronal holes (see, for example, [6]). Coronal holes are thought to be a source of high-speed streams of the solar wind [7] and, consequently, thought to play an important part in solar–terrestrial connections [8]. The aim of the present paper is a more detailed study of the structure and properties of the boundaries of coronal holes and their role in the formation of high-speed solar-wind streams. We also consider the possible influence of coronal holes on the appearance and development of prominences, which is a closely related problem.

2. OBSERVATION AND IDENTIFICATION OF CORONAL HOLES

Photoelectric scanning of the solar disk in the HeI 10830 Å and H_α lines was carried out using the horizontal solar telescope of the Solar Physics Department of the Sternberg Astronomical Institute (Moscow State University) in 1996–1998. This telescope has the following basic parameters: diameter of the primary mirror 30 cm, focal length 1500 cm, diameter of the solar image in the plane of the entrance pupil of the spectrograph 140 mm, and first-order dispersion of the diffraction grating ≈1.6 Å/mm. The spectrograph pupils used were (0.1–0.2) × (1.0–2.0) mm. The solar emission was initially detected by a photomultiplier, with subsequent amplification, automatic recording, and simultaneous readout to a computer. The apparatus and observing method are described in more detail in [9].

Various regions on the solar disk were scanned by the spectrograph entrance pupil during the motion of the image when the guiding system was turned off. The exit pupil of the spectrograph was tuned to the center of the HeI 10830 Å or H_α line or some other spectral band. The recording time for a single scan was 1.5–2.5 min.

We used the results of the observations to construct two-dimensional intensity and isophote distributions for the solar regions under investigation. In a HeI isophote map with intensity steps of ≤0.033, we can clearly identify coronal holes as extended light regions with a suppressed chromospheric network (against the darker background of the quiescent chromosphere) [10]. In order to obtain unambiguous identifications, we compared all detected active formations with corresponding structures in various lines of spectroheliograms received from other observatories via the Internet, and also with H_α pictures, maps in the FeXIV line, and magnetograms published in *Solar Geophysical Data (SGD).*

1063-7729/00/4406-0401$20.00 © 2000 MAIK "Nauka/Interperiodica"

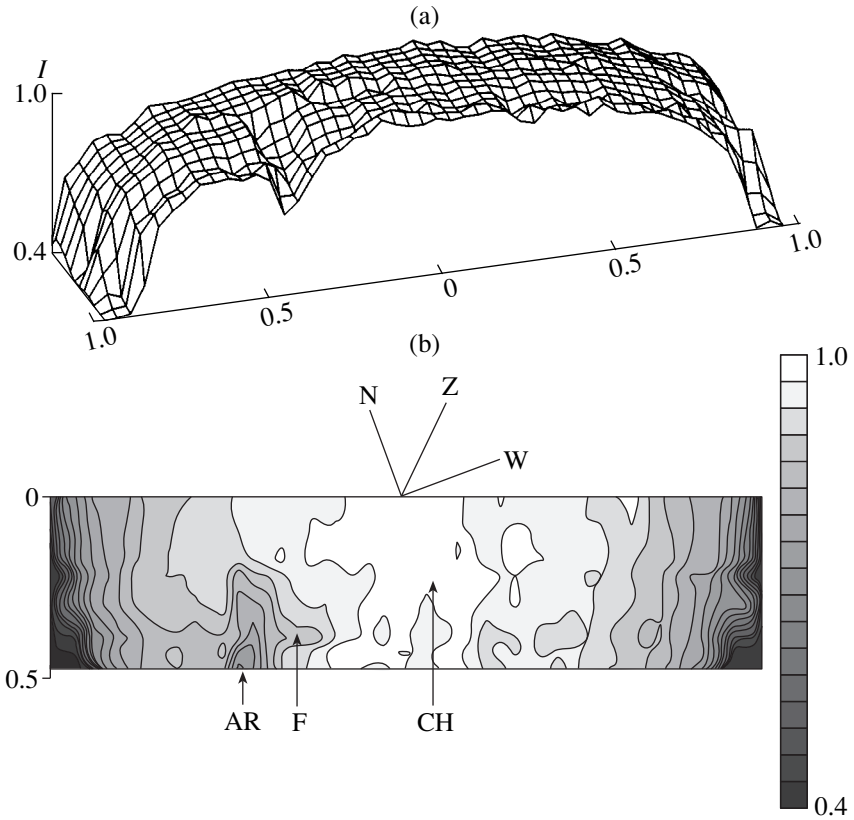

Fig. 1. Scans of the solar surface at the center of the HeI 10830 Å line: (a) two-dimensional intensity distribution and (b) map of intensity contours. The scale along the horizontal axes is in fractions of the solar radius.

3. OBSERVATIONAL RESULTS

3.1. Coronal Holes and Their Properties

Figure 1 presents a characteristic example of an intensity distribution, obtained on August 27, 1996, at the center of the HeI 10830 Å line for a strip of the solar disk passing through the active region 7986 NOAA. The orientation of this strip relative to the rotation axis, center of the disk, and vertical are shown in Fig. 1b. The strip passes along the diurnal parallel of the Sun. The spectrograph pupil was oriented along the solar vertical (Z). For convenience, distances along the horizontal axes are given in fractions of the solar radius.

The vertical axis of Fig. 1a plots the intensity at the line center. The intensity unit was the maximum in the intensity distribution for a quiescent region near the disk center. Figure 1b presents a contour map with intensity step 0.033 corresponding to Fig. 1a. In the intensity distribution and isophotes, we can clearly see darkening of the solar disk at the limb, darkening of an active region and filament (marked by the arrow F), and spikes of emission at the limb.

We identified as a coronal hole the brightest region in the central part of the disk in the intensity contour map, which disrupts the circular structure of the isophotes typical for the quiet Sun. In addition, this region is 3.3% brighter than the background, as is characteristic of coronal holes. The arrow AR marks the observed part of the active region 7986 NOAA, which has a large filament F. It extends along a neutral line of the photospheric magnetic field and intersects the entire active region (see also H_α picture in SGD).

Thus, there is no doubt about the identification of the observed structures. The isophotes at the center of the H_α line show that the coronal holes are less distinct than in the HeI line but can definitely be recognized as extended regions where the structure of the chromospheric network is absent or weak.

We processed over 50 scans of quiescent and active regions in the HeI 10830 Å line. The mean size of chromospheric network cells in quiescent regions was $(49.0 \pm 0.5)''$, and the mean brightness contrast with respect to a section drawn through the network cell centers is $(2.7 \pm 0.1)\%$. At the same time, the mean size of the network cells obtained from observations of six coronal holes is $(30.0 \pm 0.4)''$, and their mean contrast is $(1.4 \pm 0.1)\%$ [11]. These results indicate that, along with some increase in the emission intensity, there is a considerable decrease in the dimensions of the chromospheric network and its contrast in the HeI line near coronal holes, compared to quiescent regions.

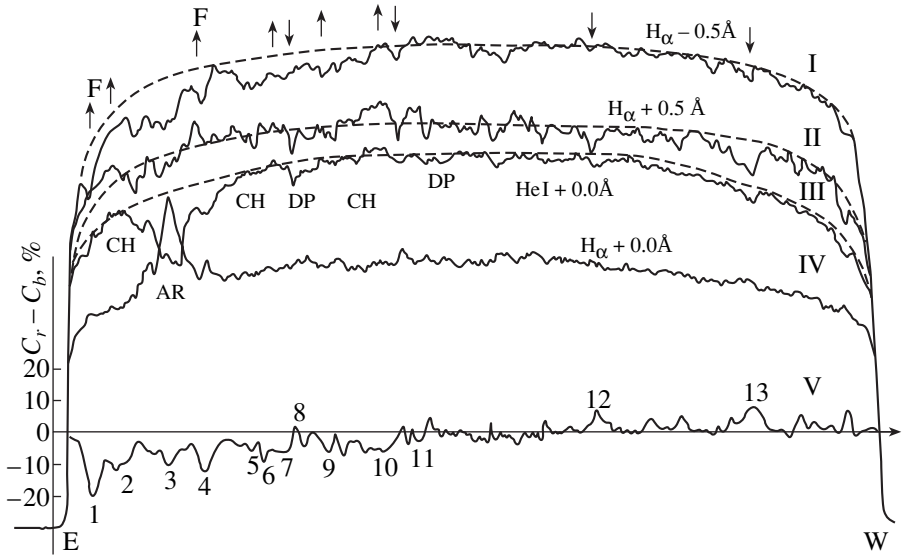

Fig. 2. Scans along a section of the solar surface in the H_α and HeI 10830 Å lines obtained on August 27, 1997: (I) H_α – 0.5 Å, (II) H_α + 0.5 Å, (III) center of the HeI 10830 Å line, and (IV) center of the H_α line. Curve V characterizes the differences of the brightness contrast $\delta C = C_r - C_b$ along the section under consideration.

3.2. Observations of Filaments

The isophotes in Fig. 1b clearly show that the filament F begins at the region of minimum separation between the active region AR and the coronal hole CH. This part of the filament is marked by the arrow F. We propose that the presence of a coronal hole very near the photospheric neutral line of a bipolar active region plays a role in the formation of prominences. Namely, there is magnetic reconnection of the bipolar arch structures of the active region and the unipolar vertical field of the coronal hole.

This efficient process results in considerable plasma upflow from the chromosphere to the corona. As shown in [11], this upflow is quite sufficient to produce large prominences above the photospheric neutral line. The required rate of reconnection is in agreement with the observed rates of annihilation of magnetic peculiarities in the photosphere. There are many such examples of the formation of streams and prominences at the boundary between an active region and coronal hole in our observations.

We should note two observed phenomena that, in our opinion, accompany the formation of prominences at the boundaries of active regions. First, as a rule, prominences usually appear in regions where the photospheric neutral line separating areas of the active region with different polarities substantially deviates from the solar meridian. Second, the magnetic-field gradients in regions of formation of prominences are not maximum. As is known, maximum field gradients are observed in active regions along the neutral line perpendicular to the meridian. This situation is most typical for solar flares, rather than for quiescent prominences.

Figure 2 presents an example of upflow in the form of a small filament at the boundary between the active region 8076 NOAA and a coronal hole observed on the solar disk on August 27, 1997. Scans I–IV of the same section, passing through the active region and the coronal hole, were obtained in three different parts of the H_α line profile and at the center of the HeI line. Scan III, representing the intensity distribution along the section at the center of the HeI line, reveals a coronal hole CH on both sides of the active region, in accordance with the aforementioned features (an increased emission level and decreased contrast of the chromospheric network [10]). Comparing scans III and IV, we can see that almost all the structures observed in absorption at the center of the HeI line are present in emission near the center of the H_α line.

Scan I was obtained in the blue wing of the H_α line, at wavelength $\lambda(H_\alpha)$ – 0.5 Å, and scan II was obtained in the red wing, at wavelength $\lambda(H_\alpha)$ + 0.5 Å. Curve V represents the distribution of the difference of the brightness contrasts for structures observed in the red and blue wings. The Doppler shift of the line due to the solar rotation gives corrections for the contrast differences of up to ±0.2%, and corrections for the velocities along the line of sight of up to ±0.4 km/s for points near the limb. The difference $\delta C = C_r - C_b$ characterizes the velocity of the plasma motion, and its sign indicates the direction of motion. The scale for δC for this curve is presented to the left of Fig. 2. Negative values of δC correspond to upflows, and positive values to downflows. Some characteristic regions of upflows and downflows are shown in the upper part of Fig. 2 near scan I by the upward and downward arrows.

To evaluate the velocities along the line of sight, we will use the "three λ" method [12]. The desired velocity

Velocities along the line of sight $v_{\parallel}$ observed in the section drawn in Fig. 2

Number of point	1	2	3	4	5	6	7	8	9	10	11	12	13
$v_{\parallel}$, km/s	−18.0	−20.1	−2.1	−7.6	−2.4	−2.4	−16.0	+1.5	−11.6	−16.0	−16.0	+2.3	+2.3

Note: 1, 2, and 4 are regions of upflow in the filament at the boundary between AR and CH; 3 is the center of AR; 5 and 6 are two regions of CH; 7, 9, 10, and 11 are regions of upflow in the vicinity of DP; 8 is a region of downflow at the center of DP; 12 and 13 are typical elements of the quiescent network.

is determined by substituting the measured intensities at the line center (I_c) and the red (I_+) and blue (I_-) wings into the expression

$$v_{\parallel} = -16.0\frac{\ln(I_-/I_+)}{\ln(I_-I_+/I_c^2)}\ \text{km/s}$$

in cases when a Gaussian approximation is sufficient to describe the line profile and $I_c^2 > I_+I_-$. If this condition is not satisfied, the radial velocity is calculated using the formula

$$v_{\parallel} = 23.5\ln(I_+/I_-)\ \text{km/s}.$$

We give the velocities $v_{\parallel}$ estimated using this method for some characteristic points in curve V in the table.

We can see in Fig. 2 and the table that the upward flows are maximum at boundaries between the active region and the surrounding coronal hole. The upflow marked in Fig. 2 by the arrows F to the right and left of the active region corresponds to a small filament, visible in the SGD H_α images. Note that the distribution of δC along the solar-disk section under consideration has a predominant upflow in the coronal hole (CH) and downflow at the boundaries of the quiescent network, with velocities up to 2.3 km/s.

3.3. Observation and Properties of Dark Points

The coronal holes observed at the center of the HeI 10830 Å line are nearly always surrounded by "dark points" with increased contrast relative to the surrounding quiescent network (denoted DP in Figs. 2, 3). The sizes of such points (at the moderate spatial resolution of our telescope) are ≈30000–40000 km, and their mean contrast relative to the local continuum is (11.5 ± 0.5)%.

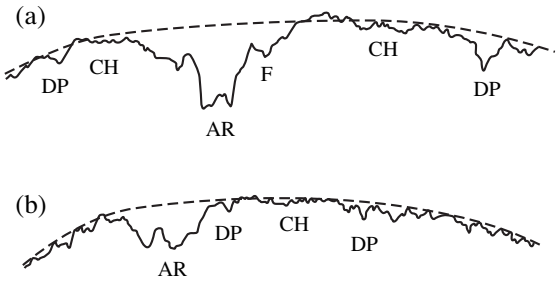

Fig. 3. Fragments of scans in the HeI 10830 Å line obtained on August 27, 1996.

We can see from the scans in the $H_\alpha \pm 0.5$ Å wings, the dependence of δC (curve V in Fig. 2), and the results presented in the table that the upflow velocities near these points are greater than those inside the coronal hole and in quiescent regions. Although the coronal holes are not identified as clearly in the H_α scans as in the HeI scans, the chains of dark points at the hole boundaries are quite visible (see, for example, scan IV in Fig. 2). Figure 3 presents fragments of scans obtained through a coronal hole surrounded by dark points, obtained at the center of the HeI 10830 Å line on August 28, 1996.

Figure 4 shows spectra in the vicinity of the helium line obtained at the center of the same coronal hole (spectrum *1*), in the quiescent solar atmosphere at the same heliocentric distance (spectrum *2*), and in faculae of an active region (spectrum *3*). A comparison between spectra *1* and *2* confirms that the central depth of the HeI line in the vicinity of the coronal hole is approximately half its value in the quiescent chromosphere.

The average depths at the center of the HeI line in dark points derived from our observations of coronal holes in 1996–1998 are (10.3–12.3)%. Using the method for determining the physical parameters of chromospheric plasma in [5], we obtain the following estimates: Doppler velocity 9.8–11.0 km/s, effective kinetic temperature 23000–29000 K, and total number of atoms at the lowest metastable level $2^3S - (0.7–1.0) \times 10^{12}$.

If we assume that the dark (in H_α and HeI) points surrounding coronal holes are groups of spicules or jets that increase the absorption in these lines, we can estimate the magnetic-field energy in a dark point. For the case of a spicule in the form of a thin tube with the average parameters from [13] ($B \approx 1000$ G, tube diameter 600 m, tube length 5000 m), we obtain a magnetic-field energy $W \approx 10^{20}$ erg. If we assume that (1) this energy can be completely converted to emission, (2) the dark points can be treated like elements of the chromospheric network with increased brightness, and (3) the filling factor of the spectrograph pupil by spicules in dark points is 0.5–0.7 [5], we find that the energy emitted by the dark points is $(0.5–0.7) \times 10^{30}$ erg. Consequently, generally speaking, the energy emitted by dark points at the boundaries of coronal holes is the same order of magnitude as the energy emitted by flares with moderate power.

Our observations indicate that the chains of dark points surrounding coronal holes exist for long times—over the entire lifetime of the hole, or at least for a large

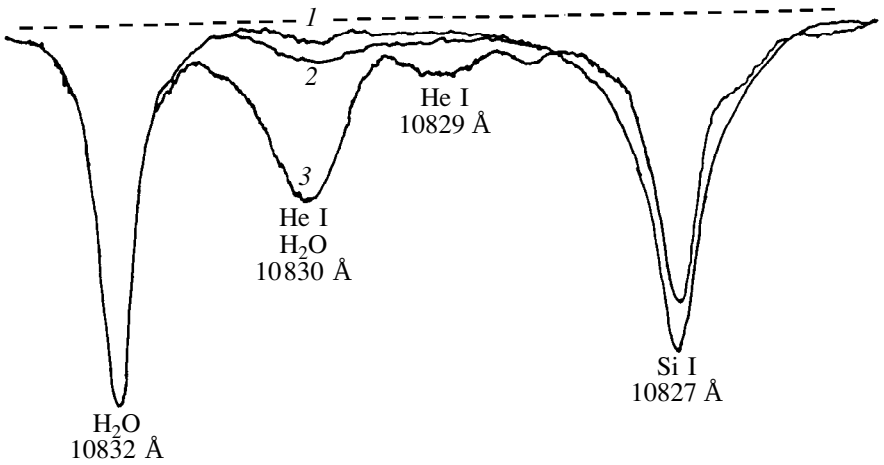

Fig. 4. Spectra in the region of the helium line: (*1*) at the center of a coronal hole, (*2*) in the quiet atmosphere, and (*3*) in the facular field of an active region.

part of this lifetime. The HeI dark points were identified in [14] with "magnetic bipoles." In addition, it was noted that the decay or formation of magnetic fluxes inside the "bipoles" is not a sufficient condition for the appearance of dark points. Many of them exist only for some fraction of the time for the existence and interaction of the magnetic field. Figures 2 and 3 in [14] show that network elements having opposite magnetic-field polarities (and, therefore, forming bipoles) continue to exist and decay for several hours after the disappearance of the dark points identified with the bipole.

Consequently, the formation, existence, and decay of magnetic bipoles in and of themselves are insufficient for the formation of dark points. We suggest that the formation and evolution of dark points result from more complex processes, namely, the interaction of a bipole magnetic field with the field of a coronal hole.

4. THE PROPOSED MODEL

According to our current understanding, three-dimensional reconnection of magnetic fluxes can occur efficiently at two levels in the solar atmosphere with completely different electrodynamic properties: the corona and the region of the temperature minimum [15]. In contrast to coronal conditions, the high efficiency of reconnection at the temperature minimum is associated with the small conductivity of the weakly ionized plasma there, rather than with the excitation of plasma turbulence in a reconnecting current sheet [16]. It is important, however, that reconnection is inevitable at both levels, although it is characterized by substantially different properties and leads to different observational consequences.

One of the consequences of reconnection in the region of the temperature minimum is the formation of a substantial upward flow of material from the chromosphere to the corona. The amount of material involved is sufficient to produce the prominences located above the corresponding photospheric neutral lines [11]. Our observations of filaments on the disk at the boundaries between active regions and coronal holes provide an indirect argument in favor of this. Reconnection in the corona (where the Alfvenic velocity is large) could give rise to high-speed plasma jets along the quasi-vertical magnetic field over the boundary of a coronal hole (compare with Fig. 1 in [17]). Such jets have been observed in the corona by the *SXT* X-ray telescope installed on the *Yohkoh* satellite [18], as well as by the *LASCO* optical coronograph on *SOHO* [19].

We propose that the reconnection process taking place in dark points, accompanied by the ejection of material to the corona and further into interplanetary space, occurs when the dark points border on a coronal hole, i.e., when they are adjacent to a large-scale unipolar structure with approximately vertical magnetic field, which becomes almost radial at large distances from the solar surface. The solar-wind flux directed along the field has the same behavior.

Figure 5 shows a simplified two-dimensional diagram of an interaction between two magnetic fluxes in the solar atmosphere. The first flux—at the photospheric level, denoted *N*—represents some fraction of the large unipolar field of the coronal hole. The magnetic field lines of this flux pass upward through the chromosphere *Ch* to the corona *C*. They are nearly vertical inside the coronal hole. The second magnetic flux belongs to the bipolar field, i.e., to a dipole source of *s* and *n* magnetic field in the photosphere. It moves toward the hole with some velocity v, as shown by the light arrows in Fig. 5b. Thus, the two magnetic fluxes—completely analogous to those in Fig. 1 in [17]—should interact with each other and reconnect.

We will assume that the reconnection begins at some point X of the corona rather than in the region of the temperature minimum. Then, as we can see in Fig. 5b, the reconnection will appreciably change the structure of the coronal magnetic field. Moreover, even a rela-

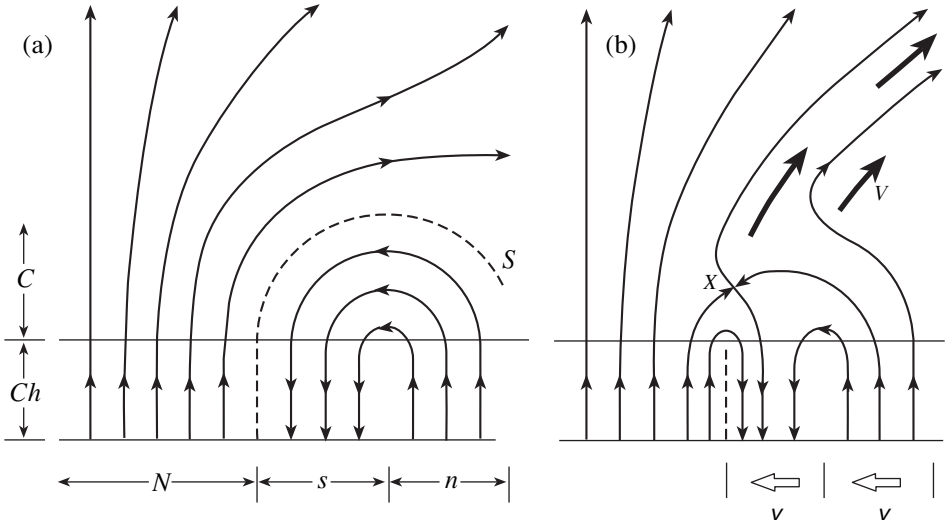

Fig. 5. A simplified two-dimensional diagram of the interaction and reconnection of two magnetic fluxes in the solar atmosphere: (a) initial state of the magnetic field and (b) reconnection in the corona as an origin of high-speed plasma streams.

tively slow reconnection in the lower corona can produce rapid plasma motions at larger heights. Thus, reconnection in the corona at places of interaction of magnetic fluxes at the boundary between an active region and a coronal hole considerably modifies the stationary pattern of the magnetic field and solar wind (Fig. 5a). High-speed streams appear in the corona (shown schematically by the thick arrows *V* in Fig. 5b). One mechanism for the acceleration of high-speed streams is based on the action of Lorentz forces on the frozen-in plasma. From this point of view, this general picture is quite similar to that proposed for coronal transients [20].

This is why the boundaries of coronal holes—and not their internal regions, as believed previously [7]—are the main source of high-speed streams of the solar wind. We hope that future satellite observations will confirm this hypothesis. Moreover, such observations will enable us to establish the relationship between the quite slow reconnection that occurs in the photosphere and the rapid reconnection characteristic of the corona.

ACKNOWLEDGMENTS

This work was supported by the Russian Foundation for Basic Research (project no. 99-02-16344).

REFERENCES

1. E. N. Avrett, J. M. Fontenla, and R. Loeser, in *Infrared Solar Physics*, Ed. by D. M. Rabin *et al.* (Kluwer Acad. Publ., Dordrecht, 1994), p. 35.
2. R. G. Giovanelli and D. N. B. Hall, Solar Phys. **52**, 211 (1977).
3. J. W. Harvey and W. C. Livingston, in *Infrared Solar Physics*, Ed. by D. M. Rabin *et al.* (Kluwer Acad. Publ., Dordrecht, 1994), p. 59.
4. L. M. Kozlova and B. V. Somov, Astron. Zh. **75**, 598 (1998) [Astron. Rep. **42**, 528 (1998)].
5. B. V. Somov and L. M. Kozlova, Astron. Zh. **75**, 926 (1998) [Astron. Rep. **42**, 819 (1998)].
6. E. V. Malanushenko, V. P. Malanushenko, and N. N. Stepanian, in *Motions in the Solar Atmosphere*, Ed. by A. Hanslmeier *et al*. (Kluwer Acad. Publ., Dordrecht, 1999), p. 251.
7. *Coronal Holes and High-Speed Wind Streams*, Ed. by J. B. Zirker (Colorado Associated Univ. Press, Colorado, 1977).
8. N. R. Sheeley and J. W. Harvey, Solar Phys. **59**, 159 (1978).
9. L. M. Kozlova, B. V. Somov, M. P. Tatarnikov, *et al.*, Izv. Ross. Akad. Nauk, Ser. Fiz. **60**, 136 (1996).
10. L. M. Kozlova, V. I. Kovshov, G. F. Sitnik, *et al.*, Tr. Gos. Astron. Inst., Mosk. Gos. Univ. **66**, 177 (1999).
11. Yu. E. Litvinenko and B. V. Somov, Solar Phys. **151**, 265 (1994).
12. J. M. Malherbe, T. Tarbell, J. E. Wiik, *et al*., Astrophys. J. **482**, 535 (1997).
13. Y. Suematsu, H. Wang, and H. Zirin, Astrophys. J. **450**, 411 (1995).
14. K. L. Harvey, in *Infrared Solar Physics*, Ed. by D. M. Rabin *et al.* (Kluwer Acad. Publ., Dordrecht, 1994), p. 71.
15. B. V. Somov, *Fundamentals of Cosmic Electrodynamics* (Kluwer Acad. Publ., Dordrecht, 1994).
16. B. V. Somov, *Physical Processes in Solar Flares* (Kluwer Acad. Publ., Dordrecht, 1992).
17. B. V. Somov and S. I. Syrovatskiĭ, Usp. Fiz. Nauk **120**, 217 (1976) [Sov. Phys. Usp. **19**, 813 (1976)].
18. *Observational Plasma Astrophysics: Five Years of Yohkoh and Beyond*, Ed. by T. Watanabe, T. Kosugi, and A. C. Sterling (Kluwer Acad. Publ., Dordrecht, 1998).
19. Y.-M. Wang, N. R. Sheeley, D. G. Socker, *et al.*, Astrophys. J. **508**, 899 (1998).
20. B. V. Somov, Adv. Space Res. **11**, 179 (1991).

Translated by Yu. Dumin

Astronomy Reports, Vol. 44, No. 6, 2000, pp. 407–413. Translated from Astronomicheskiĭ Zhurnal, Vol. 77, No. 6, 2000, pp. 467–473.
Original Russian Text Copyright © 2000 by A. Podgorny, I. Podgorny.

X-ray Bright Points on the Sun

A. I. Podgorny[1] and I. M. Podgorny[2]

[1]*Lebedev Institute of Physics, Russian Academy of Sciences, Leninskiĭ pr. 53, Moscow, 117924 Russia*

[2]*Institute of Astronomy, Russian Academy of Sciences, Pyatnitskaya ul. 48, Moscow, 109017 Russia*

Received April 20, 1999

Abstract—The possibility of forming X-ray bright points through local plasma heating near singular lines of the magnetic-field is considered. Reconnection is a plausible heating mechanism. Conductive heat losses should be impeded by the trap configuration of the magnetic field, which increases toward the periphery.

1. INTRODUCTION

X-ray bright points are the most widespread form of solar activity. They are distributed over the entire solar disk. Their lifetimes are typically measured in hours. Numerous observations indicate that the appearance of X-ray bright points is associated with the emergence of new magnetic flux. In particular, they are observed in the corona over small bipolar regions, known as ephemeral regions, with ascent speeds of about 2 km/s. Priest [1] considers bright points and flares to be similar phenomena that differ in the scale of their energy release; however, X-ray bright points appear much more frequently. The most intensely emitting portion of an X-ray bright point is about 5×10^8 cm in size [2–4]. In addition to X-ray bright points, bright points are also observed at visible wavelengths and may be arranged along curved lines [5].

The presence of hot localized emitters in the corona implies slow energy release processes, which ensure the maintenance of high temperatures within small volumes over long times. This may be associated with reconnection at a singular point between weak emerging magnetic flux and preexisting magnetic field with opposite polarity. Based on their analysis of various observations, Moses *et al.* [4] assert that X-ray bright points originate from the reconnection of small magnetic-flux elements when they encounter elements of an opposite-polarity magnetic system. The emergence of new flux must provide the necessary energy release in the vicinity of the singular line. However, the emerging flux must not be so large as to enable the accumulation of magnetic energy sufficient for a solar flare. If all the incoming magnetic energy is continuously converted into heat via reconnection, an X-ray bright point should be observed throughout the time of the flux emergence and subsequent cooling of the hot plasma formation.

2. CONFINEMENT OF THE HOT PLASMA

A bright point is distinguished from a flare not only by its smaller power, but also by the long existence of hot plasma in a restricted volume. At first glance, this presents some problems connected with energy balance. The time for conductive cooling of a bounded hot plasma formation, either in the absence of a magnetic field or via a heat flux along field lines, can be obtained from the equation of thermal conduction $\frac{\partial T}{\partial t} = \kappa_0 \frac{\partial^2 T}{\partial x^2}$.

Here, $\kappa_0 = \lambda^2/\tau_{ei} \sim 10^{20} T^{5/2}/n$, T is the electron temperature in eV, n the plasma density in cm^{-3}, λ the mean free path, and τ_{ei} the collision time for the electrons. For a hot plasma formation of size $d = 5 \times 10^8$ cm at $T =$ 1000 eV with $n = 10^9$ cm^{-3} (i.e., for a total stored energy of $\sim 10^{26}$ erg), the thermal diffusivity is $\kappa_0 \sim 3 \times 10^{18}$ cm^2/s, and the estimated cooling time is $t \sim d^2/\kappa_0 \sim 0.1$ s. Therefore, the losses due to thermal conduction comprise $W \sim nkTd^3/t \sim 10^{27}$ erg/s, in agreement with the power of a flare. At the same time, the radiative power [6] is only $W \sim 3 \times 10^{-23} n^2 d^3 \sim 10^{22}$ erg/s.

To bring the long lifetime of the hot bright-point plasma into agreement with the estimated energy release, which is incomparably smaller than in a solar flare, it would be natural to assume that the magnetic-field configuration in the neighborhood of the bright point ensures a high thermal insulation. The thermal diffusivity across the magnetic field is $\kappa_B = 6 \times 10^{-5} n/B^2 T^{1/2}$, where the temperature is measured in eV. Assuming that the vertical magnetic-field gradient is constant, the photospheric field is 100 G, the size of the heated region in the neighborhood of the neutral point is $\sim 5 \times 10^8$ cm, and the height of this region above the photosphere is $\sim 5 \times 10^9$ cm, we obtain a field intensity $B \sim 10$ G at the boundary of the hot plasma region; i.e., $\kappa_B \sim 20$. Thus, if the field configuration suppresses thermal conduction along the field lines, such heat losses can be neglected. The magnetic field near the zero point has the structure

1063-7729/00/4406-0407$20.00 © 2000 MAIK “Nauka/Interperiodica”

of a thermonuclear trap with a field that grows toward the periphery [7] (see, e.g., Fig. 1a below). Laboratory experiments show that the plasma in such a trap is stable. It can be cooled by the heat flux along the field lines near the separatrices. In this region, there are gaps with widths of the order of the Larmor radius r_L, through which the heat flux can escape along the field lines [7]. Therefore, the heat flux calculated from the nonmagnetic thermal conductivity is underestimated by the factor $d/r_L \sim 10^6$–10^7, with the cooling time being 10 h or so (here, $d \sim 5 \times 10^8$ cm is the size of a bright point). Thus, the cooling of X-ray bright points does not present an energy problem. Below, we consider the possibility of forming X-ray bright points via reconnection.

3. THE NUMERICAL EXPERIMENT

We solved the full system of MHD equations for a compressible plasma, including all dissipative terms [8, 9], in the XY plane, with the Y axis directed vertically upward and the X axis directed along the photosphere. The spatial distributions of the plasma density, temperature, magnetic field, and plasma velocity were calculated for different moments in time. The size L_0 of the calculation domain was used as the length unit. The plasma density ρ and temperature T were measured in units of their initial values, which were constant throughout the calculation domain. The unit for magnetic-field intensity was the mean magnetic field B_0 at the photospheric level in the solar region under study, i.e., on the X axis. We also used the Alfvén speed $V_A = B_0/(4\pi\rho)^{1/2}$ as the unit for the velocity V and the quantity L_0/V_A as the unit for time.

The following dimensionless parameters were introduced: the magnetic Reynolds number $\mathrm{Re_m} = 4\pi LV\sigma/c^2 = 10^5$, the Reynolds number $\mathrm{Re} = \rho LV/\eta = 100$, the Péclet number $\Pi = \rho VL/\kappa = 100$, and the plasma-to-magnetic field pressure ratio $\beta = 4\pi nkT/B^2 = 10^{-6}$. Here, η is the viscosity. Radiative losses were taken into account in accordance with [6], and the calculated electric conductivity $\sigma \sim T^{3/2}$ and thermal conductivity $\kappa \sim T^{5/2}$ were based on Coulomb collisions. In our calculations, we took into account the anisotropy of the plasma thermal conductivity in the magnetic field. We took the Péclet number for thermal conduction across the magnetic field to be 10^8. The method we used to choose the dimensionless parameters for the solar corona based on the principle of restricted modeling is described in [10].

A steady-state magnetic field with a neutral point in the calculation domain was specified either by introducing a set of dipoles under the photosphere or as a superposition of a constant field and an arch field. We studied the effect of plasma heating in the neighborhood of a neutral point under the action of weak ($\Delta B/B \sim 0.01$) photospheric perturbations.

At all boundaries, we took the velocity derivative in the direction normal to the boundary to be zero. At all boundaries other than the photospheric boundary, the normal derivative of the density was set to zero and the magnetic field and temperature were assumed to be time independent. At the photospheric boundary, a perturbation was created either by increasing the magnetic field or by increasing the density and temperature over some photospheric area.

The equations were solved using the PERESVET code, which approximates the MHD equations using a fully implicit iterative scheme.

4. NUMERICAL RESULTS

The purpose of the numerical experiment was to test the hypothesis that the energy release due to the reconnection of magnetic field lines in the neighborhood of a magnetic-field singular line can result in local heating of the coronal plasma and, consequently, in the appearance of a small-scale X-ray source. With this aim in view, we used two different magnetic-field configurations that are fairly typical of active regions. One was formed by the fields of four polarity-alternating vertical dipoles situated under the photosphere, in the XY plane. The X axis lies in the plane of the photosphere and the Y axis is normal to the photosphere. The other configuration had the form of a constant magnetic field inclined to the photosphere at an angle of 30°, and the arch field of two oppositely oriented vertical dipoles. We carried out calculations for four cases with various photospheric perturbations.

In the first case, we performed calculations for the field of four vertical subphotospheric dipoles with directions, magnitudes, and positions: (1) $\mu_1 = 26.25$, $X = 0$, $Y = -1.5$; (2) $\mu_2 = -48.125$, $X = 0.25$, $Y = -1.5$; (3) $\mu_3 = 48.125$, $X = 0.75$, $Y = -1.5$; (4) $\mu_4 = -26.25$, $X = 1$, $Y = -1.5$. Since the perturbations under study were weak, the overall field configuration shown in Fig. 1a for time $t = 0.6$ virtually coincides with the initial configuration. In the interval $0 \le t \le 0.1$, a plasma-density perturbation at the boundary $Y = 0$ in the region $0.4 \le X \le 0.6$ was specified by $\rho = 10000$; i.e., β was equal to 10^{-2}. Further, the density decreased linearly, so that it reached unity again at $t = 0.2$. Subsequently, a constant plasma density was maintained everywhere at the boundary $Y = 0$.

The arrows in Fig. 1a illustrate the plasma velocity field for a time $\Delta t = 0.4$ after the perturbation was switched off. The perturbation travels through the plasma normal to the magnetic field with the velocity $(C_S + V_A)^{1/2}$, i.e., as a magnetoacoustic wave. At the boundary $Y = 0$, the dimensionless wave speed comprises, to order of magnitude, $V_A = 1$. As the wave propagates, its speed decreases in proportional to the magnetic-field intensity. As this takes place, the velocity amplitude at the wave front is $V \sim 0.003$. By time $t \sim 2$, the wave reaches the neutral point. We can see from Fig. 1b that, at time $t = 4$, a flow typical of the magnetic reconnection process is present near the magnetic-field

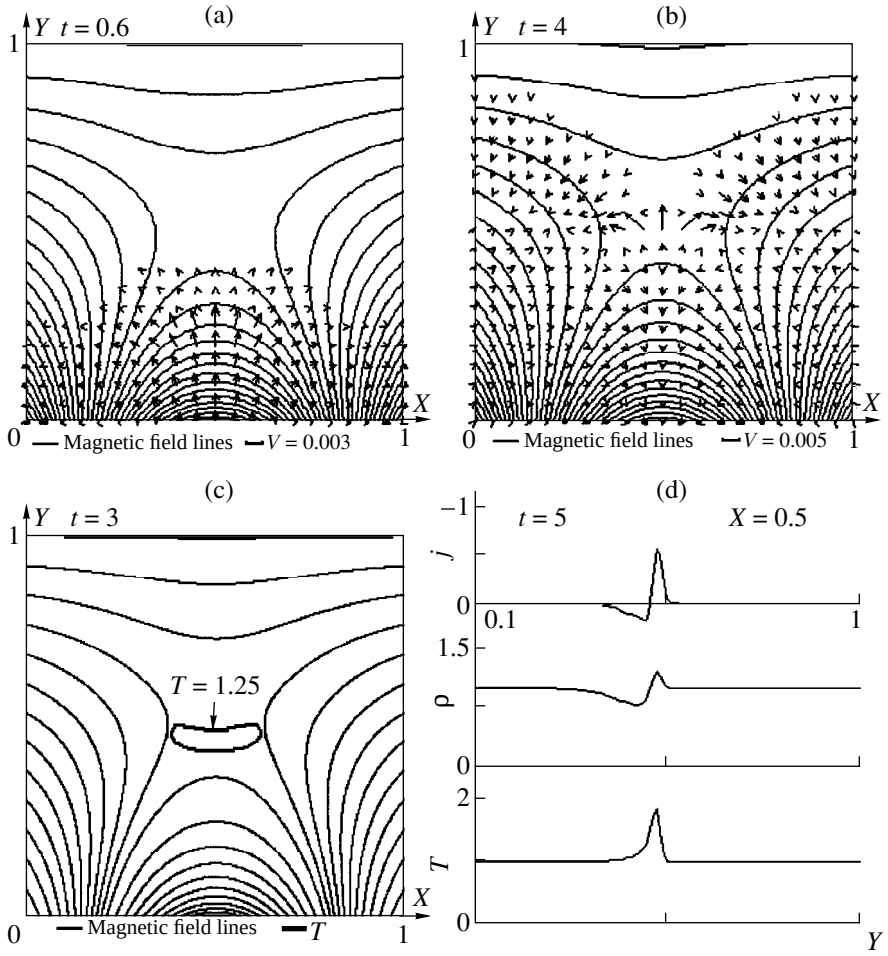

Fig. 1. Calculation for a photospheric perturbation in the form of four dipoles: (a) magnetic field lines and (b) plasma velocity vectors at times 0.4 and 3.8, respectively, after the cessation of the perturbation; (c) an isotherm in the neighborhood of the neutral point; (d) distribution of plasma parameters along the vertical axis.

zero point. It follows from Fig. 1c that the plasma is locally heated at this time (in the figure, the temperature contour $T = 1.25$ surrounds the neutral point). Figure 1d shows the density distribution of the current responsible for energy dissipation near the singular line and also the distributions of the plasma density and temperature at time $t = 5$. The density and temperature maxima coincide with the neutral point. A region of reduced plasma density can be seen below the neutral point. This is typical of flows in the neighborhood of a neutral point [11] and results from the acceleration of plasma inflow under the action of the $\mathbf{j} \times \mathbf{B}/c$ force. The maximum temperature, $T \sim 3$, is reached at $t = 8$.

In the second case, we carried out calculations for the same alternating-dipole configuration as in the first case but with a magnetic perturbation. The perturbations were introduced by a dipole situated horizontally (along the X axis) under the photosphere, at the point $X = 0.5$, $Y = -0.2$. The dipole magnitude grew from zero to $\mu_5 = 0.005$ by $t = 0.1$. After $t = 0.1$, all five dipole moments were held constant. As we can see from Fig. 2a, the magnetic field at the boundary $Y = 0$ in the region $\Delta X \sim 0.2$ increased by ~1% during this time. The overall plasma flow pattern was similar to that in Fig. 1. The velocity vectors near the neutral point are shown in Fig. 2b for $t = 5.5$ on an expanded scale, together with the magnetic field lines. The localization of the isotherms relative to the neutral point is illustrated in Fig. 2c. Figures 2d and 2e suggest a picture of the dynamics of the plasma velocity, density, and temperature. The data for time $t = 5.5$ demonstrate that the sharp peaks of the density and temperature spatially coincide with the zero magnetic field.

In the third case, the initial field was the superposition of a uniform field $B = 0.5$ inclined to the photosphere by 30° and the fields of two vertical dipoles with $\mu_1 = 4.5$ and $\mu_2 = -4.5$ situated at the points $X = 0.6$, $Y = -1.5$ and $X = 1.1$, $Y = -1.5$, respectively. We specified a magnetic perturbation in the same manner as in the second case. The patterns of the isotherms and mag-

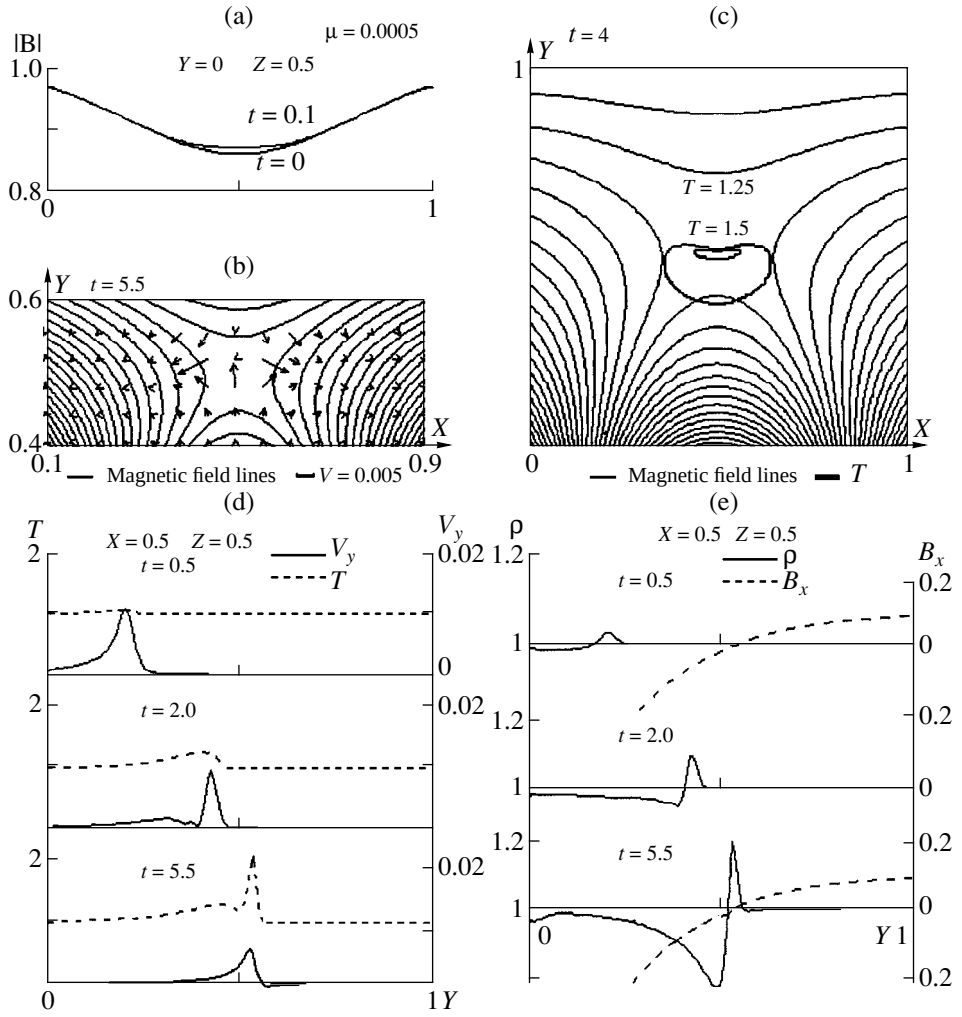

Fig. 2. Calculation for the rising field of four dipoles: (a) distributions of the absolute magnitude for the unperturbed ($t = 0$) and perturbed ($t = 0.1$) photospheric fields; (b) plasma velocity field and magnetic field lines in the neighborhood of the neutral point; (c) magnetic field lines and isotherms; (d) velocity perturbations (solid) and isotherms (dashed) for various times; (e) perturbations of density (solid) and magnetic-field distribution (dashed).

netic field lines are presented in Fig. 3a, and the temperature distribution is shown in Fig. 3b. Here, as in the two preceding cases, the heating of the plasma in the neighborhood of the neutral point can clearly be seen. In this computational run, a flow typical of the reconnection process also takes place near the neutral point (Fig. 3c). Figure 3d gives an indication of the density distribution of the current responsible for the reconnection. This distribution resembles a weakly developed current sheet with a maximum at the neutral point.

In the fourth case, we performed calculations for the same configuration of four alternating dipoles as in the first and second cases but considered the initial stage of development of a perturbation introduced by two powerful chromospheric sources resulting from local chromospheric heating during a flare. Subsequently, the vaporized plasma in these sources fills a magnetic flux tube; i.e., a post-flare loop forms [9]. We specified the plasma density to be $\rho = 10000$ and the temperature to be $T = 20$ in sources situated on the $Y = 0$ axis in the intervals $0.19 \le X \le 0.25$ and $0.75 \le X \le 0.81$. Both sources operated continuously during the entire computational run. In contrast to [9, 12], we consider here the initial stage of plasma injection, when the flux has not yet propagated a large distance from the photosphere. Physically, this corresponds to modeling a bright point at the initial stage of formation of a post-flare loop. The positions of the plasma sources relative to the initial magnetic-field configuration can be seen in Fig. 4a, which also shows field lines and isotherms (drawn in increments $\Delta T = 1$). The temperature distribution over the XY plane shown in Fig. 4b gives some indication of the shape of the temperature maximum. Further calculations show that the current decays in a time $t' \sim 30$. A the same time, there is no appreciable drop in temperature because of the low thermal conductivity across the magnetic field.

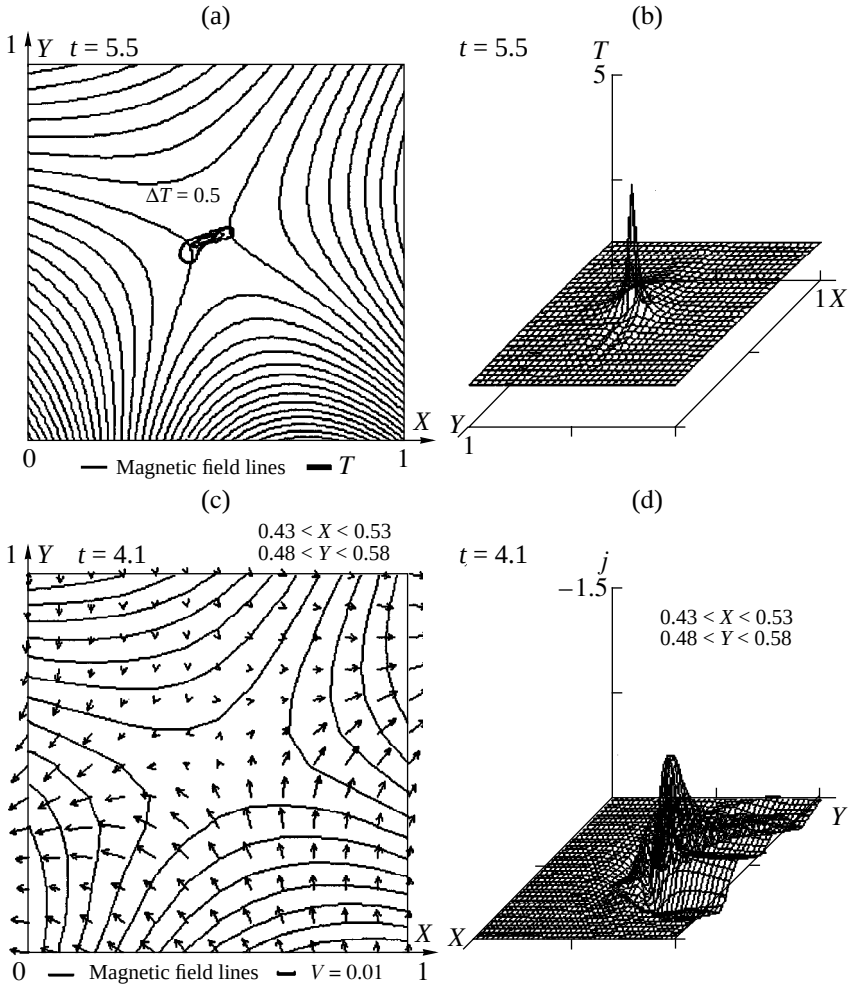

Fig. 3. Calculation for the superposition of an arch and uniform field: (a) magnetic field lines and isotherms, (b) spatial distribution of the temperature, (c) velocity field and magnetic field lines in the neighborhood of the neutral point, and (d) spatial distribution of electric-current density.

The energy transport toward the neutral point here differs from that in the first three cases. Figure 4c presents the distribution of plasma-velocity vectors for time $t = 1$, when the perturbation has not yet reached the neutral point. The positions of the sources are shown below the X axis. The plasma leaves the sources vertically, along the magnetic field. The velocity vectors in the figure at the points $X = 0.21$, $Y = 0$ and $X = 0.78$, $Y = 0$, correspond to the velocity of the plasma emerging from the chromospheric sources. The plasma stream has the velocity $V \sim 0.02$, and, at time $t = 1$, is still near the boundary $Y = 0$, within $Y = 0.02$. The wave excited by this outgoing plasma propagates along the magnetic field at the Alfvén speed, first upward and then along the curved field line. The vectors of the plasma-velocity perturbation are normal to the field everywhere over the stream. This means that the perturbation is carried by an Alfvén wave. The Alfvén perturbations encounter each other at the top of the field line and are transformed into a magnetoacoustic perturbation, which travels upward, across the field. Later, as in all preceding cases, the velocity field becomes typical of the reconnection process (Fig. 4d) responsible for local plasma heating in the solar corona.

In contrast to [11], in which the PERESVET code was used to study dramatic changes over active regions, we consider here very weak perturbations. Thus, the question arises as to the influence of purely methodical perturbations associated with the replacement of the MHD equations with a finite-difference scheme, which can, in principle, lead to artificial plasma heating near the neutral point. To test for finite-difference effects, we calculated the same fields with a neutral point but without specifying photospheric perturbations. The calculations demonstrated that, for both initial field configurations considered, the increases in the plasma temperature were no more than 1% of the temperature increases for the same times in the four cases considered.

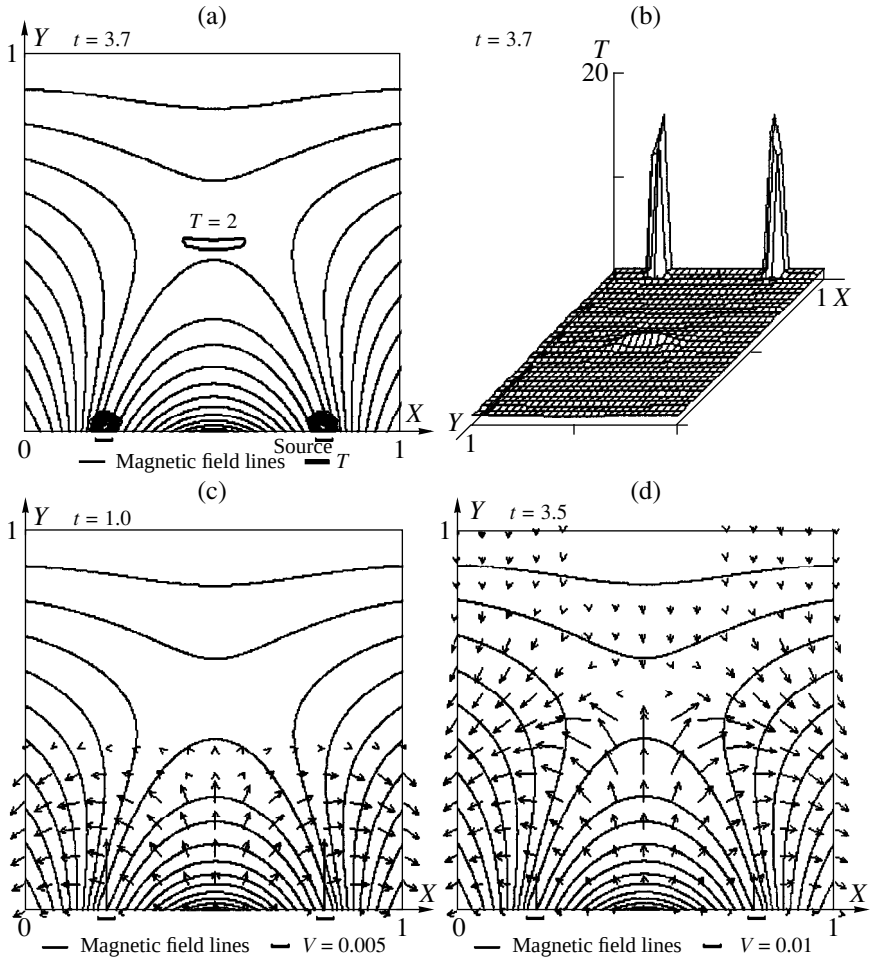

Fig. 4. Calculation for postflare chromospheric vaporization: (a) magnetic field lines and isotherms, (b) spatial distribution of the temperature, and magnetic field lines and plasma velocity fields at (c) $t = 1$ and (d) $t = 3.5$.

5. DISCUSSION

Our numerical experiments have shown that various types of weak photospheric perturbations can efficiently heat the plasma near a magnetic-field neutral line, increasing the temperature by an order of magnitude. A configuration with a neutral line can result from the superposition of magnetic fields from several different sources. Disturbances can be carried from the photosphere by magnetoacoustic and Alfvén waves. If the perturbations are weak, the current in the neighborhood of the neutral line does not substantially distort the original magnetic field. The reconnection of the magnetic flux carried by the plasma is fast enough to prevent the formation of a highly developed current sheet and the accumulation of a large amount of energy in this sheet. The prolonged existence of hot plasma is provided by magnetic thermal isolation. Thus, our numerical results provide evidence in favor of the hypothesis that reconnection can provide a mechanism for the formation of X-ray bright points.

All the data for our MHD simulations were presented in terms of a dimensionless time. For an active-region size $L = 10^{10}$ cm, coronal plasma density of $\sim 10^7$ cm^{-3}, and mean photospheric magnetic field under the neutral point of ~100 G, the Alfvén speed is $V_A \sim 5 \times 10^9$ cm/s, and the dimensionless time unit corresponds to ~2 s. Thus, for the short-term photospheric perturbations under consideration, with amplitudes of about 1%, the plasma velocity amplitude in the MHD wave is about 2×10^7 cm/s and the bright-point formation time is ~10 s.

We noted above that the plasma confined in the neighborhood of a neutral point loses some fraction of its energy via heat conduction through magnetic gaps. Heat fluxes narrowly channeled along the separatrices can produce local chromospheric heating. This probably results in the formation of two local chromospheric sources of L_α emission (bright points) situated symmetrically above the X-ray bright point; such sources were discovered by Kankelborg *et al.* [13].

Chertok [5] pointed out a regularity in the distribution of visible bright points over the solar disk. Such points tend to be arranged along certain lines. In the context of the data presented here, such an arrangement could result from the presence of long singular lines. If

so, weak local perturbations beneath such lines should give rise to a chain of bright points.

ACKNOWLEDGMENTS

This work was supported by the Russian Foundation for Basic Research (project no. 97-02-16290).

REFERENCES

1. E. R. Priest, *Solar Magnetohydrodynamics* (Reidel, Dordrecht, 1982; Mir, Moscow, 1985).
2. L. Golub, J. M. Davis, and A. S. Krieger, Astrophys. J. Lett. **229**, L145 (1979).
3. D. F. Webb, S. F. Martin, D. Moses, and J. W. Harvey, Solar Phys. **144**, 15 (1993).
4. D. Moses, J. W. Cook, J.-D. F. Bartoe, *et al.*, Astrophys. J. **430**, 913 (1994).
5. I. M. Chertok, Izv. Ross. Akad. Nauk, Ser. Fiz. **62**, 1873 (1998).
6. D. P. Cox and W. H. Tucker, Astrophys. J. **157**, 1157 (1969).
7. I. M. Podgorny and V. N. Sumarokov, J. Nucl. Energy, Part C **1**, 236 (1960).
8. A. I. Podgorny and I. M. Podgorny, Kosm. Issled. **35**, 253 (1997).
9. A. I. Podgorny and I. M. Podgorny, Astron. Zh. **75**, 132 (1998) [Astron. Rep. **42**, 116 (1998)].
10. A. I. Podgorny and I. M. Podgorny, Solar Phys. **161**, 165 (1995).
11. I. M. Podgorny and A. I. Podgorny, Solar Phys. **182**, 159 (1998).
12. A. I. Podgorny and I. M. Podgorny, Astron. Zh. **75**, 132 (1999) [Astron. Rep. **43**, 608 (1999)].
13. C. C. Kankelborg, A. B. C. Walker II, R. B. Hoover, and T. W. Barbee, Jr., Astrophys. J. **466**, 529 (1996).

Translated by A. Getling

Astronomy Reports, Vol. 44, No. 6, 2000, pp. 414–419. Translated from Astronomicheskiĭ Zhurnal, Vol. 77, No. 6, 2000, pp. 474–480.
Original Russian Text Copyright © 2000 by Sidorenkov.

Chandler Wobble of the Poles as Part of the Nutation of the Atmosphere–Ocean–Earth System

N. S. Sidorenkov

Hydrometeorological Center of Russian Federation, Bol'shoĭ Predtechenskiĭ per. 9–13, Moscow, Russia

Received May 17, 1999

Abstract—The paper presents calculated spectra of El Niño Southern oscillation (ENSO) indices. The ENSO spectra have components with periods that are multiples of the Earth's free (1.2 years) and forced (18.6 years) nutation periods. Analysis of a 41-year series of exciting functions for the atmospheric angular momentum confirms the existence of such periodicity. Nutation waves responsible for the El Niño phenomena in the ocean, the Southern oscillation in the atmosphere, and the presence of subharmonics of the Chandler period (1.2 years) and superharmonics of the lunar period (18.6 years) in the ENSO spectra are described. A model for the nonlinear nutation of the Earth–ocean–atmosphere system is constructed. In this model, the ENSO, acting at frequencies of combinational resonances, excites the Chandler wobble of the Earth's poles. At the same time, this wobble interacts with the nutation motions of the atmosphere and World Ocean. *© 2000 MAIK "Nauka/Interperiodica".*

1. INTRODUCTION

Despite a hundred years of investigation, the nature of the Chandler wobble of the poles (CWP) remains unclear. The mechanism for its excitation is still actively discussed. Meteorological and seismic processes are most frequently considered as possible drivers of the CWP. Most estimates suggest that the effect of the atmosphere is small. Opinions about the influence of earthquakes in exciting the CWP are quite contradictory. The most comprehensive reviews of this problem are given in [1, 2].

In our opinion, negative conclusions about the role of meteorological processes in exciting the CWP have been reached for two different reasons. The first is the scarcity of meteorological observations in the Southern Hemisphere, where the ordered oscillations of air masses between the Pacific and Indian oceans that swing the Earth (the El Niño Southern Oscillation, or ENSO) take place [3]. The second reason is the traditional use of linear oscillation theory for estimates, which is inadequate for describing these oscillations. Note that estimates of the excitation of the polar motion have usually been made near the principal resonance—the Chandler frequency [4, 5]. However, in the Earth–ocean–atmosphere system, nonlinear oscillations and excitation of the CWP occur primarily at combinational frequencies of the Chandler frequency (with periods of 2.4, 3.6, 4.8, and 6 years) [6], rather than at the principal resonant frequency.

Here, we present the results of our study of the power spectra of characteristics of oceanic and atmospheric processes. We also consider series of effective functions of the atmospheric angular momentum. These spectra confirm the presence of subharmonics of the Chandler period and indicate the presence of superharmonics of the fundamental period of the Earth's forced nutation (18.6 years). We have detected slow, presumably nutation, waves in the ocean and atmosphere, which are responsible for this cyclicity. Generalization of these results suggests the existence of coordinated nutation motions of the Earth, ocean, and atmosphere, which affect each other in a nonlinear way. We suggest that the wobble of the Earth's poles, the El Niño phenomenon in the ocean, and the Southern oscillation in the atmosphere—currently studied as independent phenomena in different disciplines—should be treated collectively as a single phenomenon in connection with the nonlinear nutation of the Earth–ocean–atmosphere–system.

2. INITIAL DATA

A large number of indices have been devised to describe the El Niño phenomenon. We will use the Southern oscillation index (*SOI*), which represents the normalized difference of the normalized pressure anomalies at the stations Tahiti (17°33′ S, 149°37′ W) and Darwin (12°26′ S, 130°52′ E), located at the antipodal centers of action of the Southern oscillation [6, 7]. There is a continuous series of monthly averages of the *SOI* from 1866 to the present time [7–9].

Wright [10] calculated mean quarterly *DT* indices as simple differences of the pressure anomalies at the Darwin and Tahiti stations averaged over three months. His report contains *DT* series from 1851 to the present time in steps of three months [10].

Thermal oscillations of the ocean are characterized by the temperature of the ocean's surface (TOS) averaged over the most representative regions. The well-known series of monthly average TOS indices for various *Niño* regions in the near-equatorial Pacific zone, the

1063-7729/00/4406-0414$20.00 © 2000 MAIK "Nauka/Interperiodica"

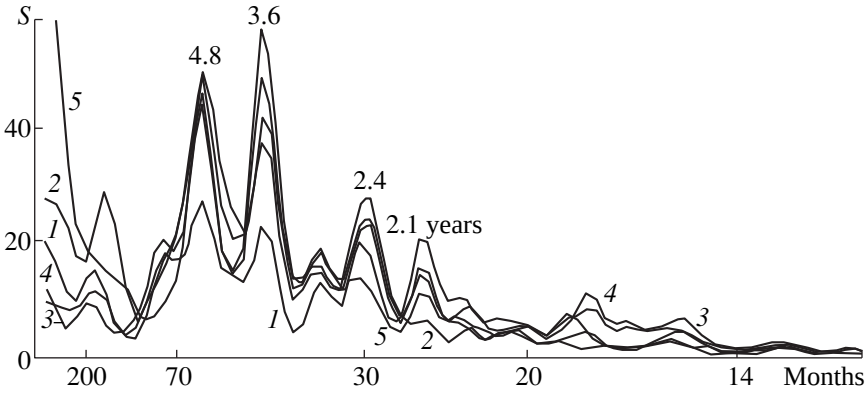

Spectra of oscillations of the *SOI* (*1*), *Niño4* (*2*), *Niño3.4* (*3*), *Niño3* (*4*), and *Tropics* (*5*) indices. Oscillation periods (in months) and spectral densities (in arbitrary units) are plotted on the horizontal and vertical axes.

N.Atl and *S.Atl* regions in the Atlantic, the *Tropics* regions in three oceans, etc., are regularly calculated at the US National Center for Environmental Prediction [8]. Regrettably, these series are available only for the period from 1950 to the present.

Series of the components χ_i of the exciting functions for the atmospheric angular momentum covering the period from 1958 to 1998 with a resolution of six hours are now available. Calculations made in the Atmospheric Angular Momentum Subbureau are based on a reanalysis of archived data for all hydrometeorological observations, performed at the National Center for Environmental Prediction [11, 12].

3. SPECTRAL ANALYSIS

Sidorenkov [6] published analyses of a series of *SOI* values starting in 1866 and of *DT* indices starting from 1851. This revealed components with periods of about 6, 3.6, 2.8, and 2.4 years (and possibly 12 years as well). Similar results are obtained by examining ENSO indices for 1870–1983 [13].

In the current study, we calculated periodograms and power spectra for series of *SOI* values and TOS anomalies for 1950–1997. Five hundred periodogram values were used for the spectral analysis. The spectra were smoothed using a 250-point Parzen window. The resulting spectra for anomalies of the *Niño3*, *Niño3.4*, *Niño4*, *Tropics*, and *SOI* indices for periods longer than 12 months are illustrated in the figure.

We also calculated the periodograms and power spectra of all daily averaged atomospheric angular momentum components χ_i^p and χ_i^w over the 41-year period. We used 3744 periodogram values to estimate these spectra. Smoothing was performed with a 1872-point Parzen window. The table contains the results of our spectral analyses of all the series. The detected periods are given in the third column in order of decreasing spectral power.

Although the analyzed series of ENSO indices cover a relatively short time interval, the detected periods mainly coincide with those derived from 145- and 114-year series [6, 13]. It is true, however, that a six-year period was detected in the 145- and 114-year ENSO series, while a 4.9-year period is indicated in the modern indices.

Spectral analysis of series of the atmospheric angular momentum components χ_i^w (wind components) and

Dominant cycles in characteristics of the ENSO and the atmospheric angular momentum components

Index	Region borders	Periods of dominant cycles, years
SOI		4.9, 2.4, 3.6, 2.1
Nino4	5° N–5° S 160° E–150° W	4.9, 3.6, 12, 2.4
Nino3.4	5° N–5° S 170° W–120° W	4.9, 3.6, 2.4, 2.1
Nino3	5° N–5° S 150° W–90° W	3.6, 4.9, 2.5, 2.1
Nino1 + 2	10° N–10° S 0°–360°	3.6, 4.9, 2.9, 2.1
Tropics	5° N–5° S 160° E–150° W	4.9, 3.6, 2.8, 2.4, 2.1
N.Atl	5° N–20° N 60° W–30° W	9.3, 3.6, 2.5, 2.1, 5.2
S.Atl	0°–20° S 30° W–10° E	12, 5.2, 2.3, 3.5
χ_1^w	Globe	2.7, 3.7, 1.86, 5.9, 2.4
χ_2^w	Globe	2.7, 3.1, 2.1, 1.8
χ_3^w	Globe	2.4, 3.7, 5.1
χ_1^{Pib}	Globe	2.6, 3.7, 4.6, 1.7
χ_2^{Pib}	Globe	2.4, 2.7, 5.9
χ_3^{Pib}	Globe	5.1, 4.1, 2.3, 2.7
18.6 years	Superharmonics	6.2, 4.7, 3.7, 3.1, 2.7, 2.3, 2.1

χ_i^{Pib} (atmospheric pressure components with allowance for the inverted barometer effect) indicates the possible presence of superharmonics of the forced nutation period (4.7, 3.7, 3.1, 2.7, 2.3, 2.1, and 1.86 years). Some of these superharmonics are close to the 2.4-, 3.6-, 4.8-, and 6.0-year subharmonics of the Chandler period. Thus, our analysis of the atmospheric angular momentum components is consistent with the results obtained from analysis of the ENSO indices. However, series of atmospheric angular momentum components are still too short to reliably detect many-year cycles.

The spectral–time diagrams of the *SOI* constructed in [13, 14], as well as wavelet and waveform analyses [15, 16], show that the *SOI* cycles are unstable in time. After emerging at certain frequencies, the cycles can fade over some time interval and be excited again at other frequencies. For example, a six-year ENSO periodicity dominated until the middle of the 20th century, when it was replaced by a 4.9-year cycle (see the figure). As noted in [15, 16], a four-year periodicity was most prominent in 1872–1890, while a three-year ENSO cycle became dominant in the period from 1890 to 1910. After 1910, the dominant period changed to seven years. From 1940 to 1960, a 5- to 6-year periodicity was most prominent, whereas in the 1960s, this was replaced by a two-year cycle and in 1971–1995, by a 4- to 5-year cycle. At the same time, the ENSO spectra averaged over 124 years (from 1872 to 1995) exhibit peaks at periods of 5.8, 3.8, and 2.8 years.

Thus, all these investigations indicate the presence in the ENSO spectra of components that are approximately multiples of the Chandler period (1.2 years) and of the fundamental period of the Earth's forced nutation (18.6 years), rather than being multiples of the annual period. The periods of superharmonics of the forced-nutation period are given in the last column of the table. It has become evident that such periodicity is due to the motion of slow waves in the atmosphere and the ocean. The waves move predominantly from west to east with various velocities and travel around the Earth primarily in time intervals equal to the above periods. The alternating sequences of the El Niño and La Niña phenomena in the ocean and of the Southern oscillation phases in the atmosphere are related to these waves.

4. A MODEL FOR EXCITING FREE MOTION OF THE POLES

During an ENSO, air and water masses are redistributed between the eastern and western hemispheres. The exchange occurs most intensively between the southern subtropical part of the Pacific Ocean and the eastern part of the Indian Ocean. The swing in the oscillations of sea level in the eastern and western parts of the tropical zone of the Pacific Ocean is ≈50 cm. Oscillations of atmospheric pressure at the antipodal centers of the action of the Southern oscillation reach 3 GPa at the ENSO frequency. These pressure anomalies are distributed over the globe in the way that is required to excite the polar wobble: The sign of the anomaly over the southwestern part of the Pacific and central Asia is opposite to the sign over the Indian Ocean and North America (these anomalies are described by the tesseral spherical harmonic $P_2^1(\theta, \lambda)$) [7, 17]. With this pressure distribution, the axis of the largest moment of inertia of the Earth (i.e., the axis of the Earth's figure) should deviate toward Asia in a La Niña oscillation and toward North America in an El Niño oscillation. Deviations of the axis of the Earth's figure from the rotation axis will necessarily give rise to free nutation of the Earth.

Let us now turn from a qualitative to a quantitative treatment of the problem. The excitation of the polar wobble can be estimated [18] using the equation

$$\frac{i}{\underline{\sigma}}\frac{d\underline{m}}{dt} + \underline{m} = \underline{\Psi}. \quad (1)$$

Here, $\underline{\sigma} = \sigma + i\beta$, $\sigma = 2\pi/T$ is the frequency of the free motion of the poles; T = 1.2 years is the Chandler period; β is the damping decrement; i is the square root of –1; $\underline{m} = m_1 + im_2$ (m_1 and m_2 are the direction cosines of the Earth's instantaneous angular rotation vector); and $\underline{\Psi} = \chi_1 + i\chi_2$ (χ_1 and χ_2 are the components of the exciting function for the atmospheric angular momentum) [18, 19].

To explain the observed wobble of the Earth's pole with a period of one year, it is sufficient for the atmospheric pressure oscillation to have an amplitude of 1.6 GPa; i.e., $P(\theta, \lambda) = 1.6 \sin 2\theta \sin(\lambda - \lambda_0)$ GPa [18]. As noted above, the amplitude of pressure oscillations during an ENSO reaches 3 GPa, so that excitation of the free nutation of the Earth is quite feasible.

The Chandler wobble of the poles is responsible for perturbations of the centrifugal potential and induces a polar tide in the atmosphere and ocean. For example, the static polar tide in the ocean has the form [18]

$$\zeta = -\frac{1+k-h}{g}\,\frac{\Omega^2 R^2}{2}\sin 2\theta(m_1\cos\lambda + m_2\sin\lambda), \quad (2)$$

where k and h are Love numbers, Ω is the magnitude of the Earth's angular rotation vector, θ is the colatitude, and λ is the longitude. In the atmosphere, the polar tide is described by the same expression, since

$$\Delta P = \int_0^{\zeta_a} \rho g\, dz, \quad (3)$$

but with a different amplitude. We should stress that the amplitude is a function of the polar deviation $\underline{m}$.

The typical amplitude of the static polar tide in the ocean is 0.5 cm. However, analysis of tide records indi-

cates a resonant spectral-density peak at period T [18]. A 14-month periodicity in the Atlantic subtropical circulation has repeatedly been noted [20, 21]. It was shown in [7, 22] that slow waves (0.25 m/s) move in the ocean along the equator, travelling around the Earth in 4.8 years. Such waves are also observed in the atmosphere. It has now been established that the periods of revolution of slow waves about the Earth vary with time, though their dominant values are multiples of the Chandler period (1.2 years) and of the period 18.6 years. This provides evidence that the waves are related to the free and forced nutations of the Earth. For this reason, we call them nutation waves.

By analogy with equations (2) and (3), we might expect that, in the case of linear interactions of nutation waves, the amplitude A of the exciting function $\underline{\Psi}$ for the atmosphere and the ocean must be a function of $\underline{m}$. However, the presence of subharmonics of the Chandler period (≈2.4, 3.6, 4.8, and 6.0 years) and superharmonics of the forced nutation period (≈2.3, 3.7, 4.7, and 6.2 years) in the ENSO and atmospheric angular momentum spectra indicate the nonlinear interaction of the forced and free nutation motions of the Earth, ocean, and atmosphere. Therefore, we assume that the amplitude A_k of each harmonic with number k of the exciting function $\underline{\Psi}$ has a power-law dependence on the value $\underline{m}$ of the deviation of the Earth's figure axis from the rotation axis, $A_k = \mu_k \underline{m}^{\alpha_k}$, where α_k is a power-law exponent different from unity and μ_k is a proportionality coefficient.

Using this assumption, we can approximate the function $\underline{\Psi}$ by the sum of N harmonics:

$$\begin{aligned}\underline{\Psi} &= \sum_{k=1}^{N} \mu_k \underline{m}^{\alpha_k} \exp[\omega_k i(t - t_{0k})] \\ &\approx \sum_{k=1}^{N} \mu_k \underline{m}^{\alpha_k} \exp(\omega_k i t).\end{aligned} \tag{4}$$

Here, k is the number of the harmonic, ω_k is its frequency, and $\omega_k t_{0k}$ is the initial phase, which is set equal to zero. For subharmonics of the Chandler frequency, $\omega_k = \sigma/n_k$, where $n_k = 2, 3, 4, \ldots$ are subharmonic numbers.

We were not able to find a solution of equation (1) with the function $\underline{\Psi}$ in the form (4). Therefore, we simplified expression (4):

$$\underline{\Psi} = \underline{m}^{\alpha} \sum_{k=1}^{N} \mu_k \exp(\omega_k i t). \tag{5}$$

Then, the solution of equation (1) with the function $\underline{\Psi}$ given by (5) at $m(0) = m_0$ takes the form

$$\begin{aligned}\underline{m}(t) &= \left\{ \underline{m}_0^{1-\alpha} \exp[(1-\alpha)\underline{\sigma} i t] - i\underline{\sigma}(1-\alpha) \right. \\ &\times \exp[(1-\alpha)\underline{\sigma} i t] \int_0^t \exp[(\alpha-1)\underline{\sigma} i \tau] \\ &\left. \times \left(\sum_{k=1}^{N} \mu_k \exp(\omega_k i \tau) \right) d\tau \right\}^{\frac{1}{1-\alpha}} \\ &= \left\{ \underline{m}_0^{1-\alpha} \exp[(1-\alpha)\underline{\sigma} i t] + \sum_{k=1}^{N} \frac{\mu_k (1-\alpha)\underline{\sigma}}{[(1-\alpha)\underline{\sigma} - \omega_k]} \right. \\ &\left. \times [\exp(i\omega_k t) - \exp[(1-\alpha) i \underline{\sigma} t]] \right\}^{\frac{1}{1-\alpha}}.\end{aligned} \tag{6}$$

The first term in braces of (6) describes the free motion of the pole due to its initial deviation $\underline{m}_0$. The second term (first sum) describes the overall forced motion of the pole with the excitation frequencies ω_k. The third term (second sum) describes the polar motion caused by the function $\underline{\Psi}$ with the fundamental frequency $\underline{\sigma}$.

Expression (6) describes the result in the most general form. To make this equation easier to understand, we make the following simplifications: (a) We neglect the initial deviation of the pole; i.e., we set $\underline{m}_0 = 0$, and (b) we neglect damping; i.e., we set $\underline{\sigma} = \sigma$. In this case, expression (6) takes the form

$$\begin{aligned}\underline{m}(t) &= \left\{ \sum_{k=1}^{N} \frac{\mu_k (1-\alpha)\sigma}{[(1-\alpha)\sigma - \omega_k]} \right. \\ &\left. \times [\exp(i\omega_k t) - \exp[(1-\alpha) i \sigma t]] \right\}^{\frac{1}{1-\alpha}} \\ &= \left\{ \sum_{k=1}^{N} \frac{\mu_k (1-\alpha)\sigma}{i[\omega_k - (1-\alpha)\sigma]} 2 \sin \frac{[\omega_k - (1-\alpha)\sigma] t}{2} \right. \\ &\left. \times \exp \frac{[\omega_k + (1-\alpha)\sigma]}{2} i t \right\}^{\frac{1}{1-\alpha}}.\end{aligned} \tag{7}$$

For $(1-\alpha)\sigma = \omega_k$, the term with number k in (7) is an indeterminate form of the type 0/0. For subharmonics of the Chandler frequency, the exponent $\frac{1}{1-\alpha} = n_k$ is equal to a positive integer number ($n_k = 2, 3, 4, \ldots$).

Let us suppose, for example, that $\omega_1 \longrightarrow (1 - \alpha)\sigma$. Then, the sine of the small angle in the first term of (7) can be replaced by the angle itself and will cancel from the numerator and denominator. All other terms (with numbers $k = 2, 3, \ldots, N$) remain unchanged, and we obtain

$$\underline{m}(t) = \left\{-\mu_1(1-\alpha)\sigma i t \exp(i\omega_1 t)\right.$$
$$+ \sum_{k=2}^{N} \frac{\mu_k(1-\alpha)\sigma}{[(1-\alpha)\sigma - \omega_k]}[\exp(i\omega_k t) \quad (8)$$
$$\left. - \exp[(1-\alpha)i\sigma t]]\right\}^{\frac{1}{1-\alpha}}.$$

The same result will be obtained if we formally evaluate the indeterminate form in (7) using L'Hópital's rule. The coefficient in the first exponential term increases with time t. All other terms have constant coefficients. Thus, at sufficiently large t, we can neglect all terms in braces except for the first.

In another time interval, a periodicity with frequency ω_k may dominate. In this case, analysis of the behavior of $\underline{m}$ gives a result similar to (8). Summing the resonant contributions from all terms, we obtain

$$\underline{m}(t) \approx \left\{\sum_{k=1}^{N}[-\mu_k(1-\alpha)\sigma i t \exp(i\omega_k t)]\right\}^{\frac{1}{1-\alpha}}$$
$$= \sum_{k=1}^{N}(\mu_k\omega_k)^{n_k} t^{n_k} \exp\left[i\left(\sigma t + \frac{3n_k\pi}{2}\right)\right]. \quad (9)$$

Here, we took into account the relations $(1 - \alpha)\sigma = \omega_k$ and $\frac{1}{1-\alpha} = n_k$.

Thus, for $\sigma = n_k\omega_k$, i.e., when the frequency of free oscillations of the pole is an integer multiple of the excitation frequency, a combinational resonance arises. The perturbing forces act synchronously with the proper oscillations of the Earth, giving rise to an intense swinging of the Earth about its rotation axis. The amplitude of the polar oscillations increases with time according to a power law (i.e., proportional to t^{n_k}), the more rapidly the lower the frequency of the subharmonic excitation component. Even low-power oscillations of the exciting function Ψ can lead to significant oscillations of the instantaneous angular rotation vector $\underline{m}$ of the Earth. As the amplitude of the polar oscillations increases, resistance leading to damping of the oscillation grows, so that an infinite increase of the amplitude becomes impossible.

It is known that the intensities of the ENSO and of the polar wobble vary with time. For example, the data reported in [15, 16] show that the ENSO amplitudes were large in 1870–1915, small in 1915–1950, and again large after 1960. A similar pattern was observed for the amplitudes of the CWP: In 1890–1915 and 1950–1998, they were a factor of two to three higher than in 1920–1945 [1, 2, 18]. In the period from 1930 to 1940, there were no long intervals with $SOI < 0$. In those years, the motion of the poles was also damped (the amplitude decreased, the period increased, and the CWP phase changed appreciably [1, 2, 18]). These facts demonstrate a coordination between the ENSO and the motion of the geographic poles. It is likely that time variations in the ENSO intensity lead to unstable CWP excitation. Instability of the ENSO is probably determined by the influence of the phase of the seasonal cycle on nutation motions of the atmosphere and ocean and by the summation of the forced and free oscillations of the Earth with similar frequencies.

5. CONCLUSIONS

The spectra of ENSO indices, nutation waves in the atmosphere, and other processes indicate that motions of the atmosphere and ocean are closely related to the lunar–solar nutation and motions of the Earth's poles. The mechanism of this relation is not entirely clear. One possibility is that the motions of the atmosphere, ocean, and Earth's poles all result from the external gravitational action of the Moon, Sun, and planets [23]. Another possibility is that there is a nonlinear interaction of the forced and free nutation motions of the Earth, ocean, and atmosphere. This last approach was considered in the model constructed above (see Section 4).

The atmospheric circulation due to various heat inflows to the atmosphere excites streams in the ocean. Interactions of the atmospheric circulation with processes in the ocean give rise to stochastic oscillations of the atmosphere and ocean. These interact with forced lunar–solar oscillations. Air and water masses are redistributed over the Earth's surface, changing the components of the inertia tensor. The axis of the Earth's figure (the axis of the largest moment of inertia) deviates from the rotation axis, which, in accordance with the laws of mechanics, leads to free nutation of the motion of the Earth's poles.

External actions from celestial bodies are superimposed on the internal stochastic oscillations of the atmosphere and the ocean. Some superharmonics (2.3, 3.7, 4.7, and 6.2 years) of the main component of the forced nutation motions of the atmosphere and ocean are near or equal to the subharmonics (2.4, 3.6, 4.8, and 6.0 years) of the period of free motion of the Earth's poles. Resonance excitation of the CWP occurs at these combinational frequencies.

The motion of the Earth's poles has a perturbing effect on the potential of centrifugal forces and induces

polar tides in the ocean and atmosphere, which, in turn, affect the motions of the atmosphere and ocean and the processes occurring in them. Thus, nonlinear oscillations with the characteristic competition, synchronization, and combinational-resonance phenomena are observed in the atmosphere–ocean–Earth system. Nutation motions of the Earth, atmosphere, and oceans are ordered and enhanced. As a result, cycles with periods that are multiples of the Chandler period and of the forced nutation period (18.6 years) appear in the spectrum of the ENSO. The equatorial zone, which serves as a trap for waves, locks onto the nutation motions of the atmosphere and ocean, which are therefore traced best there, as nutation waves.

Thus, the wobble of the Earth's poles, El Niño and La Niña oscillations in the ocean, the Southern oscillation in the atmosphere, and nutation waves are constituent parts of a single phenomenon—nutation of the Earth–ocean–atmosphere system.

ACKNOWLEDGMENTS

I thank A. N. Filatov for help in this work, which was supported by the Russian Foundation for Basic Research (project no. 99-02-16287).

REFERENCES

1. Ya. S. Yatskiv *et al.*, Itogi Nauki Tekhn., Ser. Astron. **12** (1976).
2. K. Lambeck, *The Earth's Variable Rotation. Geophysical Causes and Consequences* (Cambridge Univ. Press, Cambridge, 1980).
3. N. S. Sidorenkov, Astron. Zh. **69**, 905 (1992).
4. C. R. Wilson and R. A. Haubrich, Geophys. J. R. Astron. Soc. **46**, 707 (1976).
5. J. Vondrak and N. Pejovic, Bull. Astron. Inst. Czechosl. **39**, 172 (1988).
6. N. S. Sidorenkov, Astron. Zh. **74**, 792 (1997).
7. N. S. Sidorenkov, Tr. Gidromettsentra **316**, 31 (1991).
8. Climate Diagnostics Bulletin (NOAA, Climate Prediction Center, Washington, D.C).
9. R. J. Allan, N. Nicholls, P. D. Jones, and I. J. Butterworth, J. Climate **4**, 743 (1991).
10. P. B. Wright, Int. J. Climatol. **9**, 33 (1989).
11. E. Kalnay, M. Kanamitsu, R. Kistler, *et al.*, Bull. Am. Meteor. Soc. **77**, 437 (1996).
12. D. A. Salstein and R. D. Rosen, in *Proc. Seventh Conference on Climate Variations* (American Meteorological Society, Boston, 1997), p. 344.
13. U. Schneider and C. D. Schonwiese, Atmosfera **2**, 167 (1989).
14. N. S. Sidorenkov, in *Atlas of Time Variations of Natural, Anthropogeneous and Social Processes. Vol. 2. Cyclic Dynamics in the Nature and in Society* (Nauchnyĭ Mir, Moscow, 1998), p. 274.
15. D. Gu and S. G. H. Philander, J. Climate **8**, 864 (1995).
16. B. Wang and Y. Wang, J. Climate **9**, 1586 (1996).
17. K. E. Trenberth, Quart. J. R. Meteorol. Soc. **102**, 639 (1976).
18. W. H. Munk and G. J. F. Macdonald, in *The Rotation of the Earth, a Geophysical Discussion* (Cambridge Univ. Press, Cambridge, 1960), p. 323.
19. R. T. H. Barnes, R. Hide, A. A. White, and C. A. Wilson, Proc. R. Soc. London, Ser. A **387**, 31 (1983).
20. S. S. Lappo, S. K. Gulyaev, and A. E. Rozhdestvenskiĭ, *Large-Scale Thermal Interaction in the Ocean–Atmosphere System and Energy-Active Areas of the World Ocean* (Gidrometeoizdat, Leningrad, 1990).
21. V. V. Shuleĭkin, Izv. Akad. Nauk SSSR, Fiz. Atmos. Okeana **1**, 413 (1965).
22. N. S. Sidorenkov, in *Long-Term Variability of Conditions of the Natural Environment and Some Questions of Fishery Prediction* (VNIRO, Moscow, 1989), p. 99.
23. Yu. N. Avsyuk, *Tidal Forces and Natural Processes* (Schmidt United Institute for Physics of the Earth, 1996).

Translated by A. Kozlenkov